Control of Jets in Crossflow

A DISSERTATION
SUBMITTED TO THE FACULTY OF THE GRADUATE SCHOOL
OF THE UNIVERSITY OF MINNESOTA
BY

Rajes Sau

IN PARTIAL FULFILLMENT OF THE REQUIREMENTS
FOR THE DEGREE OF
DOCTOR OF PHILOSOPHY

Krishnan Mahesh, Advisor

June 2010

Acknowledgments

First, I would like to thank my advisor, Professor Krishnan Mahesh for his constant guidance, support and encouragement. His profound knowledge, professionalism and experience have helped me immensely in my research.

I am deeply indebted to my parents Mr. Ashok Kumar Saw and Mrs. Krishna Saw for their endless, unconditional love. Without their encouragement and inspiration I could not have ventured on this journey of doctoral research. I sincerely thank each member of my family in bringing this journey to a successful completion. My brothers Brijes and Binod motivated me strongly in all my endeavors. I am grateful to my wife, Munmun for her tremendous support. I would like to thank her for her patience and understanding during writing this thesis.

I would also like to pay my sincere gratitude to my friends. I especially thank Mr. Projjwal Banerjee for his extraordinary support in several ways during the last five years. I thoroughly enjoyed working with each and every colleague in my research group. In particular, I would like to thank Mr. Hyunchul Jang and Mr. Xiaochuan Chai. I thank Dr. Suman Muppidi for his help on numerous occasions during this project.

This work was supported by the Air Force Office of Scientific Research under grant FA–9550–04–1–0064 and the Office of Naval Research (ONR) under grant N00014–08–1–0433. Computer resources were provided by the Minnesota Supercomputing Institute (MSI), the National Center for Supercomputing Applications (NCSA) and the Texas Advanced Computing Center (TACC).

To my parents and my brothers,

and to my wife

Abstract

We use direct numerical simulations to study **control of jets in crossflow** by axial pulsing. Our main idea is that pulsing generates vortex rings; the effect of pulsing on jets in crossflow can therefore be explained by studying the behavior of vortex rings in crossflow. A method is proposed that allows optimal values of pulsation frequency, modulation and energy to be estimated a priori. This is accomplished in the following three stages.

First, direct numerical simulation is used to study the mixing of a passive scalar by a vortex ring issuing from a nozzle into stationary fluid. The 'formation number' (Gharib *et al.* 1998), is found to be 3.6. Simulations are performed for a range of stroke ratios encompassing the formation number, and the effect of stroke ratio on entrainment, and mixing is examined. When the stroke ratio is greater than the formation number, the resulting vortex ring with trailing column of fluid is shown to be less effective, at mixing and entrainment. As the ring forms, ambient fluid is entrained radially into the ring from the region outside the nozzle exit. This entrainment stops once the ring forms, and is absent in the trailing column. The rate of change of scalar containing fluid is studied for its dependence on stroke ratio. This rate varies linearly with stroke ratio until the formation number, and falls below the linear curve for stroke ratios greater than the formation number. This behavior is explained by considering the entrainment to be a combination of that due to the leading vortex ring, and that due to the trailing column. For stroke ratios less than the formation number, the trailing column is absent, and the size of the vortex ring

increases with stroke ratio, resulting in increased mixing. For stroke ratios above the formation number, the leading vortex ring remains the same, and the length of the trailing column increases with stroke ratio. The overall entrainment decreases as a result.

Next, direct numerical simulation is used to study the effect of crossflow on the dynamics, entrainment and mixing characteristics of vortex rings issuing from a circular nozzle. Three distinct regimes exist, depending on the velocity ratio and stroke ratio. Coherent vortex rings are not obtained at velocity ratios below approximately 2. At these low velocity ratios, the vorticity in the crossflow boundary layer inhibits roll–up of the nozzle boundary layer at the leading edge. As a result, a hairpin vortex forms instead of a vortex ring. For large stroke ratios and velocity ratio below 2, a series of hairpin vortices are shed downstream. The shedding is quite periodic for very low Reynolds numbers. For velocity ratios above 2, two regimes are obtained depending upon the stroke ratio. Lower stroke ratios yield a coherent asymmetric vortex ring, while higher stroke ratios yield an asymmetric vortex ring accompanied by a trailing column of vorticity. These two regimes are separated by a transition stroke ratio whose value decreases with decreasing velocity ratio. For very high values of the velocity ratio, the transition stroke ratio approaches the 'formation number' defined by Gharib *et al.* (1998). In the absence of trailing vorticity, the vortex ring tilts towards the upstream direction, while the presence of a trailing column causes it to tilt downstream. This behavior is explained.

Then, we study the mixing behavior of pulsed jets in crossflow using direct numerical simulations. The pulse is a square wave and the simulations consider several jet velocity ratios and pulse conditions. We study the effects of pulsing, and explain the wide range of optimal pulsing conditions found in experimental studies of the problem. Vortex rings in crossflow exhibit three distinct flow regimes depending on stroke ratio and ring velocity ratio. The simulations of pulsed transverse jets show that at high velocity ratios, optimal pulse conditions correspond to the transition

of the vortex rings produced by pulsing between the different regimes. At low velocity ratios, optimal pulsing conditions are related to the natural timescale on which hairpin vortices form. An optimal curve in the space of stroke ratio and velocity ratio is developed. Data from various experiments are interpreted in terms of the properties of the equivalent vortex rings and shown to collapse on the optimal curve. The proposed regime map allows the effects of experimental parameters such as pulse frequency, duty cycle, modulation, and pulse energy to all be predicted by determining their effect on the equivalent stroke and velocity ratios.

The thesis also discusses work towards the development of **Large Eddy Simulation (LES) methodology** to predict mixing in very high Reynolds number turbulent flows. We propose a novel estimation procedure to model the subgrid velocity for LES. The subgrid stress is obtained directly from the estimated subgrid velocity. The model coefficients for the subgrid velocity are obtained by imposing constraints on resulting ensemble-averaged subgrid dissipation and local subgrid kinetic energy. The subgrid dissipation may be obtained through either eddy–viscosity models or a new dynamic model for dissipation. The subgrid kinetic energy may be obtained either from the dynamic Yoshizawa model or a modeled transport equation. We also extend the estimation procedure to LES of passive scalar transport and propose an estimation model for subgrid scalar concentration. The subgrid flux is computed directly from the estimated subgrid velocity and estimated subgrid scalar. The model coefficient for the subgrid scalar is obtained by constraining mean scalar dissipation which is provided by an eddy–diffusivity approach. The velocity and scalar estimation models are applied to decaying isotropic turbulence with an uniform mean scalar gradient and good results are obtained. Realistic backscatter is also predicted.

A dynamic model for subgrid scale dissipation is proposed. The dissipation is modeled using invariants of strain–rate tensor. The proposed dynamic approach uses a second level test filter and the model coefficient is obtained using two scalar

identities. We show that this approach can also be used to obtain the Smagorinsky model coefficient for subgrid stress. This is an alternative to Germano's dynamic procedure where the single model constant is obtained by minimizing the error in a tensor identity, the Germano identity error.

Table of Contents

List of Tables

List of Figures

Nomenclature

f	Frequency
p	Pressure
r_j	Jet velocity ratio
r_{ring}	Ring velocity ratio
t	Time
u, v, w	Velocity in the x, y and z directions
x, y, z	Coordinate axes, coordinates
C	Passive scalar
D	Jet exit diameter
L	Stroke length
Re, Re	Reynolds number
Sc, Sc	Schmidt number
St	Strouhal number
T	Time period
U_∞	Free–stream crossflow velocity
U_p	Peak pulse velocity
$\overline{U}_{exit}$	Mean jet exit velocity

$\overline{U}_j$	Mean jet velocity
$U_{j,\mathrm{rms}}$	Jet r.m.s. velocity
ΔU_j	Peak–to–peak velocity
V_{sc}	Volume of scalar carrying fluid
V_{exit}, v_{exit}	Jet exit velocity
$\dot{m}_{\mathrm{nozzle}}$	Massflow rate at the nozzle exit
α	Duty cycle
τ	Pulse width
δ	Boundary layer thickness
ρ	Density
ν	Kinematic viscosity
ω_x, ω_y, ω_z	Vorticity components

Abbreviations

CVP	Counter–rotating Vortex Pair
DNS	Direct Numerical Simulation
DSM	Dynamic Smagorinsky Model
EDQNM	Eddy–Damped Quasi-Normal Markovian
LES	Large–Eddy Simulation
RSEM	Resolved Subgrid Estimation Model
SGS	Sub–Grid Scale
V/STOL	Vertical or Short Take–Off and Landing
ZNMF–JIC	Zero Net Mass Flux Jet in Crossflow

Chapter 1

Introduction

1.1 Motivation & background

A 'jet in crossflow' refers to a flow in which a jet of fluid exits an opening and interacts with fluid flowing 'across' the opening. A common example of a jet in crossflow is a smokestack (figure 1.1*b*), where the smoke plume is the jet and the crosswind is the crossflow. Other important engineering applications of jets in crossflow include dilution jets in gas–turbine combustors (figure 1.1*a*), film cooling of turbine blades, fuel injectors, pollutant dispersal, thrust vectoring of turbojets, and V/STOL aircraft.

In gas–turbine combustors, dilution holes allow cooler jets of air to enter the combustion chamber, cool the combustion products and thereby reduce the formation of pollutants e.g. NO_x gases. Again, different combustion regimes cause different pollutants to form. For example, Bowman (1982) notes that NO_x emission is usually minimized under conditions which cause carbon monoxide emissions to go up. Active control of dilution air mixing can therefore be used to optimize air fuel mixing at high power to reduce NO_x and de–tune it at low power to reduce CO (Karagozian *et al.* 2003). The ability to control the penetration and mixing behavior of dilution jets are central to the design of cleaner combustors. A related

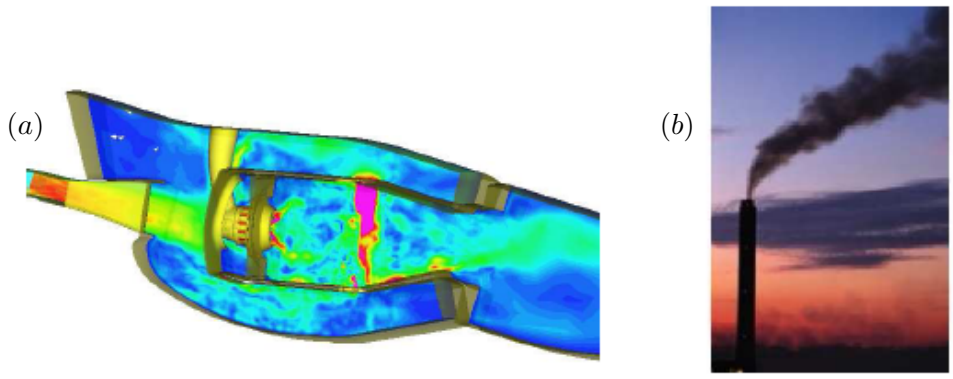

Figure 1.1: Practical examples of jets in crossflow: (a) Velocity contours of flow inside a gas–turbine combustor (Mahesh *et al.* 2004), (b) Smokestack (US Environmental Protection Agency).

problem occurs in the turbines in modern gas–turbine engines. Engine efficiencies can greatly increase if engine temperatures increase. However, higher temperatures can cause turbine blades to melt. Jets of air issuing from small holes on the surface of turbine blades ('film–cooling') are essential to cool the blades and prolong blade life. Flow fields generated by film–cooling injection are often a series of jets in crossflow. Actively manipulating the cooling jets by pulsing or modifying the shape of the film–cooling holes could significantly increase cooling efficiencies and turbine blade life.

1.2 Control of jets in crossflow

There have been considerable attempts to develop control strategies for jets in crossflow. Active control of jet penetration and mixing process can be achieved trough temporal excitation of the jet. Recent experiments (e.g. Wu *et al.* 1988, Vermeulen *et al.* 1992, Chang & Vakili 1995, Hermanson *et al.* 1998, Johari *et al.* 1999, Eroglu & Breidenthal 2001, Blossey *et al.* 2001, M'Closkey *et al.* 2002, Karagozian *et al.* 2003, Shapiro *et al.* 2006) have considered periodic pulsed excitation of the jet as a means of control, and shown that jet penetration and spread can be maximized

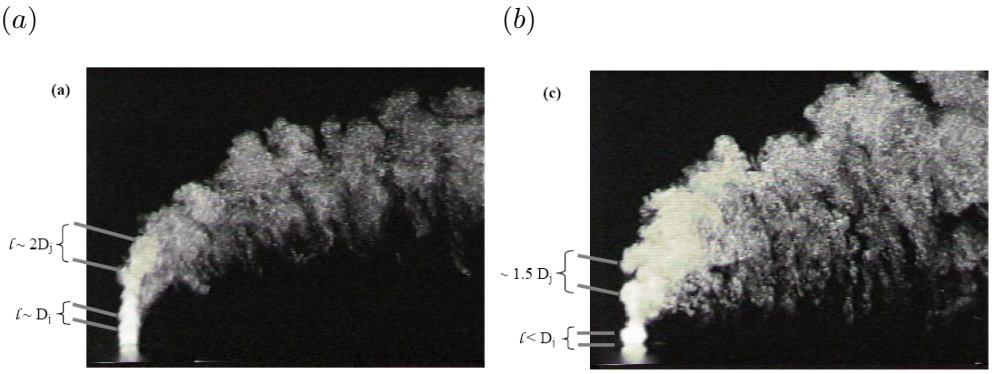

Figure 1.2: Experiments of Narayanan *et al.* (2003), jet in crossflow: (a) the unforced, $St = 0.0$ and (b) forced (sinusoidal) at $St = 0.19$. Reproduced from Narayanan *et al* (2003).

under specific pulsing conditions. The pulsing mechanism has involved solenoidal valves (Eroglu & Briedenthal 2001), spinning mechanical valves (Narayanan *et al.* 2003), and acoustic forcing (Vermuelen *et al.* 1990, M'Closkey *et al.* 2002, Shapiro *et al.* 2003). The effects of forcing amplitude, duty cycle (defined as the fraction of time during a period that the pulsing is 'on') and shape of forcing waveform have been considered. Though the penetration and mixing can be optimized at specific pulsing conditions, yet the optimal pulsing conditions vary widely among these different set of experiments (Vermeulen *et al.* 1992, Johari *et al.* 1999, Eroglu & Breidenthal 2001, M'Closkey *et al.* 2002, Shapiro *et al.* 2003, Narayanan *et al.* 2003).

Some researchers (Vermeulen *et al.* 1992, Narayanan *et al.* 2003) have employed sinusoidal forcing and show that the jet mixing is increased at specific pulsing frequencies. In the experiments of Narayanan *et al.* (2003), significant jet response is observed when sinusoidal forcing with peak to peak velocity excitation amplitude of 30% of the mean jet velocity is used (figure 1.2). They observe that the forcing frequency for maximized spread and mixing is greater than the transverse jet shear layer instability. Forcing at frequencies that are dominant near the jet exit does not cause appreciable change in jet penetration. Also, while mixing might be enhanced locally, peak scalar levels in the far–field remain high (Narayanan et al. 2003).

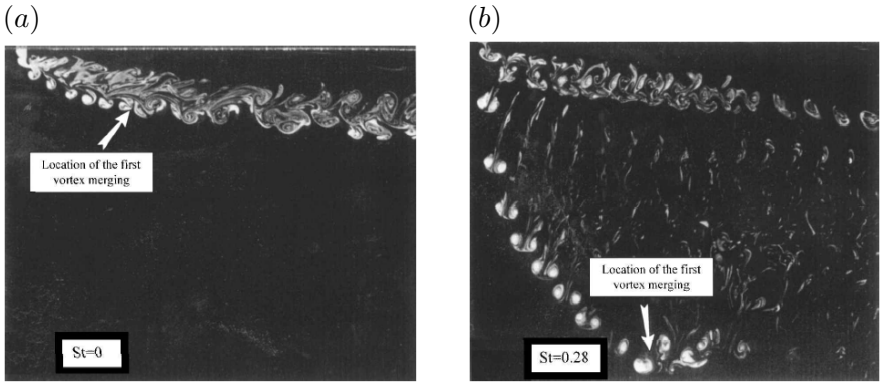

Figure 1.3: Experiments of Eroglu & Breidenthal (2001) showing (a) the steady jet, $St = 0.0$ and (b) the pulsed jet in crossflow, $St = 0.28$ at the same velocity ratio. Reproduced from Eroglu & Breidenthal (2001).

However, M'Closkey *et al.* 2002 observe that there is little response to jet to the sinusoidal forcing irrespective of the frequency even at very high amplitude excitation (such as peak to peak velocity exceeding 75% of the mean velocity magnitude).

Johari *et al.* (1999), Eroglu & Breidenthal (2001), M'Closkey *et al.* (2002) and Shapiro *et al.* (2006) use square wave excitation of the jet. The square waveform allows both frequency and duty cycle to be modified. Johari *et al.* (1999) suggest that long injection times yield moderate enhancement for fully pulsed jets, while short injection times and smaller duty cycle yield significant enhancement over the steady jet.

Eroglu & Breidenthal (2001) studied fully modulated pulsed transverse jets with square wave excitation at 50% duty cycle. When the flow rate of the jet was periodically modulated by a square wave, distinct vortex rings were created whose spacing and strength were dictated by the pulsing frequency for a given jet and crossflow combination. Figure 1.3 shows their experimental pictures of a steady jet and a pulsed jet in crossflow. Note that the pulsing creates discrete vortex rings and enhances the jet penetration into the crossflow. They also note that the pulsing might have a greater effect on mixing at low velocity ratios and lower Reynolds numbers.

M'Closkey et al. (2002) and Shapiro et al. (2006) performed numerous exper-

iments of pulsed jets in crossflow with square wave excitation. They developed a dynamical compensator or feedback controller to produce more accurate temporal square waveforms at the nozzle exit since it is difficult to generate accurate square waveform at the jet exit in experiments. Figure 1.4(b) shows the smoke visualization of the forced pulsed jet in crossflow with compensated square wave excitation (M'Closkey et al. 2002). Note the structural difference from the regular unforced jet in crossflow in figure 1.4(a). Pulsing creates discrete vortical structures which enhances the jet penetration significantly. Shapiro *et al.* (2006) utilizes square wave excitation to also vary the duty cycle at a given frequency as in figure 1.5. Note that the jet penetration is maximized at 30% duty cycle. The following observations are also made from their study. (i) Square wave excitation is more effective than sinusoidal forcing. (ii) Optimal forcing conditions are configuration and apparatus–dependent. (iii) Low frequency forcing yields significant increase in jet penetration depth. (iv) In general, as long as the forcing frequency is low enough, an optimal duty cycle is found to exist.

It is readily seen from experimental flow visualizations that square wave pulsing of the jet produces discrete vortex rings. This behavior may be anticipated, since pulsing would produce starting vortices. Some researchers (e.g. M'Closkey *et al.* 2002, Shapiro *et al.* 2003 and Johari 2006) relate optimal pulse condition for maximum penetration to the 'formation number' proposed by Gharib *et al.* (1998) for vortex ring formation in a quiescent medium. The formation number which is a universal timescale, denotes the transition between two distinct states of vortex rings in stationary fluid – single vortex ring and vortex ring with trailing column. Gharib *et al.* (1998) found that the vortex ring circulation is maximized at critical ratio of piston stroke length (L) to diameter (D) corresponding to 'universal time scale of vortex formation' or formation number. Formation number lies in the range $3.6 \leq L/D \leq 4.5$. Though, the critical stroke ratio for deeply penetrating vortical structures and optimal jet penetration, is approximately one-half of the 'formation

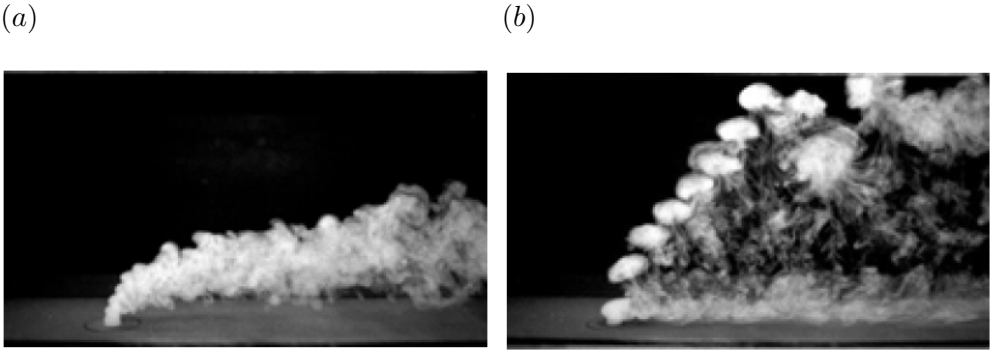

Figure 1.4: Experiments of M'Closkey *et al.* (2002), jet in crossflow: (a) the unforced, $St = 0.0$ and (b) forced (square waveform). Reproduced from M'Closkey *et al.* (2002).

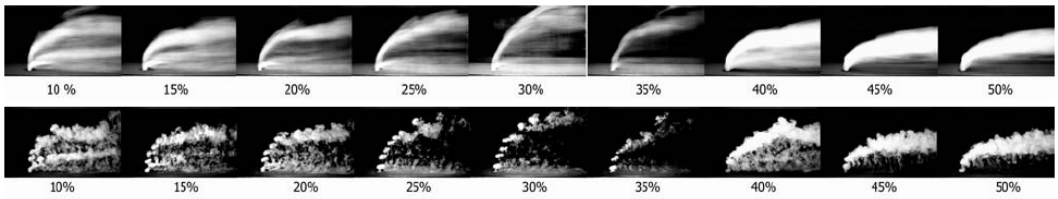

Figure 1.5: Experiment of Shapiro *et al.* (2006); mean and instantaneous flow–field with forcing frequency $f = 110$ Hz for duty cycle ranging from 10% to 50%. Maximum jet penetration occurs at 30% duty cycle corresponds to optimal pulse width ($\tau = 3$ ms). Reproduced from Shapiro *et al.* (2006).

number' (M'Closkey *et al.* 2002, Shapiro *et al.* 2003).

Johari (2006) proposes stroke ratio (L/D) and duty cycle as the only parameters describing pulsed jets in crossflow. A classification scheme is proposed which is based on the 'formation number'. He suggests that discrete vortex rings are created for $L/D < 4$ and rings with trailing column are produced for $L/D > 4$. The scaling used by Johari (2006) is only based on vortex ring properties in stationary fluid. The effect of crossflow; i.e jet to crossflow velocity ratio on the vortex rings is ignored.

There have been attempts to relate the pulsing to shear layer instabilities in the jet. Megerian *et al.* (2007) studied the effect of jet velocity ratio R on shear layer instabilities in transverse jets. The nature and strength of the instability modes were found to be significantly different between $R > 3.5$ and $R < 3.5$. They suggest that

low-level jet forcing does not appreciably influence the shear-layer response when strong modes are present; low–level forcing has significant influence when strong modes are absent.

There have been experimental attempts to optimize penetration and mixing. However, the physical mechanisms that maximize jet penetration are not well understood. Also, scaling laws that allow optimal conditions to be predicted/scaled are not known. Optimal conditions are typically presented in terms of Strouhal number, St. However, the optimal St can vary from 0.004 to 0.5 between experiments (Narayanan *et al.* 2003).

1.3 Contributions

The primary objective of the present work is to use direct numerical simulations to answer outstanding questions on pulsing as a means to control jets in crossflow. The principal contributions of this work are listed below.

- Direct numerical simulations are used to discover the optimal conditions for mixing in vortex rings in stationary fluid. The essential physics of scalar mixing and entrainment by vortex rings in stationary fluid are explained.

- Comparison of circulation, formation number and entrainment fraction of vortex ring between simulation and experiment yield good agreement.

- It is shown that a single vortex ring structure is more efficient in mixing with the quiescent ambient fluid than vortex ring with trailing column structure. The generation of trailing column is best avoided, if the objective is to entrain and mix as much as ambient fluid as possible.

- The effect of crossflow on the dynamics, entrainment and mixing characteristics of vortex rings are studied using DNS. Three distinct flow regimes with very different mixing characteristics were discovered - a vortex ring which tilts

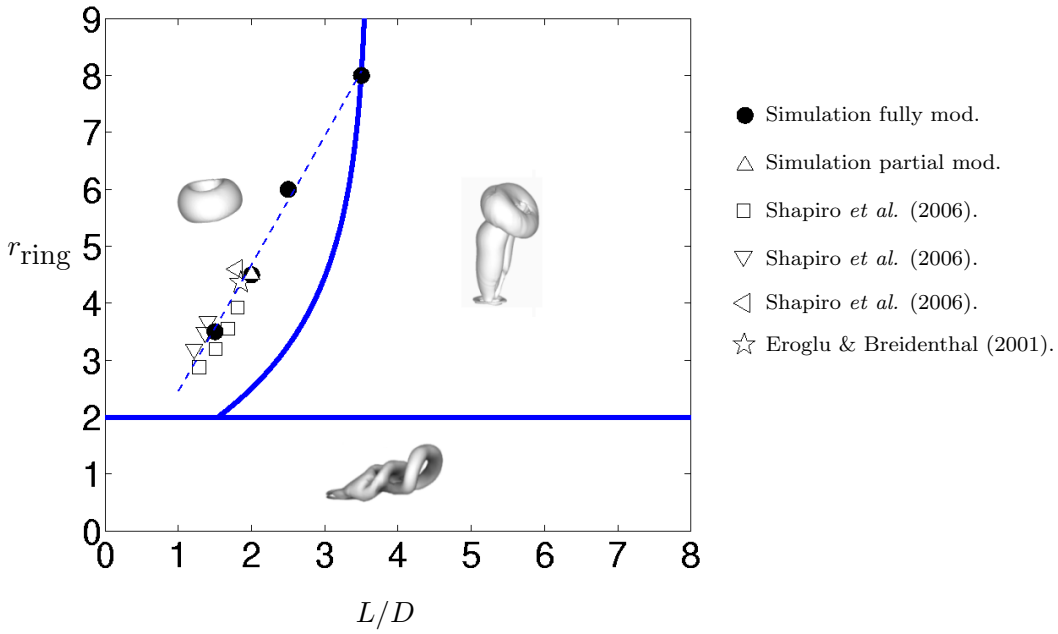

Figure 1.6: Optimal pulsing conditions from wide range of experiments and simulations collapse on a single curve in regime map

upstream, a vortex ring with trailing column which tilts downstream, and hairpin vortices which travel downstream.

- A regime map in vortex ring parameter space, classifying the three regimes, is developed. The transition boundaries between the different regimes are defined. The detailed physical mechanisms are explained.

- DNS of pulsed jets in crossflow at several jet velocity ratios and pulse conditions are performed. It is shown that the optimal pulsing conditions for jets in crossflow can be predicted in terms of the equivalent vortex rings produced by pulsing. Optimal conditions from DNS are shown to collapse on a single line in regime map. An optimal line in the regime map is presented.

- Optimal pulsing conditions for high velocity ratio jets in crossflow are shown to correspond to the transition of the vortex rings between the different regimes. For low velocity ratios, optimal conditions are related to the natural timescale

of hairpin vortex formation.

- Data from various experiments of pulsed jets in crossflow are interpreted in detail in terms of the equivalent vortex rings and shown to collapse on the same optimal line in the regime map (figure 1.6). The wide scatter in optimal Strouhal numbers in various experimental studies of the problem is explained.

- The regime map is proposed as a promising approach to predict optimal conditions for pulsed jets in crossflow. The proposed regime map allows the effects of experimental parameters such as pulse frequency, modulation, pulse energy etc. to all be predicted by determining their effect on the equivalent vortex ring (figure 1.6).

The thesis also contributes towards the development of Large Eddy Simulation (LES) methodology to predict mixing in very high Reynolds number turbulent flows such as pulsed jets in crossflow. The major contributions of this work are listed below.

- A novel subgrid scale velocity estimation model for LES is proposed. The model estimates the subgrid velocity as opposed to the common practice of only modeling the subgrid stress. The subgrid stress is directly computed from the modeled subgrid velocity. This estimation approach yields better subgrid scale physics such as large realistic backscatter of energy, than traditional stress models.

- A dynamic model for subgrid dissipation is proposed. We show that this dynamic approach for dissipation can also be used to obtain the Smagorinsky model coefficient for the subgrid stress. This is an alternative to the standard dynamic procedure used in LES.

- The velocity estimation approach is also extended to the passive scalar transport. An estimation model subgrid scalar is proposed.

Chapter 2

Vortex ring

2.1 Introduction

The motion of a fluid column of length L through an orifice of diameter D produces a vortex ring. Vortex rings have been studied by many researchers, and a large volume of work exists (see e.g. the review by Shariff and Leonard, 1992). Our study on vortex ring is motivated by experimental observations on the use of pulsing to control the mixing characteristics of free jets (e.g. Vermeulen *et al* 1986, 1992), and jets in crossflow (e.g. Johari *et al.* 1999, Eroglu *et al.* 2001, M'Closkey *et al.* 2002). Pulsing of the jet is seen to result in the formation of vortex rings, whose strength and spacing are dictated by the frequency and duty cycle of the jet. The resulting flow appears to improve mixing rate and increase the entrainment. We therefore examine the basic problem of how a vortex ring mixes with stationary fluid.

Most past work have studied vortex ring formation and their kinematics (e.g. Maxworthy 1977 and Didden 1979). The temporal evolution of vortex circulation during ring formation (Didden 1979; Glezer 1988), and during the post-formation phase (Maxworthy 1972) have been discussed. The total circulation and impulse have been shown to be approximately equal, for nozzles with, and without a wall at the exit plane (James & Madnia 1996). Gharib et al. (1998) show that around a

stroke ratio of 4, the flow transitions from a coherent vortex ring, to a ring with a trailing jet. They refer to this critical stroke ratio as the 'formation number'. The vortex ring is shown to achieve its maximum circulation at the formation number. Universality of the formation number was confirmed by generating vortex rings with different nozzle exit diameters, boundaries and non-impulsive piston velocities. Rosenfeld et al. (1998) numerically studied the effect of time history of velocity, velocity profile, vortex generator geometry and Reynolds number on the formation number. They found that the formation number appears independent of Reynolds number.

The entrainment characteristics of vortex rings were studied by Müller & Didden (1980) who estimated the entrainment fraction to be approximately 40% using a dye marker in their experiment. Dabiri & Gharib (2004) experimentally examined entrainment; their computed entrainment fraction is found to lie within 30% to 40% for stroke ratios of 2 and 4. They used counter–flow protocols to improve the entrainment fraction up to 65%. Their experiments do not resolve the convective fluid entrainment that occurs during the vortex ring formation. A computational study by James & Madnia (1996) examined entrainment and scalar mixing by vortex rings. However, their simulations were limited to small stroke ratios ($L/D < 4$), and do not comment on the effect of stroke ratio.

2.2 Simulation details

2.2.1 Problem statement

Figure 2.1(a) shows a schematic of the problem, where a slug of fluid is pushed through a cylindrical nozzle of 3 : 1 diameter ratio. The origin is located at the center of the nozzle exit plane, and the nozzle axis points in the $y-$ direction. The piston is modeled by specifying a time dependent velocity field (square wave pulse) at the nozzle inlet (e.g. Rosenfeld *et al.* 1998). A top–hat velocity profile (U_{in}) is

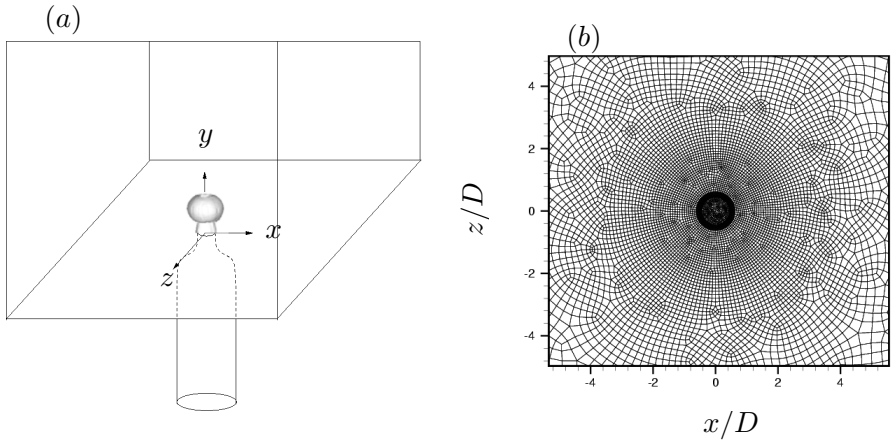

Figure 2.1: (a) A schematic of the problem. Note the schematic of the vortex ring generated by the fluid emerging out of the nozzle exit. (b) A horizontal slice of the mesh.

specified at the nozzle inflow for a duration of time τ (referred to as piston time duration). The inflow velocity is zero for time greater than τ. The stroke length and non–dimensional time are determined using the mean nozzle exit velocity, $\overline{U}_{exit}$ which denotes the equivalent piston velocity. The stroke length $L = \overline{U}_{exit}\tau$. The stroke ratio (L/D), defined as the ratio of the stroke length(L) to the nozzle exit diameter (D) is equal to $\overline{U}_{exit}\tau/D$. The stroke ratio is varied by changing the piston time duration τ. The Reynolds number of the flow based on $\overline{U}_{exit}$ and nozzle exit diameter (D) is 600. The non-dimensional time, $t^* = \overline{U}_{exit}t/D$ is referred to as formation time (Gharib *et al.* 1998). The simulations are performed for stroke ratios varying from 1.6 to 8.

2.2.2 Numerical details

The numerical scheme solves the incompressible Navier Stokes equations

$$\frac{\partial u_i}{\partial t} + \frac{\partial u_i u_j}{\partial x_j} = -\frac{\partial p}{\partial x_i} + \nu \frac{\partial^2 u_i}{\partial x_j x_j} \quad , \quad \frac{\partial u_i}{\partial x_i} = 0. \tag{2.1}$$

on unstructured grids. Here u_i, p and ν denote the velocities, pressure and kinematic viscosity respectively. The density of the fluid is assumed constant and is absorbed

into the pressure. The numerical scheme has been described in detail by Mahesh *et al.* (2004). The algorithm stores the Cartesian velocities and the pressure at the centroids of the cells (control volumes) and the face normal velocities are stored independently at the centroids of the faces. The scheme is a predictor–corrector formulation which emphasizes discrete energy conservation on unstructured grids. This property makes the algorithm robust at high Reynolds numbers without numerical dissipation. The predicted velocities at the control volume centroids are obtained using the viscous and the non–linear terms of equation 2.1 which are then used to predict the face normal velocities on the faces. The predicted face normal velocity is projected so that continuity is discretely satisfied. This yields a Poisson equation for pressure which is solved iteratively using a multigrid approach. The pressure field is used to update the Cartesian control volume velocities. Implicit time–stepping is performed using a Crank–Nicholson scheme. The algorithm has been validated for a variety of problems over a range of Reynolds numbers (Mahesh *et al.* 2004).

The passive scalar is computed by solving the advection-diffusion equation

$$\frac{\partial C}{\partial t} + \frac{\partial C u_j}{\partial x_j} = \frac{\nu}{Sc}\frac{\partial^2 C}{\partial x_j x_j}, \tag{2.2}$$

where C is the concentration of the scalar. The fluid emerging from the nozzle-exit has a value of $C = 1.0$, and the ambient fluid has $C = 0.0$. The spatial derivatives are computed using a predictor–corrector method (Muppidi 2006). The scalar field is first advanced using a second–order central difference scheme. The predicted scalar field is corrected in regions of scalar overshoot using a first order upwind scheme. This corrector step ensures that locally, the passive scalar concentration is bounded (*i.e.* $C \in [0, 1]$). The scalar is advanced in time explicitly using second order Adam-Bashforth scheme in an inner loop.

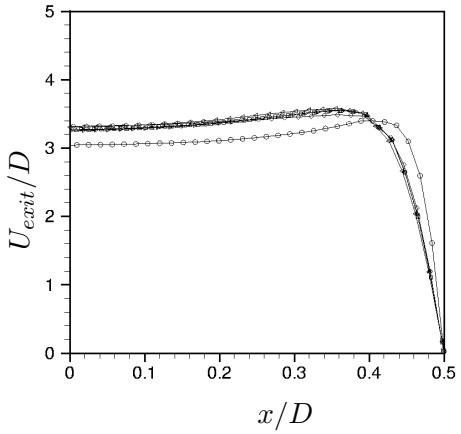

Figure 2.2: The velocity profile at the exit of the nozzle: $-\circ-$, $t^* = 0.50$; $-\diamond-$, $t^* = 0.95$; $-\triangleleft-$, $t^* = 1.50$; $-\triangleright-$, $t^* = 2.50$; $-\triangle-$, $t^* = 4.00$; $--$, $t^* = 5.50$;

2.2.3 Computational domain and boundary conditions

The computational domain above the nozzle exit spans $16D \times 24D \times 16D$. The domain includes the $10D$ length of nozzle upstream of the nozzle exit. The computational mesh is unstructured and hexahedral elements are used. Figure 2.1(b) shows a horizontal slice of the mesh. Note the very fine elements near the nozzle exit. The boundary conditions are specified as follows. Wall boundary conditions (i.e. $u_i = 0$) are specified at the nozzle wall, outer walls ($x/D = \pm 8$ and $z/D = \pm 8$) and wall at the nozzle exit plane. The wall at the nozzle exit plane refers to $y/D = 0$ plane excluding the nozzle–exit surface. At the nozzle inflow plane ($y/D = -10$ plane), a top hat velocity profile is specified:

$$v_{inflow} = \begin{cases} U_{in} & \text{if } t <= \tau \\ 0 & \text{if } t > \tau \end{cases}$$

The corresponding velocity profile at the nozzle exit is shown in figure 2.2 for $L/D = 6$. A zero-gradient boundary condition is used at the outflow ($y/D = 24$).

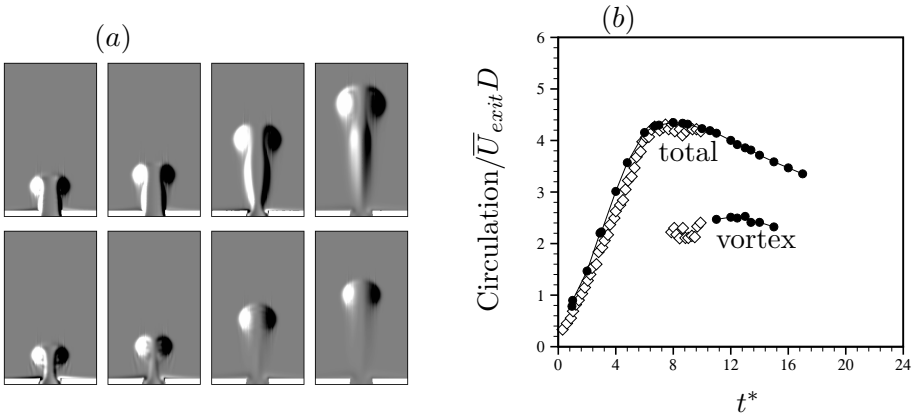

Figure 2.3: (a) Evolution of vorticity field during formation and post-formation phases of the vortex ring for $L/D = 6$ (top row) and $L/D = 2$ (bottom row). The formation time instants are 3.0, 4.0, 7.0 and 10.0 (from left). Note the vortex ring with a 'trailing column' for the higher stroke ratio. (b) Time evolution of the total and vortex circulation for $L/D = 6$: $\diamond$, experiment (Gharib *et al.*, 1998);$-\circ$-, simulation.

2.3 Results

2.3.1 Comparison to experiment

The simulation results are compared to experiment. The total circulation in the flow is compared to Gharib *et al.* (1998). This comparison serves to validate the present simulation, as well as to obtain the formation number for the nozzle-wall configuration. We also compare diffusive entrainment by the vortex ring to the experiments of Dabiri *et al.* (2004).

2.3.1.1 Formation number

Figure 2.3(a) shows vorticity contours for two vortex rings generated by stroke ratios of 6 and 2 respectively. In the case of higher stroke ratio, a vortex ring followed by a trailing column of fluid is generated (figure 2.3a). The time evolution of total circulation, and vortex circulation are shown in figure 2.3(b) for $L/D = 6$. Total circulation is computed by integrating the vorticity in the plane, $z = 0$ above the nozzle exit. Vortex circulation is estimated only after it clearly pinches off from

the trailing jet. The vorticity contour level that is used to determine the pinch off, is set to 5% of the maximum vorticity contour level. The pinch-off occurs in this case at around $t^* = 11$. Thus, the leading vortex circulation is estimated after $t^* = 11$ onwards. The formation number defined by Gharib *et al.* (1998), is 'the formation time when the total circulation imparted by the discharging flow is equal to the circulation of the pinched off vortex ring'. Their study showed the existence of a limiting value for the stroke ratio (L/D), above which the vortex ring does not absorb all the vorticity of the discharged fluid. They conclude that there is a maximum value of circulation that a vortex ring can acquire as the stroke ratio increases. This maximum is reached at a piston stroke ratio of $L/D \approx 4$. If the piston stroke ratio is higher than the formation number, the excess circulation accumulates in the jet like trailing column as shown in figure 2.3(a). For stroke ratio less than formation number, a single vortex ring is generated leaving behind a quiescent flow. In the simulation, the formation number is found to be approximately 3.6 from the circulation plot in figure 2.3(b). Also shown are results from Gharib et al's experiments (1998). Good agreement with experiment is observed.

2.3.1.2 Diffusive entrainment

Dabiri *et al.* (2004) computed the diffusive entrainment by an isolated vortex ring after formation. The difficulty in computing entrainment is the proper definition of the unsteady boundary of the vortex ring as it propagates. This difficulty can be overcome by changing the frame of reference. Figure 2.4(a) shows the instantaneous streamline in the global frame of reference. The boundary of the vortex ring is not well defined. Figure 2.4(b) shows the instantaneous streamlines in a reference frame that moves with the vortex ring. This is done by superimposing a free stream axial flow with magnitude equal to the measured ring axial velocity. The ring velocity was measured at the axial location of the maximum vorticity in the core of the vortex ring. The bounding streamline, 'vortex bubble' defines the extent of the vortex

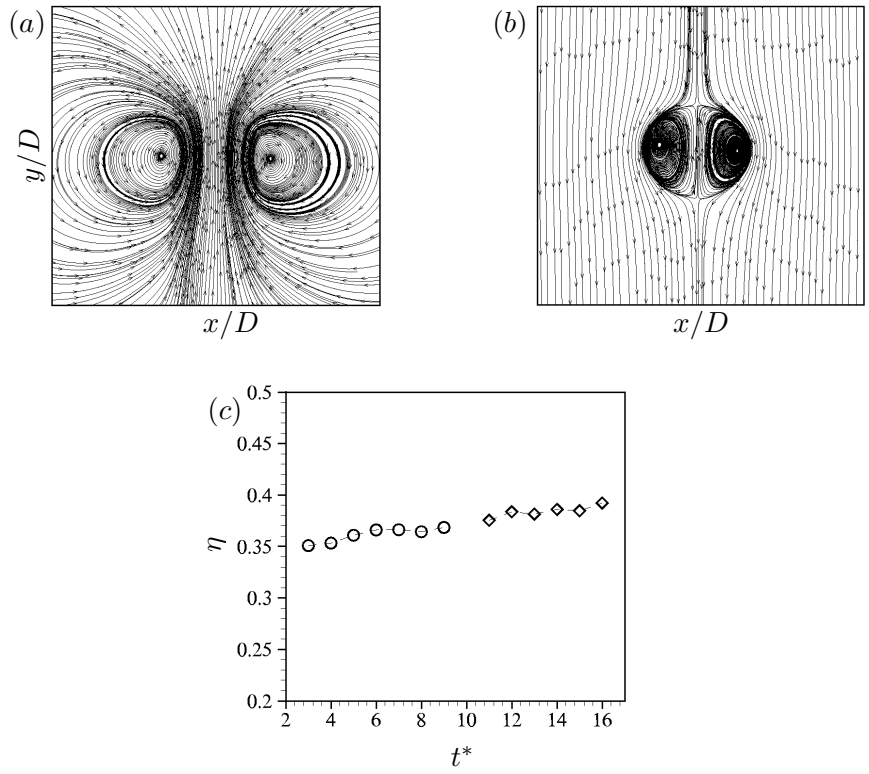

Figure 2.4: (a) Instantaneous streamlines. (b) Instantaneous streamlines in a reference frame that moves with the vortex ring. The limiting streamline shows the extent of the vortex ring or 'vortex bubble'. (c) The computed entrainment fraction using 'vortex bubble' approach for two different stroke ratios: -○-, $L/D = 2$; -◇-, $L/D = 4$.

ring visibly. The 'vortex bubble' is approximated as an ellipsoid to compute the volume. The volume of this ellipsoidal vortex bubble $V_B(t)$ is computed from the measured locations of the front and rear stagnation points as well as radial extent of the ring. Such visualization and measurement of the volume of the 'vortex bubble' is suggested by Dabiri *et al.* (2004).

Entrainment fluid fraction $\eta(t)$ is defined by $\eta(t) = \frac{V_B(t)-V_N(t)}{V_B(t)}$, where $V_B(t)$ is the volume of the vortex bubble and $V_N(t) = A\int_0^\tau U_{in}d\tau$ is the fluid volume supplied by the nozzle. Note that the entrainment is computed using the difference between bubble volume and the ejected volume. This definition assumes that nearly all of the ejected fluid is entrained into the ring, for low stroke ratios. Figure 2.4(c) shows the entrainment fraction computed for stroke ratios $L/D = 2,\ 4$ and plotted against the non-dimensional time t^*. The transient volumes are computed much after the formation phase so that the 'vortex bubble' is completely formed. Again the objective here is to compute the diffusive fluid entrainment after the vortex ring formation. Dabiri *et al.* suggested that the entrainment fraction lies between 30% to 40% in these two cases. Müller & Didden (1980) estimated the entrainment fraction to be approximately 40% in their experiment. In both the cases, the computed entrainment fractions lie between 30% to 40% which agree well with the experimental results.

2.3.2 Scalar mixing

The transport of passive scalar is used to study the mixing in vortex rings. The Schmidt number Sc of the scalar is 1.0.

2.3.2.1 Scalar field

Figures 2.5 and 2.6 contrast instantaneous scalar contours on the symmetry plane ($z = 0$) for stroke ratios equal to 2 and 6. The scalar profiles show three distinct regions. In the ring core, boundary layer fluid from the nozzle is stretched, and

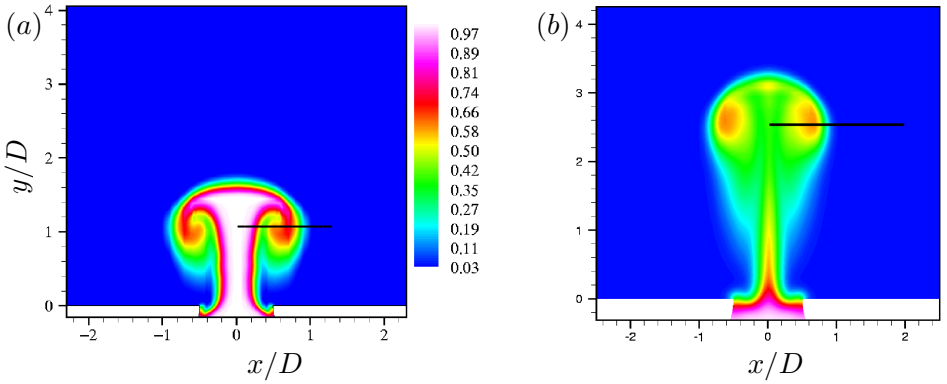

Figure 2.5: Instantaneous contours of passive scalar on $z = 0$ plane for $L/D = 2$ at t^*=(a) 3.024, (b) 6.552. Note the scalar mixing in the core of the vortex ring and downstream scalar deposition as the vortex ring propagates.

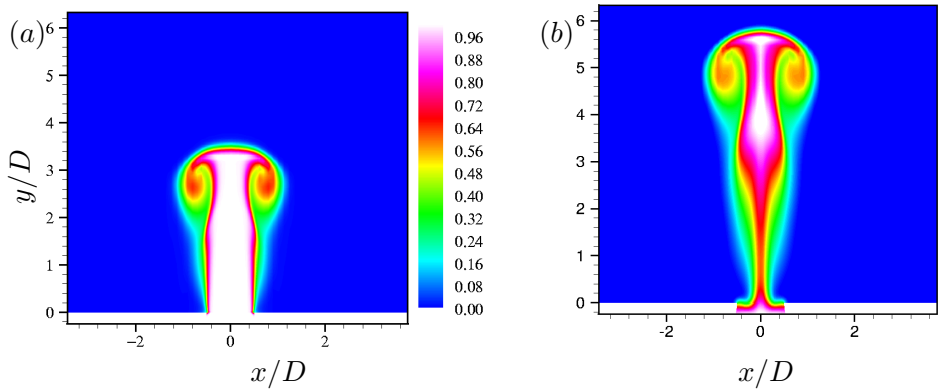

Figure 2.6: Instantaneous contours of passive scalar on $z = 0$ plane for $L/D = 6$ at t^*=(a) 6.048 and (b) 10.08. Note the trailing column behind the vortex ring.

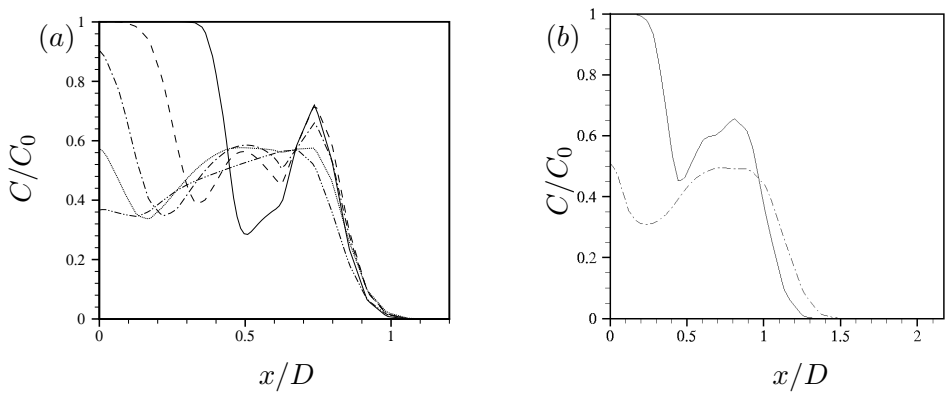

Figure 2.7: (a) Time evolution of variation of scalar concentration along the line passing through the cores of the vortex ring for $L/D = 2$: —— , $t^* = 2.016$; ---- , $t^* = 3.024$; —·— , $t^* = 4.032$; ····· , $t^* = 5.040$; —··— , $t^* = 6.552$.(c) Radial variation of scalar concentration along the line passing through the cores of the vortex ring for $L/D = 6$: —— , $t^* = 5.04$; —·— , $t^* = 14.1$.

mixed with entrained ambient fluid. Details of the entrainment of ambient fluid are discussed in the next section. At the boundary of the ring, the scalar diffuses because of the gradient between ring fluid and the ambient fluid. This diffused scalar is deposited by the ring in its wake (low velocity region), by a combination of its rotational velocity around the toroidal core, and its own propagation velocity. The amount of this fluid in the wake increases as the ring propagates. Similar downstream scalar deposition is observed by James & Madnia (1996). The fluid in the region surrounded by the toroidal core is mixed by diffusion because of the gradient at the interface of this region and toroidal core. The scalar in the trailing jet also diffuses into the ambient fluid.

The evolution of scalar inside the vortex ring can be quantitatively studied by examining profiles of the scalar along the line (shown in figures 2.5a and 2.5b) passing through the center (position of maximum vorticity) of the toroidal core of the vortex ring. Figures 2.7a and 2.7b show one half of the scalar profiles (the other half is identical) for $L/D = 2$ and $L/D = 6$. The curves corresponds to different time instants after ring formation. The peak scalar concentration is equal to 1.0

across almost half the radial extent of the ring at $t^* = 2.016$ for $L/D = 2$ in figure 2.7(a). Past $x \sim 0.5D$, there is a sudden drop in the concentration. This is due to the entrained ambient fluid during the formation phase. The small region ($0.65 < x/D < 0.85$) towards the boundary of the ring is filled with stretched boundary layer fluid from nozzle and the gradients near this region are sharp as expected. At later times, the width of the region containing peak scalar concentration near the axis of symmetry decreases rapidly. Scalar contours and profiles for $L/D = 2$ suggest that the vortex core is the region of significant mixing during the initial phases. However, at later time after formation, the maximum scalar concentration is found near the core region of the ring. At $t^* = 6.552$, the sharp gradients inside the vortex ring have disappeared, and peak scalar concentration is observed around the core of the vortex ring. These profiles flatten at later times. Note that past $x/D = 1$, the scalar concentration is negligible even when the ring propagates. One would expect viscous diffusion to gradually increase the scalar concentration beyond $x/D = 1$. The reason for this behavior is that the time scale of ring propagation is faster than the diffusion time scale. As a result, scalar that diffuses from the edge of the ring is deposited in the wake of the ring. Figure 5(b) shows that there is considerable amount of scalar deposition on the downstream side of the ring for $L/D = 2$. Note that global conservation of the scalar was confirmed by computing the average scalar concentration $\bar{c} = \left(\int_V C dV\right)/V$, where V denotes the volume of the domain. For all stroke ratios, $\bar{c}$ was found to be constant after the inflow stops.

The scalar field is quite different in the case of $L/D = 6$. The basic difference is that all the scalar carrying fluid issuing from the nozzle does not go into the vortex ring. Scalar contours in figure 2.6 shows the trailing column of very high scalar concentration. The scalar profiles in figures 2.7(a) and 2.7(b) suggest that the qualitative behavior of scalar field inside the vortex ring is similar in both cases of stroke ratios. But the mixing process is much slower in the case of $L/D = 6$ as compared to $L/D = 2$. For example, the profile at $t^* = 5.04$ for $L/D = 2$ in figure

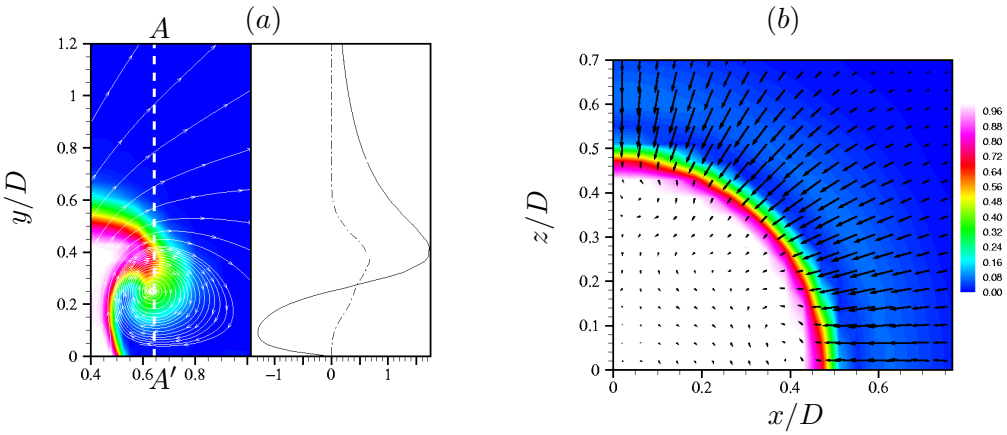

Figure 2.8: (a) (Left) Instantaneous streamlines on ($z = 0$) plane along with contours of scalar for $L/D = 2$ at t^*= 1.008. (Right) Variation of u velocity and scalar concentration along the line AA' at t^*= 1.008: —— , u/D; —·— , C/C_0 scalar concentration.(b) A horizontal cross–section of the flow-field at $y/D = 0.1$ at t^*= 1.008. Contours of scalar along with in–plane velocity vectors. Note the length and direction of the velocity vectors in the ambient field.

2.7(a) is qualitatively similar to the profile at $t^* = 14.1$ for $L/D = 6$ in figure 2.7(b). The vortex ring with $L/D = 6$ takes much larger time to attain a similar scalar profile inside the vortex ring.

2.3.2.2 Entrainment during formation

Figure 2.8(a) shows the instantaneous streamlines in the near field for $L/D = 2$ at $t^* = 1.008$, and the u–velocity profile and scalar concentration along the line AA' (shown as dotted white line). As the ring forms, ($t^* < 2.0$ in this case), a region of very low pressure is created just outside the nozzle, at the center of the vortex core. The resulting pressure gradient is directed towards the vortex center, and causes ambient fluid to be entrained. This behavior is illustrated in figure 2.8b, which shows strong negative u–velocities near the nozzle–exit, close to the wall. The scalar concentration of the fluid with negative u–velocity near the wall is near zero, indicating ambient fluid. Figure 2.8(b) shows a horizontal cross–section at $t^* = 1.008$ at a height of $y/D = 0.1$. Velocity vectors are shown along with scalar

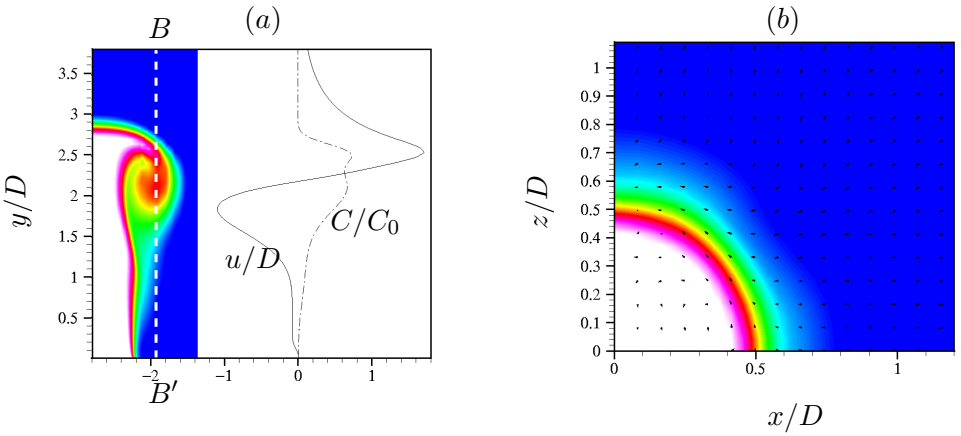

Figure 2.9: (a) $L/D = 6$ at t^*= 5.04, variation of u velocity and scalar concentration along the line BB' (dotted white line): ——— , u/D; —·— , C/C_0 scalar concentration. (b) A horizontal cross–section of the trailing jet at $y/D = 0.6$ at t^*= 5.04. Contours of scalar along with in–plane velocity vectors. Note that the in–plane velocity vectors are of zero magnitude. Same scalar contour levels are used here as in figure 2.8.

contours. The velocity vectors show the motion of the ambient fluid toward the edge of the fluid emanating from the nozzle–exit. These results show that ambient fluid is radially entrained into the vortex ring, from the near field of the nozzle, during the formation phase.

For the case of large stroke ratio ($L/D = 6$), the phenomenon is similar until $t^* \sim 3.6$ (formation number). After this time, fluid from the nozzle cannot enter the vortex ring, and instead forms a trailing jet behind the vortex ring. The vortex ring is largest in size when the stroke ratio equals the formation number. During formation, the vortex ring entrains ambient fluid as explained earlier. However, the trailing jet does not entrain ambient fluid similar to a vortex ring. Figure 2.9(a) shows the u–velocity and scalar concentration profiles along the line BB' passing through the core of the vortex ring with $L/D = 6$ at $t^* = 5.04$. Note that the u–velocity is almost zero near the trailing column up to a height of $y/D = 1$. Figure 2.9b shows a horizontal cross section of the trailing jet at $y/D = 0.6$ for $L/D = 6$ at $t^* = 5.04$. The absence of appreciable radial entrainment is apparent; the trailing column is mostly surrounded by stationary fluid.

The implication is that if the objective is to maximize mixing, it is best to avoid producing the trailing column, so that entrainment can be maximized. A vortex produced with stroke ratio equal to the formation number, entrains the most ambient fluid, for a given amount of fluid in the nozzle. The volume of fluid required for stroke ratio equal to 6, is three times the volume required to create a single vortex ring of stroke ratio 2. The above results suggest that it would be better to create three successive vortex rings with $L/D = 2$, or two successive vortex rings of stroke ratios equal to 3.6 (formation number) and 2.4, instead of a single vortex ring with $L/D = 6$. This conclusion, of course ignores any interaction between the rings.

2.3.2.3 Rate of mixing

Figure 2.10(a) shows the time variation of the total volume of scalar–containing fluid (V_{sc}) for stroke ratios equal to 2 and 6. V_{sc} is computed as the sum of all volume elements which have scalar concentrations above a threshold value (set to 0.01) in the domain above the nozzle exit plane ($y/D > 0$). The threshold value of scalar–concentration allows the difference between the scalar containing fluid and unmixed ambient fluid to be represented. V_{sc} can be considered as a measure of the spread of the scalar in the flow–field. Figure 2.10(a) shows that V_{sc} increases nearly linearly (at a rate of 1.7) until $t^* \sim 2$. In general, V_{sc} increases due to diffusion of scalar from the boundaries of the ring, and mixing of entrained ambient fluid inside the vortex ring. During the very short time ($t^* \leq 2$) of ring formation, entrainment of ambient fluid dominates, as discussed earlier. The linear rate of increase in V_{sc} is therefore, mostly a result of mixing of ambient fluid with nozzle fluid, in the toroidal core of the ring.

After the inflow stops ($t^* > L/D$), V_{sc} further increases, as shown in figure 2.10a. This increase is also nearly linear, and its slope, $\frac{dV_{sc}}{dt^*}$ yields the rate of volume mixing when the vortex ring propagates. Figure 2.10(b) plots $\frac{dV_{sc}}{dt^*}$ after formation ($t^* > L/D$) for different stroke ratios. Note that the rate increases linearly with

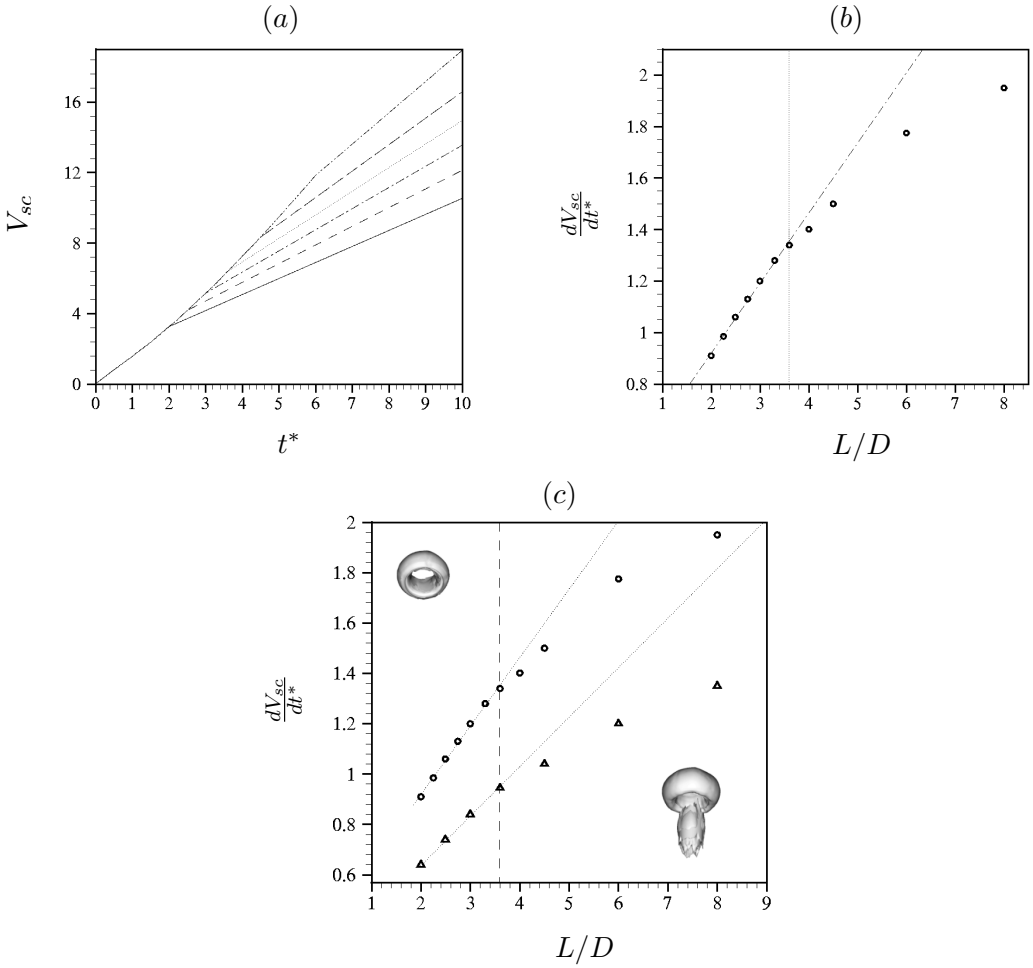

Figure 2.10: (a) Plot of volume of scalar carrying fluid with time for different stroke ratios: ——— , $L/D = 2.0$; - - - - , $L/D = 2.5$; —·— , $L/D = 3.0$; ····· , $L/D = 3.6$; – – – , $L/D = 4.5$; —··— , $L/D = 6$. (b) The rate of scalar volume after formation is plotted against the stroke ratio. The dotted line separates the two regime of flow - stroke ratio less than formation number and higher than formation number. (c) Again, the rate of scalar volume is plotted against the stroke ratio for two different Schmidt numbers: ∘, $Sc = 1$; △, $Sc = 10$. The corresponding flow structures (iso–surface of vorticity) are also shown for the two regimes.

stroke ratio until the stroke ratio equals the formation number. For stroke ratios greater than the formation number, the rate falls below the linear curve. The deviation increases with increasing stroke ratio, and may be explained as follows.

Recall that stroke ratios smaller than the formation number yield a vortex ring without trailing column. The size of the vortex ring increases with increasing stroke ratio, until the formation number is reached, since nearly all of the nozzle fluid goes into the vortex ring. The largest possible vortex ring is therefore produced at the formation number. This increase in ring size results in an increased rate of mixing. As the stroke ratio increases beyond the formation number, the flow field consists of the leading vortex ring, and a trailing column. Increasing the stroke ratio does not change the leading vortex ring; it only increases the length of the trailing column. The overall entrainment may be thought to be a combination of entrainment by the leading vortex ring, and entrainment by the trailing column. The relative contribution of the leading vortex ring to the overall entrainment therefore decreases as the stroke ratio increases. Recall that the trailing column does not entrain fluid as effectively as the vortex ring. This results in an overall decrease of entrainment as the stroke ratio increases beyond the formation number.

The qualitative dependence of the rate of change of scalar carrying fluid on stroke ratio is found to be independent of Schmidt number Sc. Figure 2.10(c) shows results for Schmidt numbers of 1 and 10. Even for $Sc = 10$, the rate increases linearly with stroke ratio until formation number, and deviates away from the linear curve for stroke ratios higher than formation number. The scalar diffuses less at higher Schmidt number, which leads to lower rate at the same stroke ratio. Since entrainment does not depend on Schmidt number, the qualitative behavior of the curves shown in figure 2.10(c) do not change with Schmidt number.

2.4 Summary

Direct numerical simulation of passive scalar mixing in vortex rings is performed, and the effect of stroke ratio on entrainment and mixing is examined. Computed results for circulation and formation number agree well with experimental values. Instantaneous scalar profiles inside the vortex rings are used to contrast the mixing in vortex rings whose stroke ratio is smaller than the formation number, to rings whose stroke ratio is greater. The results show the spiral roll–up of nozzle fluid, and its mixing with entrained ambient fluid in the toroidal core of the ring. As the ring forms, it rapidly entrains ambient fluid from the near–field of the nozzle exit. For stroke ratios greater than the formation number, this entrainment is totally absent in the trailing column. The rate of change of scalar–carrying fluid after ring formation was examined, and seen to vary linearly with stroke ratio until the formation number is reached. As the stroke ratio increases beyond the formation number, the rate increasingly deviates away from the linear curve. This suggests that generation of the trailing column is best avoided, if the objective is to entrain and mix as much as ambient fluid as possible.

Chapter 3

Vortex ring in crossflow

3.1 Introduction

Chapter 2 described the simulations of vortex rings in stationary fluid. We considered two Schmidt numbers and a range of stroke ratios. The formation number was found to yield the maximum entrainment for both Schmidt numbers. This behavior was explained by noting that the entrainment was a combination of that due to the leading vortex ring, and that due to the trailing column of vorticity. The entrainment by the trailing column was negligible as compared to that by the vortex ring, as a result of which the relative contribution of the vortex ring to overall entrainment decreases beyond the formation number. In pulsed jets in crossflow, the vortex rings created by pulsing interact with the crossflow. We therefore study the effect of crossflow on the dynamics, mixing and entrainment characteristics of vortex rings.

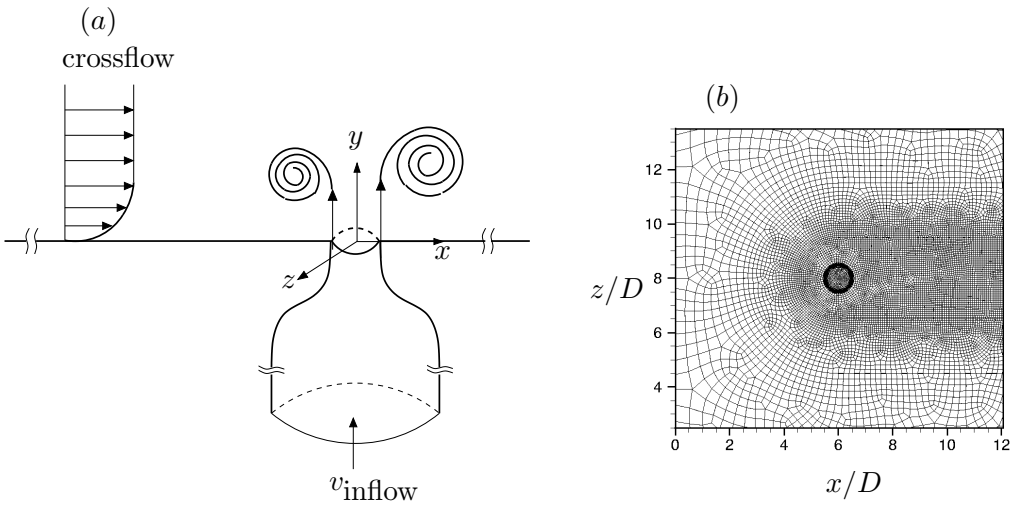

Figure 3.1: (a) Schematic of the problem. (b) Horizontal slice of the mesh.

3.2 Simulation details

3.2.1 Problem statement

Figure 3.1 shows a schematic of the problem, in which a slug of fluid is pushed through a cylindrical nozzle with 3 : 1 diameter ratio. The nozzle fluid forms a vortex ring as it exits the nozzle. The vortex ring interacts with the crossflow which is directed along the $x-$direction. The crossflow is modeled as a laminar boundary layer over a flat plate. Note that the origin of the coordinate system is located at the center of the nozzle exit plane, and the nozzle axis points in the $y-$direction.

In experiments, vortex rings are often generated by a piston pushing a column of fluid of length L through an orifice of diameter D. In simulations, this process is modeled by specifying a top–hat velocity profile (U_{in}) at the nozzle inflow for a duration of time τ (referred to as piston time duration). The inflow velocity is zero for time greater than τ. The stroke length and non–dimensional time are determined using the mean nozzle exit velocity, $\overline{U}_{exit}$ which is equivalent to the piston velocity. The stroke length L is therefore equal to $\overline{U}_{exit}\tau$, and the stroke ratio (L/D) is equal to $\overline{U}_{exit}\tau/D$. The stroke ratio is varied by changing the piston time duration τ. The velocity ratio r_{ring} is defined as the ratio of mean nozzle exit velocity ($\overline{U}_{exit}$)

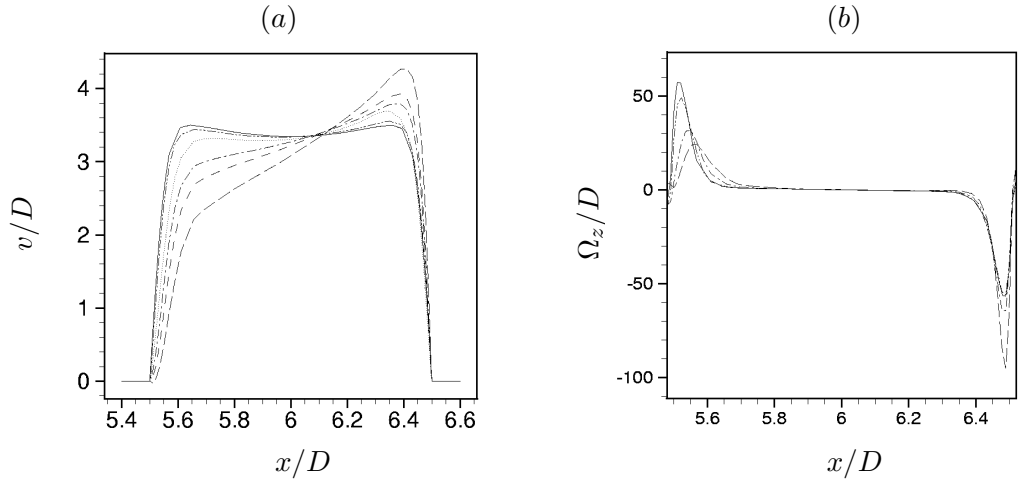

Figure 3.2: (a) v–velocity profiles at the nozzle exit in the symmetry plane at $t^* = \overline{U}_{exit}t/D = 1.0$: —— , without crossflow ($r_{\text{ring}} = \infty$); —·· — , $r_{\text{ring}} = 6$; ····· , $r_{\text{ring}} = 3$; —·— , $r_{\text{ring}} = 2.0$; - - - - , $r_{\text{ring}} = 1.5$; – – – , $r_{\text{ring}} = 1.0$. (b) Corresponding span-wise vorticity, Ω_z/D profiles: —— , without crossflow ($r_{\text{ring}} = \infty$); —·· — , $r_{\text{ring}} = 6$; —·— , $r_{\text{ring}} = 2.0$; – – – , $r_{\text{ring}} = 1.0$.

to the free stream crossflow velocity (U_∞). The velocity ratio is varied by changing the crossflow velocity. DNS of single vortex rings are performed for stroke ratios varying from 1.6 to 8 and crossflow velocity ratios ranging from 1 to 6. The Reynolds number based on $\overline{U}_{exit}$ and nozzle exit diameter (D) is 600 in all cases, except where noted below.

3.2.2 Computational domain & boundary conditions

The computational domain spans $21D \times 20D \times 16D$ above the nozzle exit in the x, y and z directions respectively, and includes a $10D$ length of nozzle. The computational mesh consists of unstructured hexahedral elements. A grid refinement study was performed on grids containing approximately 2.7 million, 3.6 million and 7 million elements. The profiles of nozzle–exit velocity and vorticity for the three grids were examined. The maximum v velocity obtained for the 3.6 million grid differs by 0.6% from the 2.7 million grid. The 7 million grid deviates less than 0.1% from the 3.6 million grid. The vorticity obtained from the 3.6 million grid deviates

less than 0.5% from the 7 million grid. Results from the 7 million grid are presented here. Figure 3.1(b) shows the horizontal cross section of the mesh (with 3.6 million elements for clarity). Very fine mesh elements are used near the nozzle exit and along the direction of the crossflow. The crossflow is simulated as a laminar flow over a flat plate. The velocity field from the self-similar Blasius boundary layer solution is specified at the inflow plane of the crossflow, $6D$ upstream of the nozzle exit. The velocity field is such that in the absence of nozzle fluid, the crossflow has prescribed $\delta_{50\%}$ at the centre of the nozzle exit. On the spanwise boundaries ($z/D = \pm 8$), the velocity field corresponding to laminar crossflow over **a** flat plate is prescribed. Freestream velocity boundary conditions are specified on the top boundary at $y/D = 20$. At the nozzle inflow plane ($y/D = -10$), a top hat velocity profile is specified:

$$v(x, z, y/D = -10, t) = v_{\text{inflow}} = \begin{cases} U_{in} & \text{if } t <= \tau \\ 0 & \text{if } t > \tau \end{cases} \tag{3.1}$$

A zero-gradient boundary condition is used at the outflow ($x/D = 24$).

The numerical schemes used in this chapter are the same as described in section 2.2.2 of chapter 2.

3.3 Effect of crossflow on ring dynamics

When the ambient fluid is stationary, the shear layer that emerges from the nozzle rolls up into an axisymmetric vortex ring. It propagates away from the nozzle and entrains the ambient fluid radially inwards as it does so. The formation number (Gharib *et al.* 1998) marks the transition between two possible flow structures – vortex ring and vortex ring with trailing column of vorticity. A single vortex ring is produced for stroke ratios less than the formation number, while a vortex ring with trailing column is produced for larger stroke ratios.

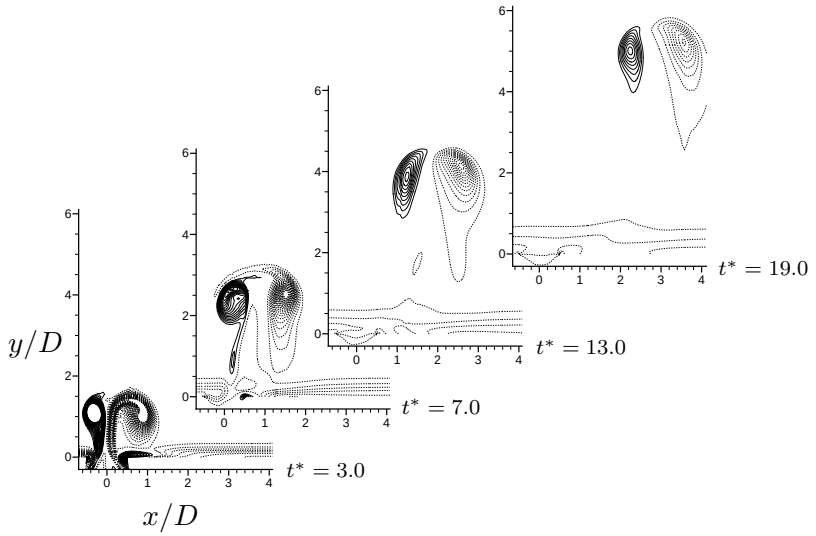

Figure 3.3: Vorticity contours for $L/D = 2$ and $r_{\text{ring}} = 6$ at different time instants. The solid and dashed lines denote positive and negative values respectively.

Both the formation and propagation of vortex rings are affected by presence of crossflow. The crossflow also breaks the axisymmetry of the ring. Figure 3.2(a) shows the nozzle exit velocity(v) profiles at the symmetry plane for different velocity ratios at the same instant of time ($t^* = 1.0$). The exit velocity in the absence of the crossflow is also shown. The crossflow momentum decelerates the nozzle fluid on the upstream side ($x/D = 5.5$). As a result of mass conservation, the fluid near the downstream side ($x/D = 6.5$) accelerates as shown in the figure. The peak velocity on the downstream side increases with increasing crossflow velocity. For $r_{\text{ring}} = 1.0$, there is a very small amount of reverse flow at the upstream side of the nozzle. This is because the adverse pressure gradient outside the nozzle exit overcomes the favorable pressure gradient created by the nozzle throat. Profiles of span-wise vorticity at the nozzle exit in the symmetry plane are shown in figure 3.2(b). Note that vorticity increases significantly on the downstream side due to acceleration of the nozzle fluid. In contrast, the vorticity in the upstream side decreases. Also, the location of peak vorticity on the upstream side shifts to the nozzle right with the increasing crossflow velocity. For very low velocity ratios ($r_{\text{ring}} < 2$), the nozzle

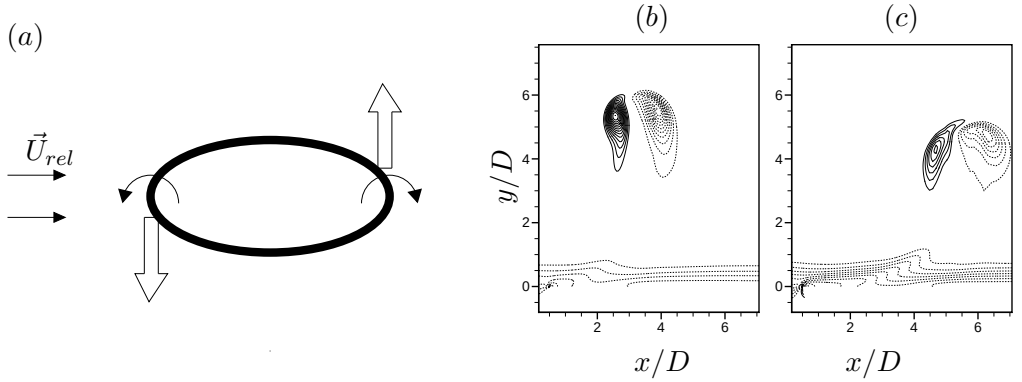

Figure 3.4: (a) Schematic of vortex ring tilting. (b,c) Vorticity contours for $L/D = 2$ at two different crossflow velocities: (b) $u_\infty = 0.5$; (c) $u_\infty = 1.0$. Note that the tilting increases with increase in the crossflow velocity.

shear layer at the upstream side does not roll–up and a complete vortex ring does not form. The low velocity ratio case is discussed in detail in later sections. The following section examines the effect of crossflow on a complete vortex ring. Here, the velocity ratio is greater than 2.

3.3.1 Velocity ratio > 2

For velocity ratio greater than 2, the simulations show that the vortex ring tilts in the presence of crossflow. Tilting is defined in terms of the angle between the plane of the vortex ring and the exit plane of the nozzle. The ring tilts towards the upstream direction for low stroke ratio and tilts towards the downstream for high stroke ratio. This behavior is discussed in more detail below.

3.3.1.1 Low stroke ratio: upstream tilting

Figure 3.3 shows contours of Ω_z vorticity in the symmetry plane (x–y) for stroke ratio 2 and velocity ratio 6 at different instants of time. Note that the vortex ring tilts towards the upstream direction as it penetrates into the crossflow. The induced velocity of the vortex ring opposes the crossflow velocity which helps the ring to penetrate deeper into the crossflow. This behavior is consistent with the

experiments of Chang & Vakili (1995), who observed the upstream tilting of vortex rings in low frequency pulsed jets in crossflow.

The fluid in the vortex ring initially does not have mean horizontal momentum. The relative horizontal velocity between the crossflow and the centroids of the vortex ring combines with ring circulation to produce Kutta–Joukowski lift. It is readily seen that the upstream portion of the ring experiences a downward lift force relative to the downstream portion as shown in figure 3.4(a). As a result, the ring tilts upstream. Note that this reasoning is two–dimensional at every cross–section of the ring. Two–dimensional simulations of a vortex pair in crossflow were therefore performed to test this hypothesis. The vortex pair was found to tilt upstream as observed here. A quantitative discussion of Kutta–Joukowski lift on vortex cores is provided by Ting & Tung (1965) who consider a vortex core of uniform vorticity embedded in a 2D non–uniform stream. They match the near–field and far–field solutions, and use the Kutta–Joukowski theorem to obtain the resulting force on the vortex. Figures 3.4(b) and 3.4(c) show vortex rings of stroke ratio 2 in velocity ratios of 6 and 3. Note that the tilting increases with increase in the crossflow magnitude. This behavior is consistent with the Kutta–Joukowski lift being responsible for the tilting.

The vortex ring also deforms in the presence of crossflow. The thickness of the ring becomes non-uniform as it propagates into the crossflow. Figure 3.5(a) shows λ_2 surface of the vortex ring. Note that the downstream side of the ring is thicker than the upstream side. This deformation of the ring can be attributed to the strain field experienced by the ring in crossflow. Figure 3.5(b) plots the in–plane velocity magnitude along a curve which encompasses the circumference of the ring from upstream to downstream side on the plane of the ring. The velocity field around the ring suggests that a positive velocity gradient is set up along the ring on the upstream side and a negative velocity gradient is set up along the ring on the downstream side. The corresponding velocity gradients experienced by the ring

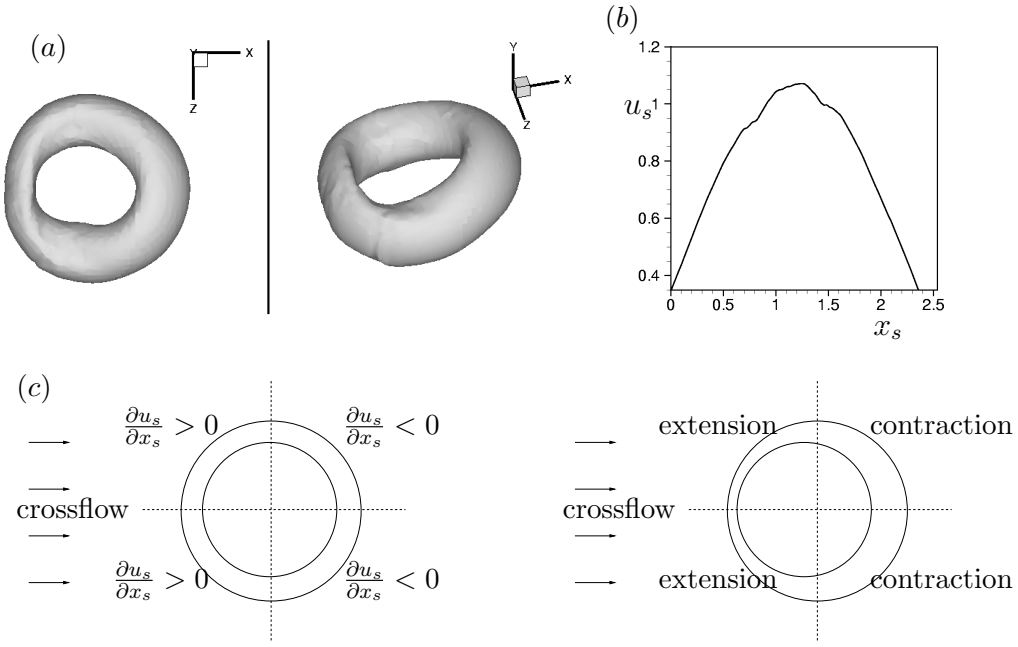

Figure 3.5: (a) λ_2-surface of the vortex ring at a distance of around $4D$ from the nozzle exit for L/D of 2 at $r_{\text{ring}} = 3$. (b) In–plane velocity magnitude on the circumference of the ring from upstream to downstream side. (c) Schematic to illustrate the velocity gradients along the ring.

and the resulting deformation is shown in figure 3.5(c). The upstream side of the ring experiences a positive velocity gradient and stretches as a result. The vortex tube becomes thinner due to stretching. The downstream side exhibits the opposite behavior.

3.3.1.2 High stroke ratio: downstream tilting

For large stroke ratios, vortex rings along with a trailing column of vorticity are generated. Figure 3.6 shows the time evolution of Ω_z contours in the symmetry plane for stroke ratio of 6 and velocity ratio of 6. Note that a vortex ring followed by a trailing column is produced. Also, the leading vortex ring tilts towards the downstream direction, unlike its behavior at lower stroke ratios. One other significant difference is that the ring diameter expands as it propagates downstream (figure 3.6(b)). This behavior is due to the enhanced downstream entrainment of crossflow fluid, which is explained later. The ring's induced velocity has a component along the direction of the crossflow which favors downstream movement. The trailing column acts as an obstacle to the crossflow and as a result, the Kutta–Joukowski lift is not produced. Instead, the crossflow bends the leading vortex ring and the trailing column along the direction of the crossflow; finally the leading vortex ring pinches-off from the trailing column.

For a fixed velocity ratio, the stroke ratio determines whether the ring tilts upstream or downstream. This suggests that there is a *transition stroke ratio* which separates these two regimes. So, the transition stroke ratio for $r_{\text{ring}} = 6$ is sought and the effect of crossflow velocity ratio on the transition stroke ratio is examined.

3.3.1.3 Transition stroke ratio

For a fixed crossflow velocity ratio, the transition stroke ratio is obtained from simulations at different stroke ratios. The transition stroke ratio for $r_{\text{ring}} = 6$ is found to be at $L/D = 3.3$. The vortex ring tilts in the upstream direction for stroke

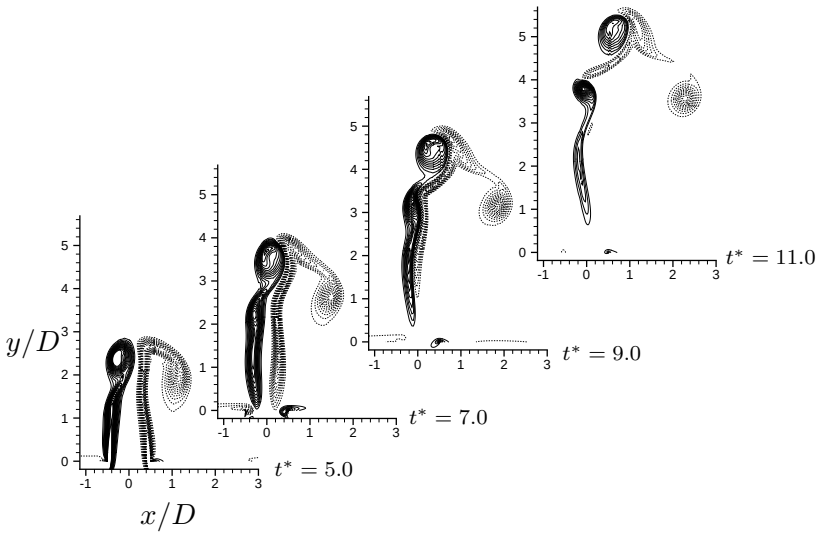

Figure 3.6: Vorticity contours in the symmetry plane for $L/D = 6$ and $r_{\text{ring}} = 6$ at different time instants.

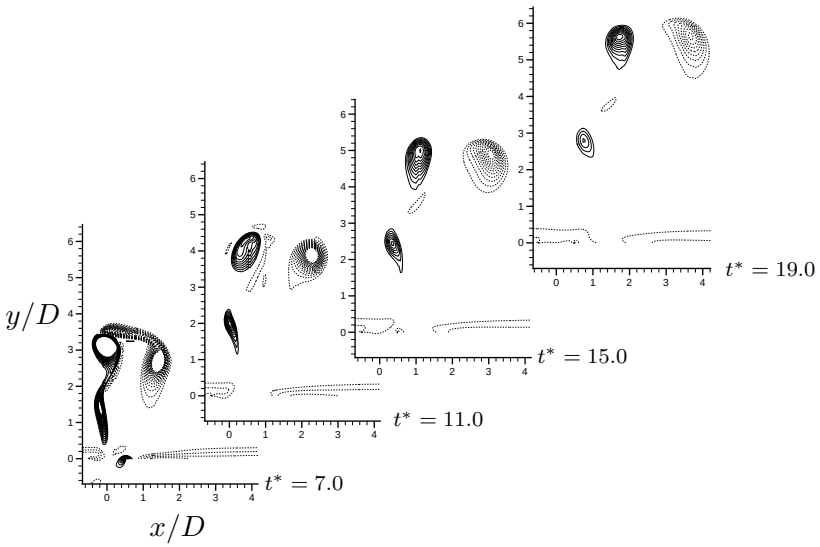

Figure 3.7: Time evolution of vorticity contours at transition stroke ratio ($L/D = 3.33$) for $r_{\text{ring}} = 6$.

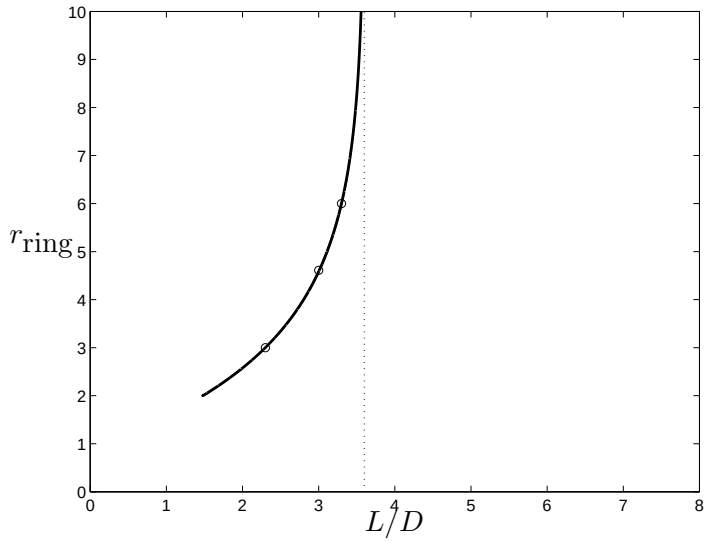

Figure 3.8: The transition curve separates two regimes of flow in the presence of crossflow. The dotted line represents the transition line in stationary flow.

ratios below 3.3. For stroke ratios larger than 3.3, the vortex ring tilts downstream and the ring diameter expands. The ring dynamics at the transition stroke ratio for $r_{\text{ring}} = 6$ are shown in figure 3.7. Initially the leading vortex ring tilts in the downstream direction, but eventually it pinches-off and tilts in the upstream direction slightly.

The effect of velocity ratio on the transition stroke ratio is examined in figure 3.8. For $r_{\text{ring}} = 3$, the transition stroke ratio is found to be 2.3; the transition stroke ratio decreases as the velocity ratio decreases. We estimate a 'transition curve' which defines the transition stroke ratio as a function of velocity ratio. Figure 3.8 shows the three transition stroke ratios obtained at r_{ring} =3, 4.6 and 6 respectively. The ambient fluid approximates stationary fluid when the velocity ratio is increased to very high values. Recall that in stationary fluid, the 'formation number' ($L/D =$ 3.6) defines the transition between single vortex ring and vortex ring with trailing column. So, the transition curve has an asymptote: $L/D = 3.6$. An exponential curve is fitted which passes through the three data points and has an asymptote at $L/D = 3.6$. This yields the transition stroke ratio $(L/D)_{tr}$ as a function of velocity

ratio r_{ring} :

$$(L/D)_{tr} = F_0 - A_1 \exp\left(-A_2 r_{\text{ring}}\right) \tag{3.2}$$

where $F_0 = 3.6$ denotes the formation number in stationary fluid, A_1 and A_2 are constants which are obtained as 5.6 and 0.5 respectively. The transition curve is only plotted for $r_{\text{ring}} > 2$ as shown in figure 3.8. It will be shown later that complete vortex rings do not form for $r_{\text{ring}} < 2$.

The transition curve has important practical consequences. For a particular velocity ratio, stroke ratios on the left of the curve shown in figure 3.8 will generate vortex rings which tilt upstream and penetrate into the crossflow. The stroke ratios to the right of this curve will generate rings which tilt downstream and have a trailing column. It will be shown later that the trailing column significantly improves entrainment in crossflow. In terms of penetration of the rings into the crossflow, stroke ratios around the transition curve will provide maximum opposition to the crossflow. For stroke ratios higher than the transition stroke ratio, the ring–tilting will produce a component of the induced momentum along the crossflow and favor downstream movement of the ring. Shapiro *et. al.* (2006) performed experiments in a pulsed jet in crossflow and reported maximum penetration at two stroke ratios, one in the range of formation number (3.5–4.7) and the other lying in the range 1.8–2.2. Their jet was acoustically pulsed and r_{ring} was equal to 2.58. From our results, it can be inferred that the maximum penetration of the pulsed jet is due to the formation of vortex rings which tilt upstream and penetrate deeper into the crossflow. Note that for a velocity ratio $r_{\text{ring}} = 2.58$, the stroke ratio from the transition curve is approximately 2.0 which is in agreement with the experimental observation of Shapiro *et. al.* (2006).

The above behavior is not significantly affected by the Reynolds number at least in the Reynolds number regime where the rings are stable. Figure 3.9 shows the vorticity field in the symmetry plane for the vortex ring with $L/D = 6$ and $r_{\text{ring}} = 6$

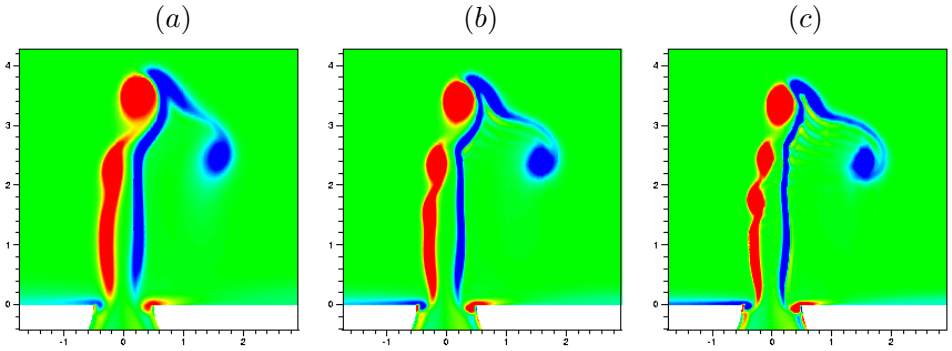

Figure 3.9: Effect of Reynolds number for $L/D = 6$ at $r_{\text{ring}} = 6$: (a) Re=600 (b) Re=900 (c) Re=1300.

at three different Reynolds number. Note that the Reynolds number has almost no effect on the tilting of the vortex rings. As the Reynolds number increases, the vorticity gradients increase and the instabilities in the trailing jet become more pronounced.

3.3.2 Velocity ratio < 2

The increase in crossflow (i.e. decrease in velocity ratio) causes the vorticity in the crossflow boundary layer to increase. Thus, for very low velocity ratios, the vorticity in the crossflow boundary layer starts interacting with the vorticity of the nozzle boundary layer. The interaction is most significant on the upstream side of the nozzle exit. Figure 3.10 shows results for three low velocity ratios: 2, 1.5 and 1. Crossflow boundary layer profiles and vorticity contours in the symmetry plane are shown at $t^* = 1.0$ for each case. Note that roll–up of the nozzle boundary layer is inhibited on the upstream side. The vorticity in the emerging boundary layer is cancelled by the opposing vorticity from the crossflow boundary layer. The vorticity cancellation becomes more pronounced as the velocity ratio decreases. For $r_{\text{ring}} = 1.0$, the vorticity in the emerging nozzle boundary layer is almost annihilated by the crossflow boundary layer as shown in figure 3.10(c). So, a complete vortex ring structure does not form. Instead, a hairpin structure is formed due to the roll

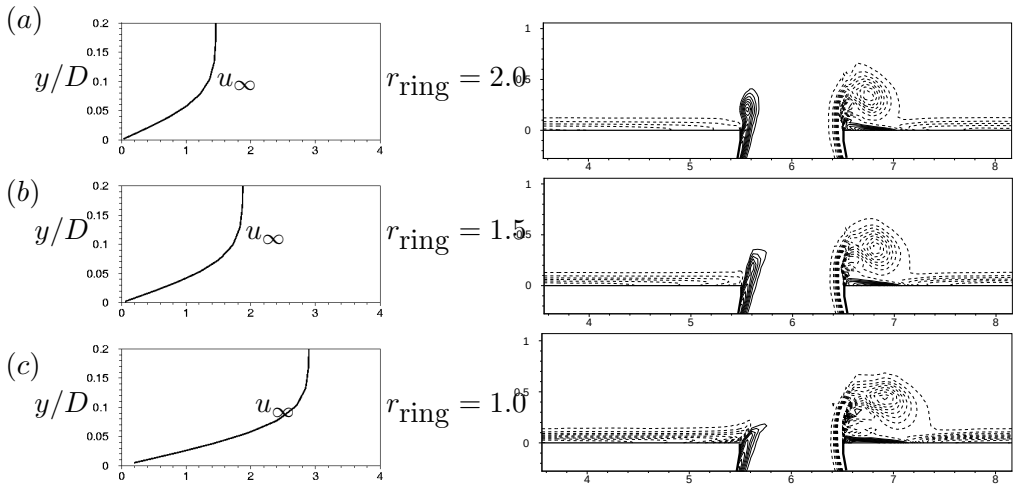

Figure 3.10: Low velocity ratio cases: (a) $r_{\text{ring}} = 2.0$, (b) $r_{\text{ring}} = 1.5$ and (c) $r_{\text{ring}} = 1.0$. Crossflow boundary layer profiles and the vorticity contours in the symmetry plane are shown at $t^* = 1.0$ for each case. Note that the vorticity from the nozzle boundary layers is cancelled by opposing vorticity in the crossflow boundary layer at the upstream side of the nozzle exit.

up on the downstream side alone. This formation of hairpin vortices is similar to that observed in the experiments of Acarlar & Smith (1987) at velocity ratios much smaller than those used in our simulation.

3.3.2.1 Large L/D: hairpin vortex shedding

For low velocity ratios and large stroke ratios, a series of hairpin vortices are shed downstream. Figure 3.11 shows an iso–surface of pressure for $L/D = 5$ and $r_{\text{ring}} = 1.0$. Note that once a hairpin vortex is discharged, then the next hairpin starts to form. This shedding of hairpin vortices is Reynolds number dependent. Figure 3.12 shows vorticity contours in the symmetry plane at different Reynolds numbers: $600, 300$ and 150. The stroke ratio $L/D = 100$ so that the periodic shedding of the hairpins can be observed. Instantaneous contours of vorticity are shown at $t^* = 20$ for each of the cases. Note that for $Re = 600$, the vortices are unstable. For lower Reynolds number, periodic shedding of coherent hairpins is observed as shown. Also, the shedding frequency depends upon the Reynolds number.

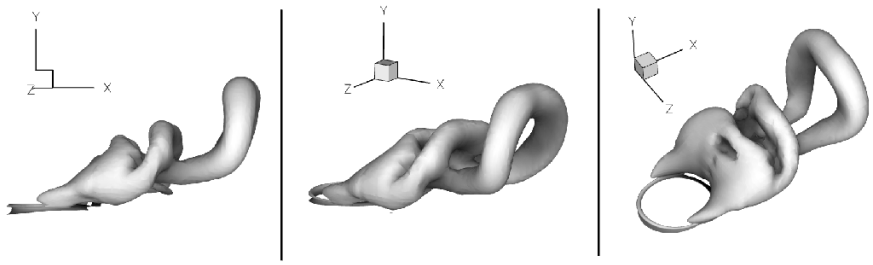

Figure 3.11: Hairpin structures are shed for $L/D = 5$ at $r_{\text{ring}} = 1$. The figures correspond to $t^* = 5.0$.

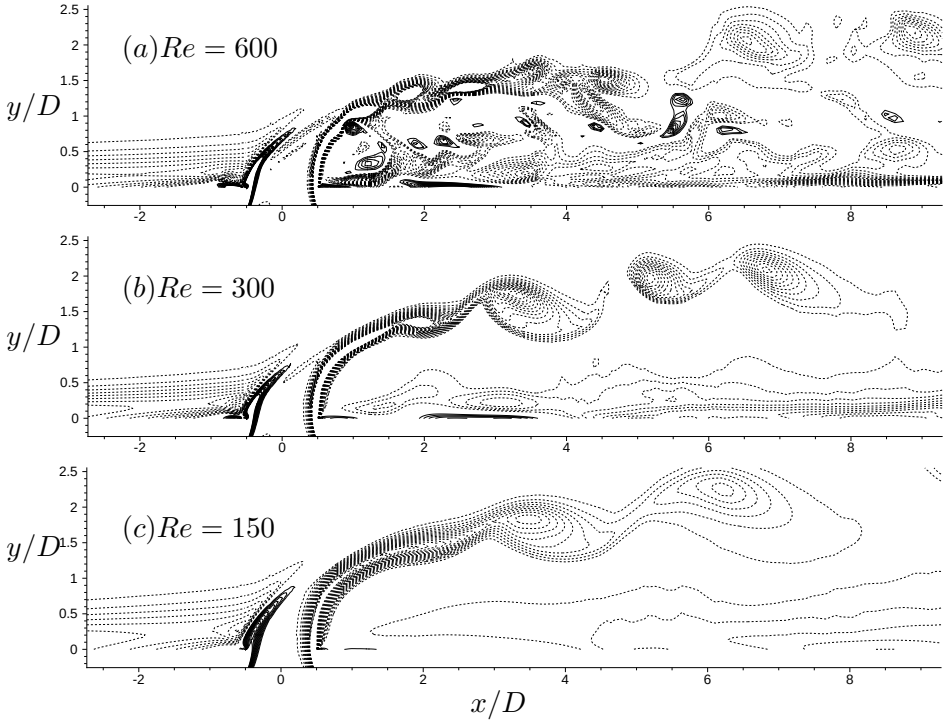

Figure 3.12: Vorticity contours in the symmetry plane at $t^* = 20$ for $r_{\text{ring}} = 1.0$ and $L/D = 100$. (a) $Re = 600$, (b) $Re = 300$, (c) $Re = 150$. Note that shedding of the hairpin vortices is unstable at $Re = 600$. The shedding is very periodic for lower Reynolds number.

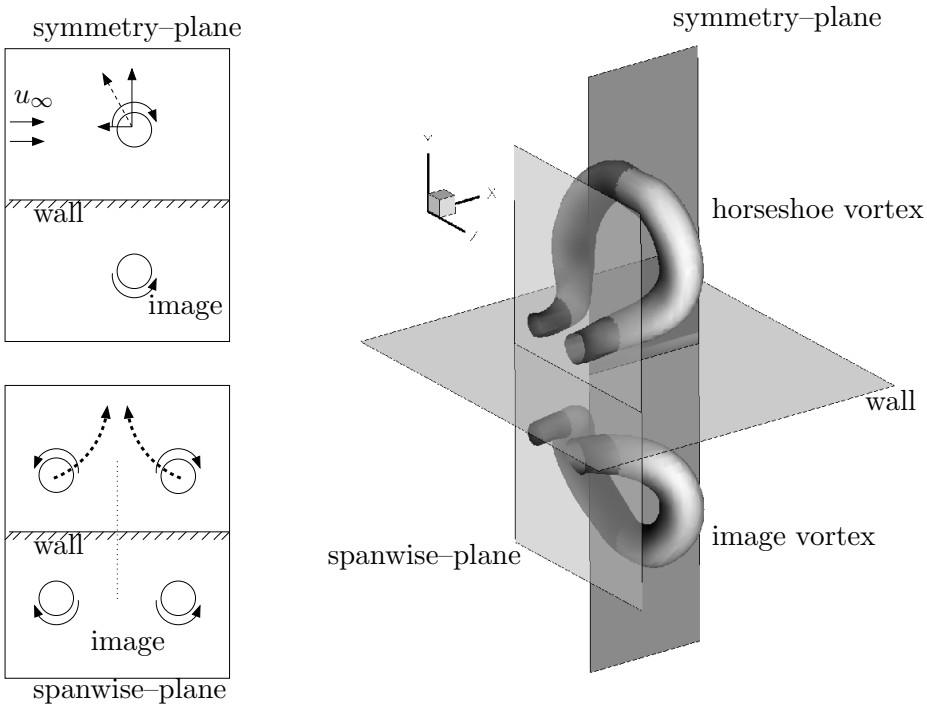

Figure 3.13: Evolution of a hairpin vortex structure in the presence of a wall. The dotted curves in the spanwise–plane show trajectory of the legs due to the wall.

The evolution of hairpin vortices may be explained as follows. Figure 3.13 shows a hairpin structure and its image in the presence of the wall. Schematics of the hairpin cross-sections in span-wise and symmetry planes are also shown. The symmetry plane cuts the 'head' of the hairpin structure. The span-wise plane consists of the counter–rotating legs of the hairpin. The presence of the wall can be modeled by the image–vortices as shown in the schematic. In the span-wise plane, the counter rotating 'legs' follows the path shown in thick-dotted line in figure 3.13. The legs approach each other and also move upwards due to their mutual induction and interaction with the image vortices. On the other hand, the crossflow exerts an upward Kutta–Joukowski lift force on the head of the hairpin and the image vortex induces a negative u–velocity. As a result, the portion around the head of the hairpin tilts as it propagates downstream and becomes normal to the crossflow direction as shown in figure 3.11. The hairpin structure detaches from the emerging shear layer due to the particular motion of the hairpin legs in the presence of the wall. While the hairpin detaches from the shear layer and is shed downstream, the next hairpin is formed.

These results suggests that for very low velocity ratio and low Reynolds number, a steady jet in the presence of a crossflow results in a series of hairpin structures. And if the Reynolds number is very low then the horseshoe-like vortices are shed in a periodic manner. This suggests that at very low velocity ratios, the structure of jets in crossflow is quite unlike the classical structure of jet in crossflow where the counter rotating vortex pair (CVP), a stationary horseshoe vortex, wake vortices and Kelvin–Helmholtz instability vortices characterize the flow (Fric & Roshko 1994). This observation is also consistent with the experiments of Gopalan *et al.* (2004) on a turbulent jet in crossflow at $r_{\text{ring}} < 2$. They report that a semi-cylindrical vortical layer forms behind the jet and suggest that this vorticity starts from the jet shear layer.

3.4 Mixing & entrainment characteristics

The mixing of nozzle fluid with the crossflow fluid is studied by the transport of a passive scalar. The Schmidt number Sc of the scalar is 1.0. Fluid exiting from the nozzle has scalar concentration of 1. The crossflow fluid which initially had scalar concentration of zero, mixes with the nozzle fluid to give intermediate scalar values between zero and one. When the ambient fluid is stationary, an axisymmetric vortex ring entrains the ambient fluid radially inward into the core when it forms. The entrained ambient fluid mixes with the nozzle fluid inside the core. In contrast, the trailing column is surrounded by quiescent ambient fluid and does not entrain the ambient flow. The trailing column is much less effective than a single vortex ring in entraining the ambient fluid and mixing by vortex rings in stationary fluid is optimal at stroke ratio equal to the formation number (Sau & Mahesh 2007). The presence of crossflow changes the mixing and entrainment characteristics completely. As shown above, three different flow regimes exist depending on the velocity ratio and stroke ratio. The different entrainment mechanisms of these three different flow regimes are studied below.

3.4.1 Velocity ratio > 2

Figures 3.14(a) and 3.14(b) show scalar contours in crossflow of $r_{\text{ring}} = 6$ for vortex rings with stroke ratio 2 and 6 respectively. Distinctly different mixing and entrainment behavior can be observed. For the single vortex ring shown in figure 3.14(a), the scalar mixing is almost similar to that in the absence of crossflow. The vortex ring entrains the ambient fluid during its formation. The entrained fluid is mixed with the nozzle fluid inside the core and some of the fluid from the boundary of the vortex ring is deposited behind the ring as the ring propagates. The crossflow introduces an asymmetry between the cores of the ring. Figure 3.14(a) suggests that the core on the upstream side is more mixed than on the downstream side of

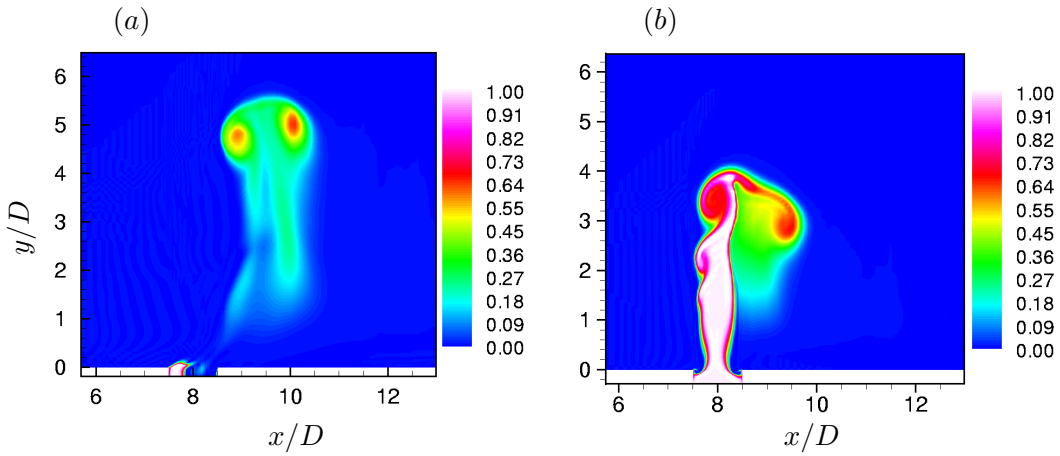

Figure 3.14: Instantaneous scalar contours on the symmetry plane for vortex ring in crossflow with $r_{\text{ring}} = 6$ and L/D of (a) 2 & (b) 6. Note asymmetry in the scalar concentration in the case of small stroke ratio. Also note the enhanced downstream mixing for the case of large stroke ratio.

the ring. This asymmetry in scalar mixing can be attributed to the deformation of the ring as explained in section §3.3.1.1.

For large stroke ratios, scalar contours in 3.14(b) clearly show that the mixing on the downstream side is enhanced significantly. This behavior is similar to that observed in jets in crossflow. As suggested by Muppidi & Mahesh (2006), when a jet encounters a crossflow, the jets bends and the cross–section of the jet deforms. This creates a high pressure gradient directed towards the jet on the downstream side. This pressure gradient drives the flow toward the jet and causes the jet to entrain more fluid on the downstream side rather than the upstream side. Similar flow features are observed in the present case. Figure 3.15 shows an iso–surface of vorticity along with $3D$ streamlines for $L/D = 6$ and $r_{\text{ring}} = 6$. The iso–surface shows the structure of the ring along with the trailing column. It is interesting to observe the streamlines and the deformation of the trailing column cross–section on the downstream side. The streamline clearly show that crossflow fluid goes around the trailing column and is entrained from the downstream side into the trailing column and ring. This downstream entrainment is further enhanced by the low pressure in the core of the vortex ring. This behavior is in contrast to that in the

absence of crossflow where the trailing column does not significantly contribute to overall mixing.

Is there an optimal length of trailing column? For low stroke ratios (no trailing column or very small trailing column), enhancement due to downstream entrainment is absent. On the other hand, for very large stroke ratios, the leading ring would be far away from the high pressure region downstream of the trailing column and would not contribute to enhance the downstream pressure gradient.

3.4.1.1 Optimal downstream pressure gradient

In order to obtain the optimal length of trailing column, the variation of pressure gradient magnitude with the length of the trailing column is computed for velocity ratio of 3. Figure 3.16 plots the contours of pressure gradient magnitude ($|\nabla p|$) in the symmetry plane at different time instants. The figure shows that a high pressure gradient magnitude (denoted by $|\nabla p|_{tr}$) is created on the downstream side of the trailing column. Note that $|\nabla p|_{tr}$ increases till approximately $t^* = 5.0$, following which it decreases. So, for optimal downstream entrainment, the length of the trailing column should be at stroke ratio equal to 5. The effect of the leading ring on the downstream pressure gradient is shown in figure 3.17. The downstream side of the trailing column is enlarged to show the pressure gradient vectors at two different time instants. The time instants are chosen when $|\nabla p|$ is increasing. Note that the pressure gradient vectors rotate towards the right, in the direction of the leading vortex ring.

3.4.2 Velocity ratio < 2

Recall that for very low velocity ratio, a hairpin structure forms instead of a vortex ring, and that a series of hairpins are shed downstream for large stroke ratios. Figures 3.18(c) and 3.18(d) show the scalar contours in the symmetry plane for hairpin structures at $r_{\text{ring}} = 1$ for stroke ratio of 3 and 5 respectively. It is immediately

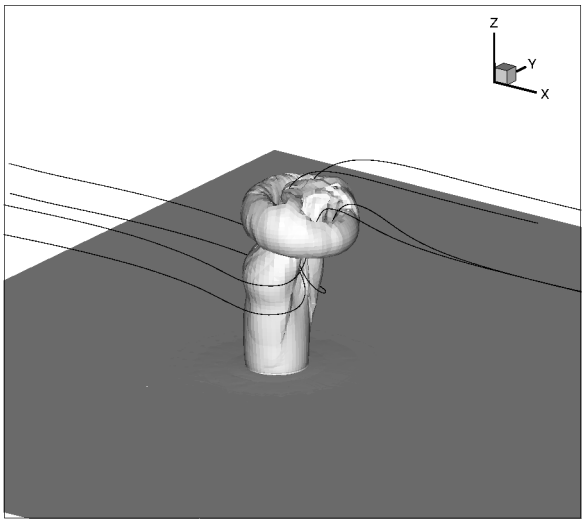

Figure 3.15: Iso–surfaces of vorticity along with some 3D streamlines for $L/D = 6$ and $r_{\text{ring}} = 6$. The stream lines show the downstream entrainment of the crossflow fluid.

apparent that the mixing behavior is quite different from that observed at high velocity ratios. These differences are discussed in detail below.

3.4.2.1 Entrainment by hairpin legs

Figure 3.19(a) shows the hairpin structures for $L/D = 5$ at $r_{\text{ring}} = 1$ along with scalar contour lines on a span-wise plane at $x/D = 1.9$. A streamline emanating from near the nozzle exit is also shown. Figure 3.19(b) shows scalar contours in the span-wise plane ($x/D = 1.9$) which cuts the counter–rotating legs of the hairpin, and some instantaneous streamlines around one of the hairpin leg–core. A very low pressure region is created at the core. The resulting pressure gradient causes the crossflow fluid around the legs to be entrained. This entrainment could also be explained as Biot–Savart induction by the vortex cores in the hairpin legs. The streamlines in figure 3.19(b) show this entrainment of crossflow fluid by the hairpin legs. To further illustrate this behavior, w-velocity and scalar concentration profiles are plotted in figure 3.19(c) along a line passing through one of the core of hairpin

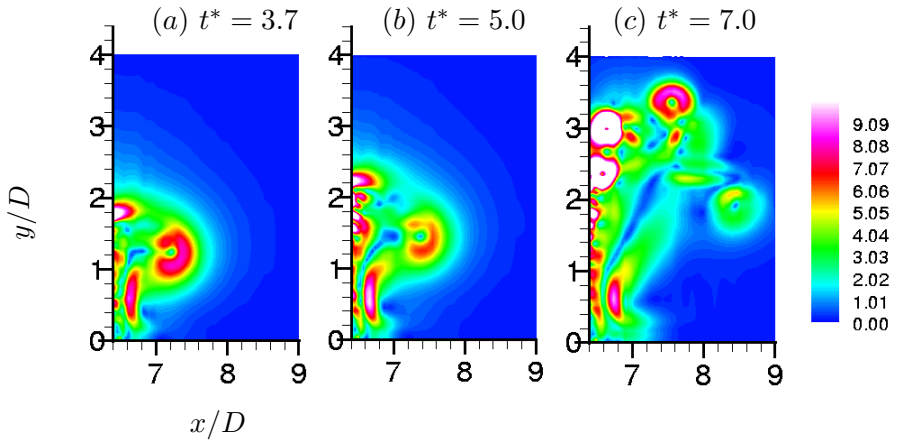

Figure 3.16: Contours of pressure gradient magnitude ($|\nabla p|$) at different times: (a) $t^* = 3.7$, (b) $t^* = 5.0$, (c) $t^* = 7.0$. Note that the pressure gradient magnitude around the downstream of the trailing column is maximum around $t^* = 5.0$.

legs on the span-wise plane at $x/D = 1.9$. The figure shows large levels of w–velocity near the vortex core close to the wall. The scalar concentration of the fluid with strong w–velocity is close to zero, indicating crossflow fluid. An interesting point to note here is that the scalar contours due to the counter–rotating hairpin legs in the span-wise plane appears similar to that the counter rotating vortex pair (CVP), observed in a jet in crossflow. Although in the present case, a CVP does not exist.

3.4.3 Rate of Mixing

The mixing is quantified by computing the rate of change of total volume of scalar after formation. The procedure is similar to that followed by Sau & Mahesh (2007) for vortex rings without crossflow. Figure 3.20(a) shows the total volume of scalar carrying fluid (V_{sc}) plotted against non-dimensional time (t^*) for different stroke ratios and velocity ratio of 3. V_{sc} is computed as the sum of all volume elements which have scalar concentrations above a threshold value (set to 0.01) in the domain above the nozzle exit plane ($y/D > 0$). The slopes of these volume curves after the formation of the ring yield the rate of change of total volume of scalar carrying

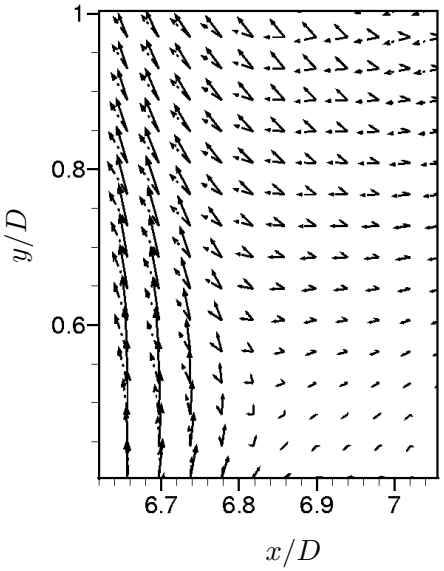

Figure 3.17: Pressure gradient vectors on the symmetry plane near the downstream pressure gradient region at two different time instants. (a) ---- , $t^* = 3.7$; (b) —— , $t^* = 5.0$; Note that the vectors rotate towards the right in the direction of the vortex ring core.

fluid. The rates are shown in Figure 3.20(b) along with the results for rings without crossflow. The figure suggests that the crossflow enhances the mixing in each of the cases. But the enhancement is much higher for larger stroke ratios. This is due to the enhanced downstream entrainment by the trailing column. The percentage increase in entrainment rate for each stroke ratio is shown in figure 3.20(c). For a stroke ratio of 2, the rate of volume change increases only about 20%. The increase is about 40% for stroke ratio of 3 and about 70% for stroke ratio 4.5. The percentage increase in rate appears optimal around stroke ratio of 4.5, which is consistent with optimal downstream pressure gradient.

The behavior for low velocity ratios is different. Figure 3.21 shows the total volume of scalar carrying fluid for different stroke ratios and $r_{\text{ring}} = 1$. Note that the slopes of the curves after formation are nearly equal. The rate of change of V_{sc} in this case is therefore nearly the same at all stroke ratios. This behavior is due to

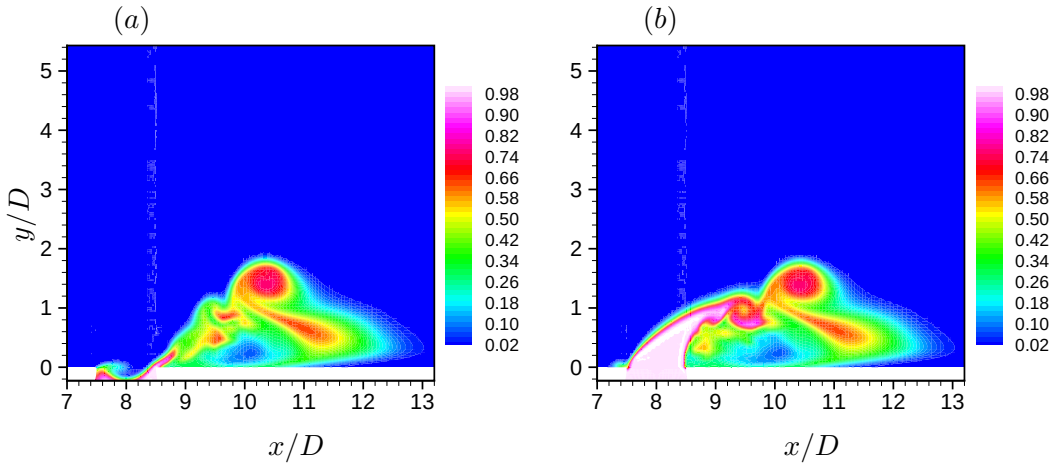

Figure 3.18: Instantaneous scalar contours on the symmetry plane for r_{ring}=1 and L/D of (c) 3 & (d) 5.

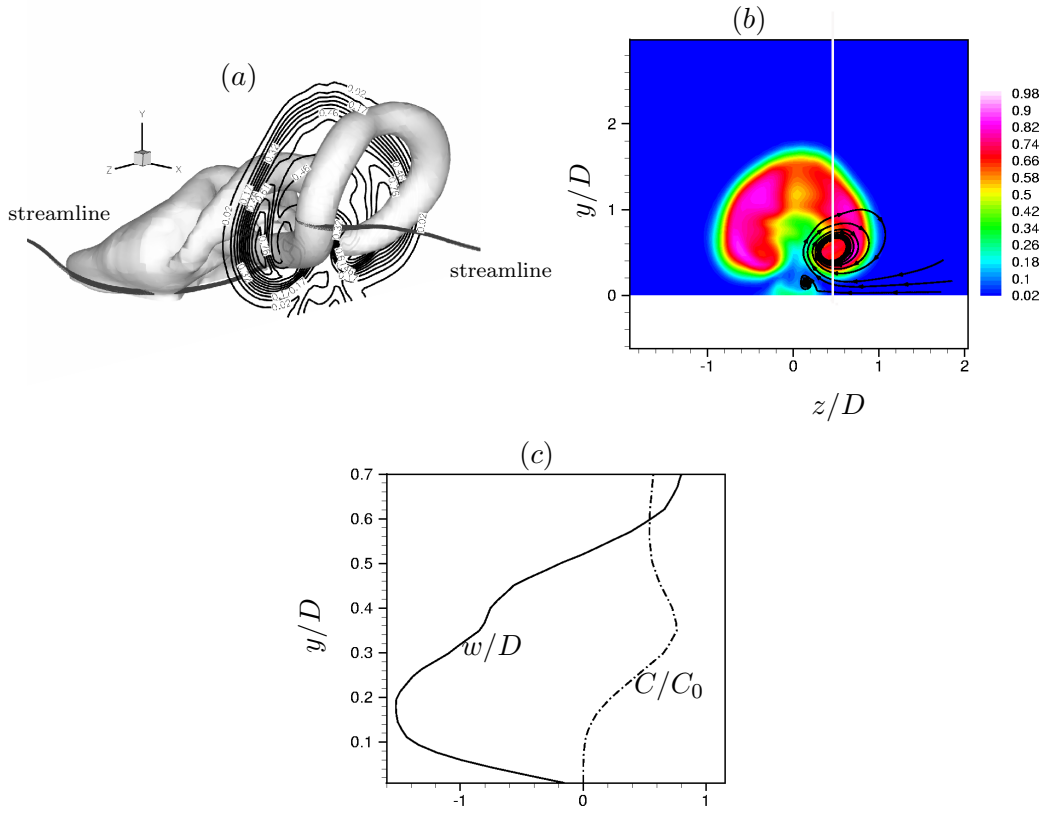

Figure 3.19: Entrainment by hairpin vortex legs. (a) scalar contour lines on a spanwise cross–section of the hairpin legs at $x = 1.9$. (b) The corresponding scalar contour on the spanwise plane along with some in–plane streamlines. (c) spanwise velocity (w/D) and scalar concentration (C/C_0) profiles along a line passing through one of the core of hairpin legs on the spanwise plane.

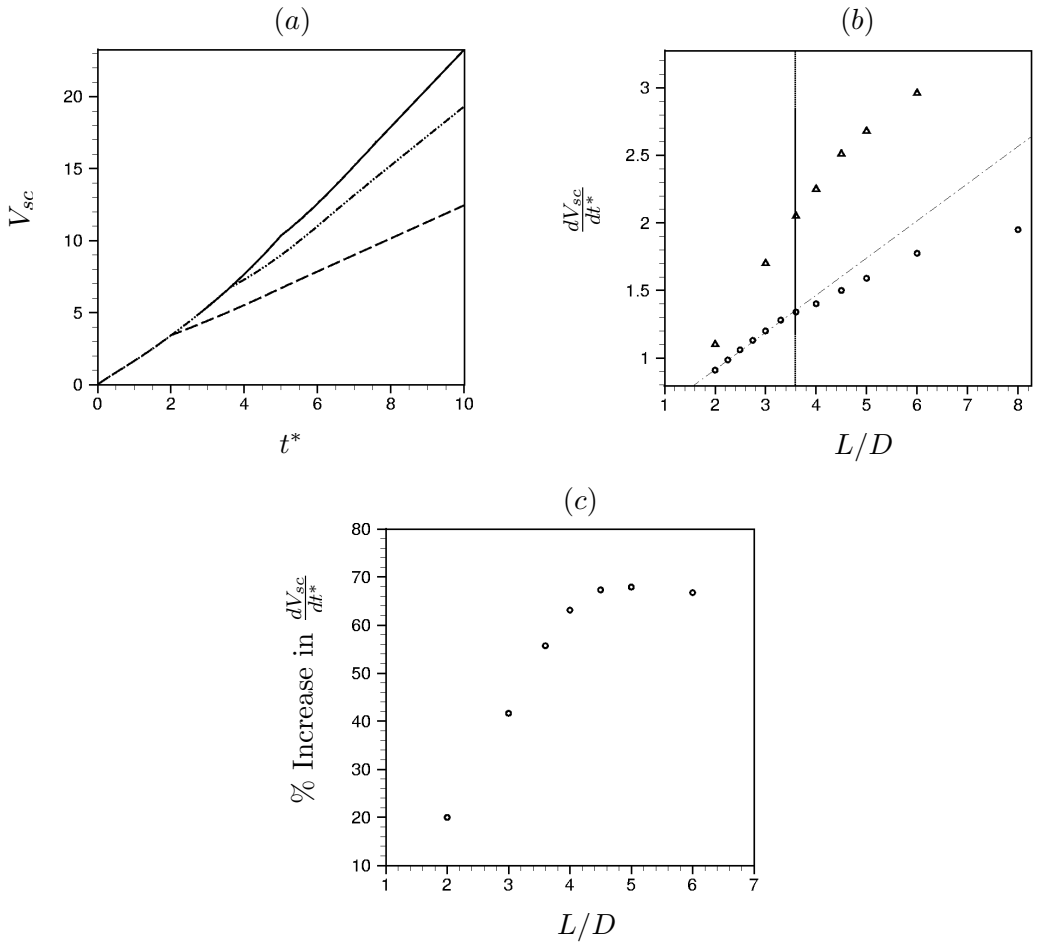

Figure 3.20: (a) Variation of volume of scalar–carrying fluid with time for different stroke ratios and $r_{\text{ring}} = 3$: $---$, $L/D = 2.0$; $—\cdot\cdot—$, $L/D = 3.6$; ——— , $L/D = 5.0$. (b) The rate of change of scalar volume after formation against the stroke ratio for $r_{\text{ring}} = 3$: $\triangle$. The results for the vortex rings in the absence of crossflow are also shown: $\circ$. The vertical line denotes the formation number. (c) Percentage increase in the rates due to crossflow are plotted against the stroke ratio. Note that the percentage increment is maximum around $L/D = 5$.

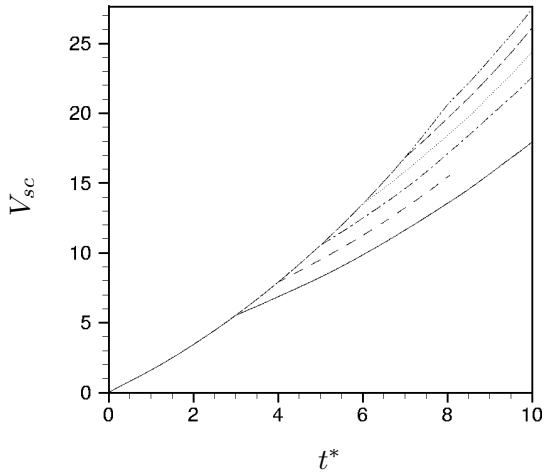

Figure 3.21: Variation of volume of scalar–carrying fluid with time for different stroke ratios and $r_{\text{ring}} = 1$: ——— , $L/D = 3.0$; - - - - , $L/D = 4.0$; —·— , $L/D = 5.0$; ····· , $L/D = 6.0$; – – – , $L/D = 7.0$; —··— , $L/D = 8.0$. Note that the slope of the volume curve after formation is almost the same for all stroke ratios.

the formation of hairpin structures at low velocity ratios. As shown earlier, periodic hairpin vortices are generated at all stroke ratios. Therefore this regime does not have an optimal stroke ratio which maximizes entrainment of crossflow fluid.

3.5 Summary: a regime map

A vortex ring in crossflow can be classified into three different regimes with differing flow structures, mixing and entrainment characteristics. Figure 3.22 shows these different regimes in the space of stroke ratio (L/D) and velocity ratio (r_{ring}). This 'regime map' includes the transition curve for $r_{\text{ring}} > 2$. The transition curve defines the transition from discrete vortex ring (upstream tilting) to vortex ring with trailing column (downstream tilting). As the velocity ratio approaches very high values, the flow field approaches vortex ring in stationary fluid, and consequently, the transition stroke ratio approaches the 'formation number'. Again, as the stroke ratio increases toward very large values, the flow field approaches a jet in crossflow. The regime right of the transition curve is characterized by enhanced downstream entrainment

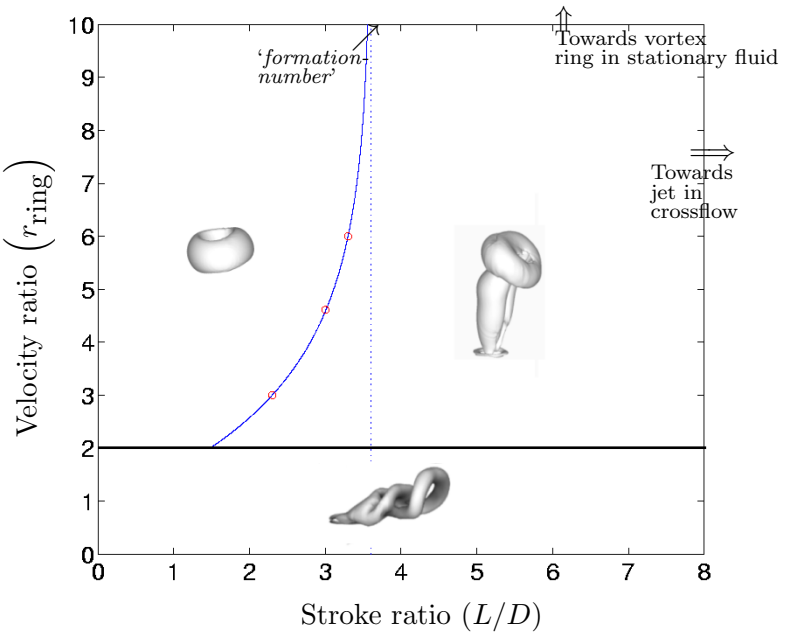

Figure 3.22: A regime map showing three regimes with different flow structure and entrainment characteristics.

due to the trailing column structure. And, for a particular velocity ratio, there is an optimal length of the trailing column. For velocity ratio approximately less than 2, complete vortex ring structures do not form. This regime is characterized by the formation of hairpin–like vortex structures.

The regime map has important implications. It categorizes the complete space of velocity ratio and stroke ratio into three different regimes. A desired flow feature can be attained by choosing the corresponding parameter from the map. Consider pulsation of the jet as a means to control in jets in crossflow. A pulsed jet generates a series of vortex rings. The equivalent stroke ratio of each vortex ring can be easily derived from the pulsing parameters (e.g. Strouhal number, duty cycle, waveform). For example, the equivalent stroke ratio is the inverse of Strouhal number for a fully modulated pulsed jet with 50% duty cycle and square waveform. Thus, for a fixed crossflow, the pulsing parameters can be chosen from the map according to the desired flow structure and entrainment characteristics.

Chapter 4

Pulsed jet in crossflow

4.1 Problem statement

In this chapter, we perform DNS of pulsed jets in crossflow. The pulse is a square wave and the simulations consider several jet velocity ratios and pulse conditions. A fully modulated pulsed jet is injected through a cylindrical nozzle with 3 : 1 diameter ratio (figure 4.1a). The nozzle shape of 3:1 diameter ratio is created using an interpolated B-spline curve. In the symmetry plane, the curve is interpolated using the following points: $(-0.5, 0, 0), (-0.866, -1, 0)$ and $(-1.732, -1.5, 0)$. The origin of the coordinate system is located at the center of the nozzle exit plane, the nozzle axis points in the $y-$direction, and the crossflow is along the $x-$direction. Pulsing causes the nozzle fluid to form a series of vortex rings as it exits the nozzle. These vortex rings interact with the crossflow which is modeled as a laminar boundary layer over a flat plate. A square wave velocity profile is prescribed at the nozzle inflow to simulate a pulsed jet. Figure 4.1(b) shows a typical velocity waveform at the center of the nozzle exit plane. Note that the exit velocity waveform is very close to the square wave prescribed at the nozzle inflow. In experiments, the exit-velocity waveform can be quite different from the prescribed inflow waveform unless some form of control is applied; e.g. M'Closkey *et al.* (2002) use a linear compensator in

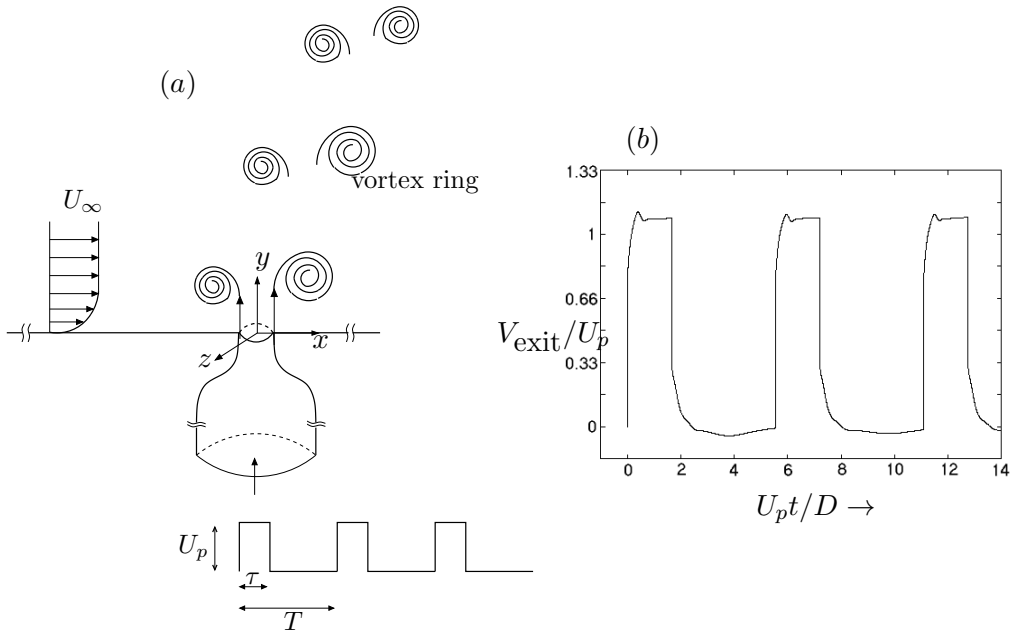

Figure 4.1: (a) A schematic of the problem. (b) Typical waveform at the nozzle exit resulting from a square waveform specified at the nozzle inflow.

their experiments to obtain a square waveform at the nozzle–exit.

4.2 Simulation details

4.2.1 Computational domain & boundary conditions

The computational domain spans $40D \times 40D \times 20D$ above the nozzle exit in the x, y and z directions respectively, and includes a $10D$ length of nozzle. The crossflow is simulated as a laminar flow over a flat plate. The velocity field from the self-similar Blasius boundary layer solution is specified at the inflow plane of the crossflow, $7D$ upstream of the nozzle exit. The velocity field is such that in the absence of nozzle fluid, the crossflow has prescribed $\delta_{50\%}$ at the centre of the nozzle exit. On the spanwise boundaries ($z/D = \pm 10$), the velocity field corresponding to laminar crossflow over **a** flat plate is prescribed. Freestream velocity boundary conditions are specified on the top boundary at $y/D = 20$. At the nozzle inflow plane ($y/D = -10$), spatial profile of the specified velocity is a top hat. A zero-gradient boundary

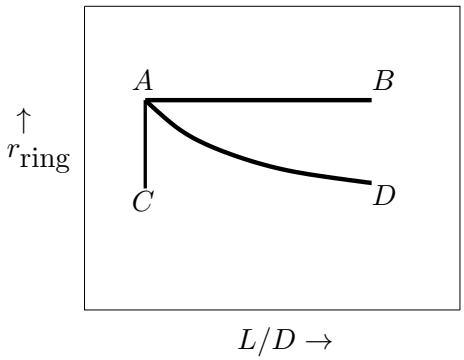

Figure 4.2: Different trajectories in ring parameter space defined in terms of stroke ratio L/D and ring velocity ratio r_{ring}.

Vortex ring regime, $r_{\text{ring}} > 2$.						
Case	r_{ring}	α	Mod.	Optimal St^*	Optimal $\frac{L}{D}^*$	Uncertainty in $\frac{L}{D}^*$
I	8.0	20%	100%	0.28	3.5	±7.1%
II	8.0	30%	100%	0.28	3.5	±7.1%
III	6.0	20%	100%	0.4	2.5	±5.0%
IV	4.5	15%	100%	0.5	2.0	±6.2%
V	4.5	20%	100%	0.5	2.0	±6.2%
VI	3.5	20%	100%	0.67	1.5	±8.3%
VII	10.0	35%	100%	0.28	3.5	±7.1%
VIII	4.5	25%	75%	0.21	2.0	±6.2%

Table 4.1: Simulations performed and corresponding optimal conditions.

condition is used at the outflow.

The numerical schemes used in this chapter are the same as described in section 2.2.2 of chapter 2.

4.2.2 Problem parameters

Figure 4.1 shows a schematic of a square wave pulse. The pulse frequency f may be non–dimensionalized using the mean jet velocity $\overline{U}_j$ (obtained by averaging nozzle exit velocity over the nozzle cross–section in one time period T) and the nozzle exit diameter D. This yields the Strouhal number $St = fD/\bar{U}_j$. Duty cycle α is defined as the ratio of pulse width (τ) to the time period ($\alpha = \tau/T$). Here, pulse width

is the length of time for which the pulse is 'on'. For a fully modulated jet, the inflow velocity is set to zero when the pulse is 'off'. The peak pulse velocity and free–stream crossflow velocities are denoted by U_p and U_∞ respectively. The mean jet to crossflow velocity ratio r_j is defined as the ratio of mean jet velocity $\overline{U}_j$ to U_∞. The Reynolds number based on U_p and nozzle exit diameter (D) is 650 for all simulations except where mentioned.

The properties of the vortex ring produced during each pulsing cycle may be related to the pulse parameters as follows. In experiments, vortex rings are generated by ejecting a column (length L) of fluid though a nozzle (diameter D). Vortex ring formation is therefore determined by the stroke ratio, L/D. For a square waveform, the equivalent stroke ratio, L/D can be obtained from pulsing parameters (e.g. St, α) as follows. In each cycle, $L = \Delta U_j \tau = \Delta U_j \alpha T$, where ΔU_j is the peak–to–peak velocity. Hence, the stroke ratio

$$\frac{L}{D} = \frac{(\Delta U_j)\,\tau}{D} = \frac{(\Delta U_j)\,\alpha}{fD} = \frac{(\Delta U_j)\,\alpha}{\overline{U}_j} \times \left(\frac{\overline{U}_j}{fD}\right) = \frac{(\Delta U_j)\,\alpha}{\overline{U}_j} \times \left(\frac{1}{St}\right). \tag{4.1}$$

In the presence of crossflow, another important parameter is the ring velocity ratio (r_{ring}), which is defined as

$$r_{\text{ring}} = \frac{\Delta U_j}{U_\infty}. \tag{4.2}$$

Note that for fully modulated (100% modulation) pulsed jets, the mean jet velocity, $\overline{U}_j = \frac{1}{T}\int_0^T u\ dt = \Delta U_j \alpha$. This implies that

$$\frac{L}{D} = \frac{1}{St} \text{ for 100\% modulation.} \tag{4.3}$$

$$\frac{L}{D} = \frac{(\Delta U_j)\,\alpha}{\overline{U}_j} \times \left(\frac{1}{St}\right) \text{ for partial modulation.} \tag{4.4}$$

Note that the vortex ring parameters (L/D, r_{ring}) depend on the *deviation of velocity* about the mean velocity. On the other hand, the mean jet velocity ratio depends on the mean jet velocity. This observation allows the vortex ring parameters

to be consistently computed regardless of jet mean velocity ratio and modulation. Equations 4.1 through 4.3 show how different control strategies determine different ring properties. Assuming that $\overline{U_j}$ and U_∞ are fixed, if the duty cycle α is fixed and St is varied, then L/D varies while r_{ring} stays constant – the path AB in figure 4.2. If St is fixed and α is changed, L/D stays fixed and r_{ring} varies (path AC). If both St and r_{ring} vary, then L/D varies along with r_{ring} (e.g. path AD).

For a given jet and crossflow combination $(r_j, \overline{U}_j)$, there are two independent parameters – St and ΔU_j. The parameters traverse paths similar to AD (with varying duty cycle) as in figure 4.2. Simulations are performed for fixed ΔU_j (which results in fixed duty cycle), so that there's only one independent parameter, St. In this case, parameters traverse a fixed path like AB in figure 4.2.

The effect of the oncoming crossflow boundary layer is not studied.

4.2.3 Simulation cases

Table 4.1 lists the conditions for the various simulations performed. For different combinations of ring velocity ratio and duty cycle, the stroke ratio L/D (inverse of St) is varied and an optimal stroke ratio is identified. The combination of cases allows the effect of ring velocity ratio and duty cycle on optimal stroke ratio to be assessed. Note that the ring velocity ratio is varied by varying the free–stream crossflow velocity. So, for a given ring velocity ratio and duty cycle, mean jet to crossflow velocity ratio (r_j) remains constant as St is being varied. St ranges from 2.0 to 0.167 which corresponds to variation of L/D from 0.5 to 6. Table 4.1 also tabulates the optimal L/D and corresponding optimal St at different ring velocity ratios and duty cycles. Optimal St corresponds to the the frequency which results in the maximum overall penetration for a given jet and crossflow combination. The maximum overall penetration is obtained by the maximum y location of vorticity or non–zero passive scalar concentration (both yielded the same condition). The optimal condition is obtained by first narrowing down the range where the optimum

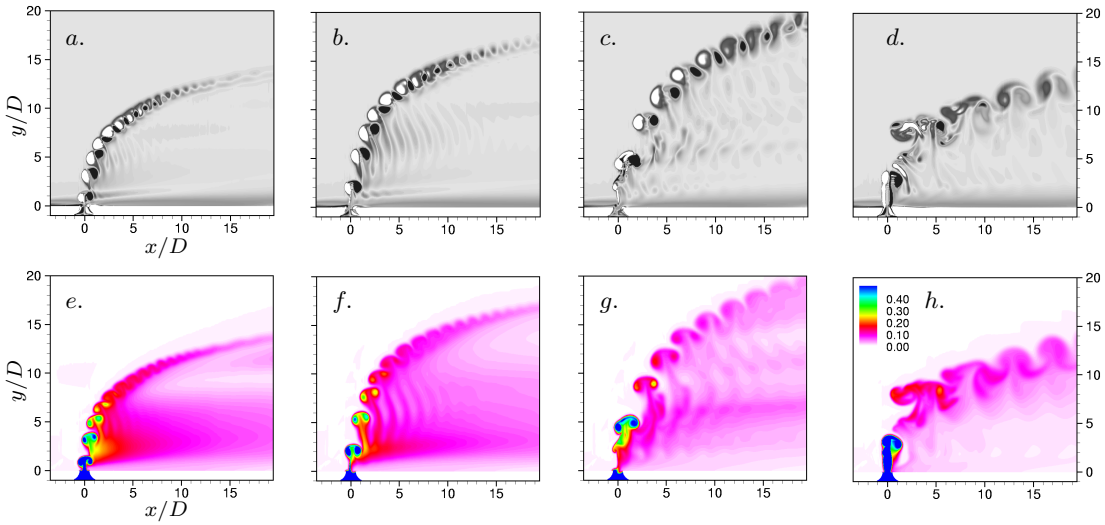

Figure 4.3: Case I: Contours of z vorticity (fig. a–d) and scalar concentration (fig. e–h) in symmetry plane. Ring velocity ratio, $r_{\text{ring}} = 8.0$ and duty cycle, $\alpha = 20\%$ are fixed ($U_p = 3.0, U_\infty = 0.38$). Strouhal number is varied: (a) & (e) $St = 0.714$; (b) & (f) $St = 0.50$; (c) & (g) $St = 0.28$; (d) & (h) $St = 0.167$. Note that maximum penetration is achieved for $St = 0.28$.

lies and then performing additional simulations over that range. For example, figure 5 shows simulation results for case II with L/D = 1.4, 2.0, 3.5 and 6.0 which correspond to St = 0.714, 0.50, 0.28 and 0.167 respectively. However, simulations are also performed for 3.0, 3.25, 3.75, 4.0. In this case, the uncertainty in the optimal stroke ratio is ±7.1%. Table 4.1 lists the uncertainty in optimal stroke ratio for all cases.

4.3 Simulation results for $r_{\mathbf{ring}} > 2$

The behavior of pulsed jets for $r_{\text{ring}} > 2$ is discussed in this section. Optimal pulse conditions at different ring velocity ratios are examined.

4.3.1 A 'typical' simulation

Figure 4.3 shows the flow field corresponding to case I in table 4.1. The ring velocity ratio ($r_{\text{ring}} = 8$) and duty cycle ($\alpha = 20\%$) are fixed while frequency or St is varied:

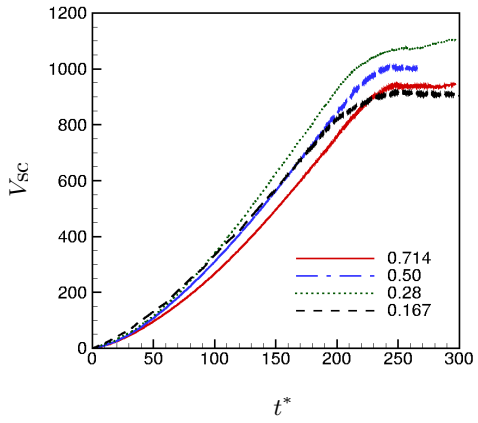

Figure 4.4: Variation of total volume of scalar carrying fluid with time. Ring velocity ratio is 8.0, duty cycle is 20% and several stroke ratios are considered.

(*a*) $St = 0.714$; (*b*) $St = 0.50$; (*c*) $St = 0.28$; (*d*) $St = 0.167$. Contours of ω_z–vorticity (figures 4.3*a*–*d*) and the corresponding scalar contours (figures 4.3*e*–*h*) in the symmetry plane are shown. Note that the pulsed jet produces a series of discrete vortex rings in each of the cases. In figures 4.3(*a*–*c*), upstream tilted vortex rings are produced, and the rings merge and interact further downstream. For $St = 0.167$, in figure 4.3(*d*), vortex rings with trailing column are produced. These rings strongly interact with their trailing column in the near field. Note that as the St decreases from 0.714 (fig.4.3a) to 0.28 (fig.4.3*c*), the jet penetration increases. Further reduction in frequency results in lower jet penetration as observed in figure 4.3(*d*). Thus, there exist optimal pulse conditions which maximize penetration of the jet into the crossflow. The jet penetration is maximum at $St = 0.28$ as shown in figure 4.3(*c*).

In order to quantify mixing, the total volume of scalar carrying fluid is computed. Schmidt number (Sc) of the scalar is 1. Total volume of scalar carrying fluid is computed as the sum of all volume elements which have scalar concentrations above a threshold value (set to 0.01) in the domain above the nozzle exit plane ($y/D > 0$). Figure 4.4 shows the time evolution of total scalar carrying fluid for different St. After the jet exits the domain, the volume of scalar carrying fluid remains nearly

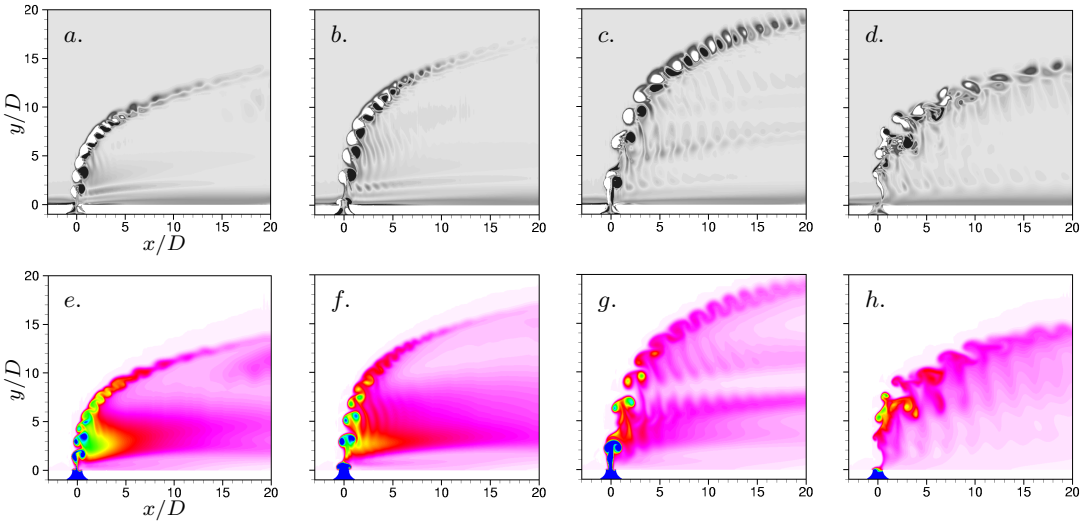

Figure 4.5: Case II: Contours of z vorticity (fig. a–d) in symmetry plane. Ring velocity ratio, $r_{\text{ring}} = 8.0$ and duty cycle, $\alpha = 30\%$ are fixed ($U_p = 3.0, U_\infty = 0.38$). Strouhal number is varied: (a) & (e) $St = 0.714$; (b) & (f) $St = 0.50$; (c) & (g) $St = 0.28$; (d) & (h) $St = 0.167$. Note that maximum penetration is achieved for $St = 0.28$.

constant. Note that optimal conditions extracted from the total volume of scalar are consistent with that obtained from maximum penetration. The total volume of scalar is also maximum at $St = 0.28$. The passive scalar contours (fig. 4.3e–h) reveal an interesting structural feature of pulsed jets in crossflow. Note that (fig. 4.3e–g) that the jet splits in two streams for $St \geq 0.28$. For lower St (e.g. 0.167), no such splitting is observed and only a single stream of the jet is observed (fig 4.5h). In case of splitting, the second stream is formed by the 'wake of the rings' being convected by the crossflow. At lower St, the rings merge in the near–field and the second stream is not pronounced. Fully modulated pulsed jets in crossflow experiments of Eroglu & Breidenthal (2001) reveal similar structural properties and dependence on St. As shown in the simulation, the location of the ring merging moves upstream as St increases. Similar behavior is observed in the experiments. For very high St (e.g. $St > 2$), the pulsed jet behaves similar to a regular jet since the stroke ratio is too small to produce deeply penetrating rings.

4.3.2 Effect of velocity ratio and duty cycle

Figure 4.5 shows simulation results for case II. Here, conditions are similar to case I except the duty cycle is 30% instead of 20%. Figures 4.5(a–d) show contours of ω_z–vorticity and figures 4.5(e–h) show the corresponding scalar contours in the symmetry plane. Note that the rings interact earlier when the duty cycle is 30%. However, the overall behavior is similar to that at the lower duty cycle (20 %). Also, note that varying the duty cycle does not change the optimal Strouhal number. However, for very large duty cycle e.g. $\alpha > 50\%$, there is no optimal pulsing frequency since the rings interact in the very near field irrespective of pulsing frequency. The trajectories at very high duty cycle ($\alpha > 50\%$) are similar to that of a regular transverse jet. This behavior is pronounced at lower ring velocity ratios (3.0–5.0) as discussed later.

The optimal forcing conditions are affected by the ring velocity ratio. Figure 4.6 shows results for case V in table 4.1. The ring velocity ratio is lower (4.5) than the preceding cases discussed and the duty cycle is 20%. Figures 4.6(a–e) show contours of vorticity in the symmetry plane at different Strouhal number: (a) $St = 1.0$; (b) $St = 0.5$; (c) $St = 0.4$; (d) $St = 0.333$; (e) $St = 0.2$. Figures 4.6(f–j) show the corresponding scalar contours in the symmetry plane. Note that the jet penetration varies with the pulsing frequency and maximum penetration is obtained at $St = 0.5$ (fig. 4.6b). This optimal value is higher than the optimal St obtained at $r_{\text{ring}} = 8.0$. Also, note that the jet splits into two streams near the optimal pulsing frequency. The ring interactions are much stronger at these low velocity ratios (such as 4.5) and also the trajectories are lower than the ring velocity ratio of 8.0 (case I & II).

The effect of duty cycle at $r_{\text{ring}} = 4.5$ was studied by performing simulations at varying duty cycle. For example, at 15% duty cycle (case IV), the same optimal St is obtained. As observed for $r_{\text{ring}} = 8$, the optimal forcing does not change when the duty cycle is lowered. As long as the duty cycle is low enough (but non–zero), e.g. $10\% < \alpha < 40\%$, optimal forcing conditions are found to exist and varying the

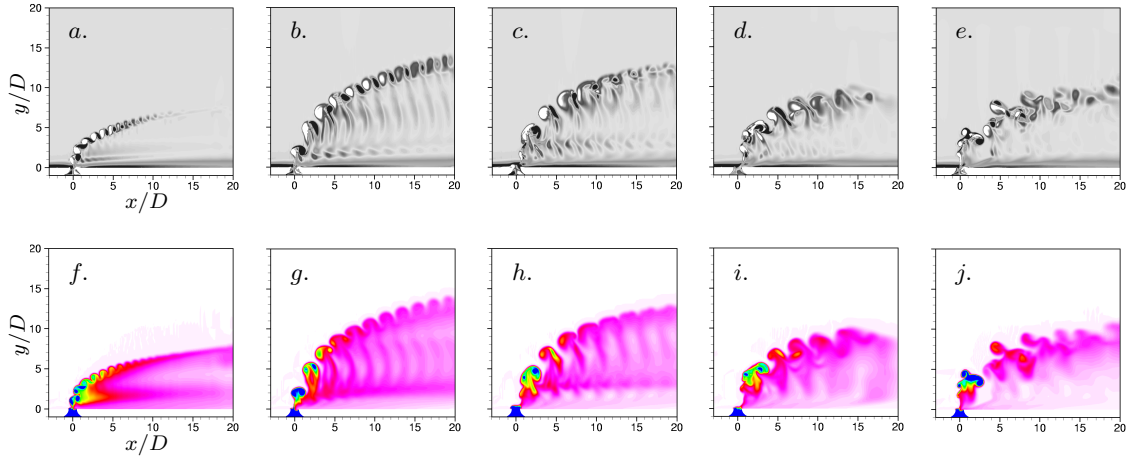

Figure 4.6: Case V: Contours of z vorticity (fig. a–e) and scalar concentration (fig. f–j) in symmetry plane. Ring velocity ratio, $r_{\text{ring}} = 4.5$ and duty cycle is 20% ($U_p = 3.0, U_\infty = 0.67$). Strouhal number is varied: (a) & (f) $St = 1.0$; (b) & (g) $St = 0.5$; (c) & (h) $St = 0.4$; (d) & (i) $St = 0.333$; (e) & (j) $St = 0.2$. Note that the optimal penetration is obtained at $St = 0.5$.

duty cycle only changes penetration difference between optimal and non–optimal cases. For very large duty cycle ($\alpha > 50\%$), the ring interactions occur in the very near field at these low velocity ratios (3.0–5.0) and the trajectories resemble that of a regular jet in crossflow. Simulations were also performed at $r_{\text{ring}} = 6$ (case III) and 3.5 (case VI) as listed in table 4.1. For both velocity ratios, optimal pulse conditions are obtained.

4.3.3 Interpretation in terms of regime map

The preceding section showed that an optimal pulsing frequency exists, when pulsing the jet at fixed ring velocity ratio and duty cycle. These optimal conditions may be interpreted in terms of the the regime map (figure 3.22) for single vortex rings in crossflow (Sau & Mahesh 2008). As discussed in section 4.2.2, the pulsing parameters can be transformed into ring parameters. Recall that a square waveform with 100% modulation yields an equivalent stroke ratio L/D which is the inverse of St. Also recall that if the mean jet to crossflow ratio ($r_j = \overline{U}_j/U_\infty$ and $\overline{U}_j = \Delta U_j \alpha$) is fixed, the product of ring velocity ratio (r_{ring}) and duty cycle (α) is fixed. In each of

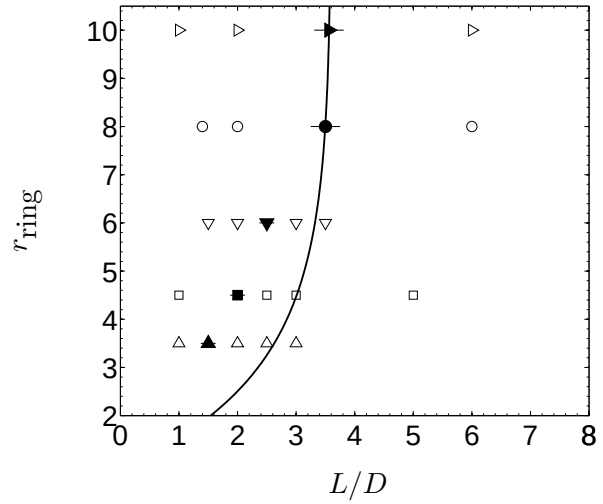

Figure 4.7: Simulation conditions are plotted in stroke ratio and ring velocity ratio coordinates. ∘, case I & II; ∇, case III; ⊓, case IV & V; △, case VI; ▷, case VII. The filled–symbols denote the optimal stroke ratio (table 4.1) at the corresponding ring velocity ratios. The solid curved line denotes the transition curve for a single vortex ring in crossflow. The horizontal bars around the optimal stroke ratios denote the uncertainty in each case.

the cases listed in table 4.1, the time period of the pulse is varied while keeping the pulse velocity fixed. Fixing the pulse velocity (ΔU_j) yields fixed ring velocity ratio (since U_∞ is fixed), and therefore fixed duty cycle. Varying the time period results in variation in stroke ratio. Thus, the pulsing conditions can be transformed into ring parameters and the flow field can be interpreted in terms of the behavior of vortex rings in crossflow.

Consider case I which was discussed earlier in figure 4.3. Here, $r_{\mathrm{ring}} = 8.0$ and the equivalent stroke ratios are: (a) 1.4; (b) 2.0; (c) 3.5; (d) 6.0. These conditions are plotted as circles in the regime map in figure 4.7. The solid circle corresponds to the optimal stroke ratio, $L/D = 3.5$. Note that for stroke ratio less than the transition stroke ratio ($L/D \leq 3.5$ or $St \geq 0.28$) in figure 4.3(a–c), the pulsed jet produces a series of upstream tilted vortex rings without any trailing column of vorticity. Vortex rings with $L/D = 1.4$ and 2.0 (fig.4.3a & 4.3b respectively) contain far less circulation than rings with $L/D = 3.5$ (fig.4.3c). The weaker rings interact

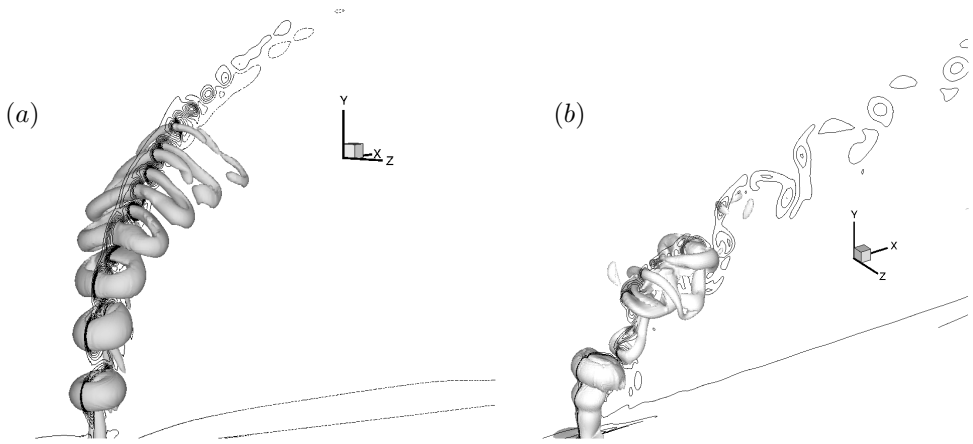

Figure 4.8: (a) Ring interactions. (b) Ring–column interactions.

in the near field and the penetration is less. In figure 4.3(c), the upstream tilted vortex rings contain maximum momentum when L/D approaches the transition stroke ratio, and therefore penetrate deep into the crossflow before interacting with each other. On the other hand, vortex rings with a trailing column of vorticity are produced when the stroke ratio, $L/D = 6$ is higher than the transition stroke ratio (figure 4.3(d), $St = 0.167$). These rings have approximately the same momentum as $L/D = 3.5$ (figure 4.3c), but the trailing columns strongly interact with subsequent ring–column structures in the near field itself. This interaction prevents deep penetration into the crossflow. Optimal penetration is therefore obtained at $St = 0.28$ or $L/D = 3.5$ for $r_{\text{ring}} = 8$. Simulations are also performed at $r_{\text{ring}} = 10$ (case VII). The results are similar to $r_{\text{ring}} = 8$. The optimal condition corresponds to $St = 0.28$ or $L/D = 3.5$ (figure 4.7).

Next consider simulations at $r_{\text{ring}} = 4.5$ (case V, figure 4.6). The equivalent stroke ratios vary from 1.0 (fig. 4.6a) to 5.0 (fig. 4.6b). The equivalent vortex ring parameters are plotted using square symbols on the regime map in figure 4.7. The solid square symbol represents the optimal stroke ratio. Note that the optimum lies left of the transition curve unlike its behavior at the higher velocity ratio discussed above. The same behavior is observed for simulations performed at $r_{\text{ring}} = 6$ (case

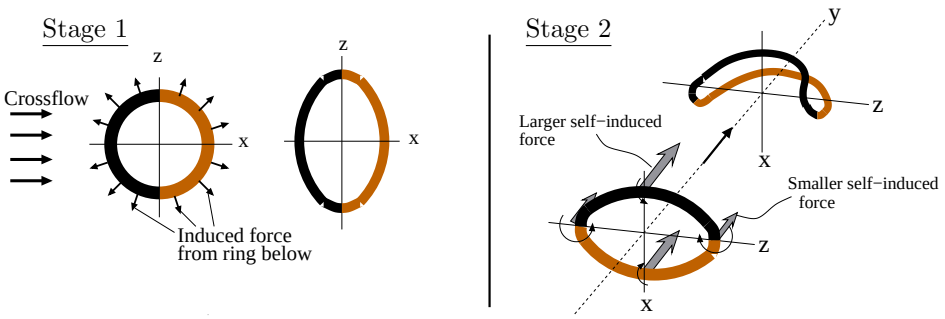

Figure 4.9: Schematic to explain ring deformation.

III) and 3.5 (case VI) listed in table 4.1. These two cases are marked by triangles in 4.7. A curve representing optimal stroke ratios at different velocity ratios can be estimated passing through the points shown in the figure. Note that this curve coincides with the transition curve at higher velocity ratios, and falls to the left of the transition curve at lower ring velocity ratios. The optimal stroke ratio decreases as the ring velocity ratio decreases. Recall that the transition curve represents the transition in structure and tilting for *single* vortex ring in crossflow. The reason for the shift of optimal condition from the transition curve is due to the interaction between successive rings. At low ring velocity ratios, the interaction between successive rings increases as the stroke ratio increases. This mutual interaction is stronger at lower ring velocity ratios.

4.3.4 Ring Interactions

The interaction between successive rings is qualitatively different between the regimes that produce upstream tilting vortex rings and downstream tilting rings with trailing column. In the absence of a trailing column, ring–ring interactions (figure 4.8a) cause out–of–plane stretching and deformation of the rings. Note that as the rings evolve, they stretch in the span-wise direction and deform out–of–plane to develop a 'bow–like' shape. Also, filaments with opposite span–wise vorticity come closer in the stream–wise direction. The evolution and deformation of these ring can be

explained using self- and mutual induction (figure 4.9).

When a single vortex ring exits the nozzle, it tilts upstream as explained in Sau & Mahesh (2008). The subsequent ring will induce a force to expand the upper ring radially outward similar to the leap-frog mechanism of two vortex rings. However, the interaction between the streamwise crossflow and the ring leads to a straining flow in the plane of the ring. The straining flow stretches the ring in the span–wise direction (stage 1, figure 4.9). The ring evolves into a tilted elliptic ring. Marshall & Grant (1994) studied the effect of straining flow on the evolution of vortex rings using linear theory and vortex element method. They suggest that depending on the degree of straining, either the ring alternately elongates in the direction of the stretching and compression of the external flow or the ring monotonically elongates in the direction of the stretching of the external flow without oscillation. In the present simulations, the latter scenario is observed. An elliptic ring has smaller distance between stream–wise filaments; this yields larger self–induced force on the stream–wise filaments and the ring deforms into a 'bow–like' shape in later stages (figure 4.9, stage 2). When a trailing column is present, (figure 4.8b), the ring above the column expands and reduces in speed while the trailing column enters into the ring structure. Even at moderate duty cycle, the trailing column strongly interacts with the ring below it.

4.3.5 Partially modulated pulsed jets

All simulations discussed thus far, consider pulsed jets with 100% modulation; i.e. the minimum jet velocity during a time period is zero. Note that percentage modulation is defined as the ratio of the peak–to–peak jet velocity to maximum jet velocity. The optimal values in figure 4.7 correspond to simulation cases with 100% modulation. For Partially modulated jets the peak to peak velocity difference is fixed and the lower bound of the prescribed jet velocity is nonzero. The equivalent stroke ratio and ring velocity ratio should be based on the peak–to–peak velocity

difference and crossflow free–stream velocity as defined in section 4.2. When defined in this manner, the optimal combination of stroke ratio and ring velocity ratio in partially modulated jet is the same as fully modulated jet (figure 4.7).

An additional set of simulations were performed for a 75% modulated jet with ring velocity ratio of 4.5 as shown in figure 4.10. Contours of z vorticity (fig 4.10a–c) and scalar concentration (fig 4.10d–f) are plotted in the symmetry plane. The Strouhal number St is varied ($St = (a)$ 0.43, (b) 0.21 and (c) 0.11) while keeping the duty cycle ($\alpha = 25\%$) and ring velocity ratio ($r_{\text{ring}} = 4.5$) constant. As discussed in section 4.2, $St = D/L$ for 100% modulation. On the other hand, for partial modulation, the relation will involve the base flow. In this particular case, $St = 0.43 \times D/L$. Figure 4.10(b) shows that optimal penetration corresponds to equivalent stroke ratio of 2. Recall that the optimal stroke ratio was 2 at ring velocity ratio of 4.5 for a fully modulated jet. Thus, optimal conditions can be predicted even for partial modulation using the equivalent stroke ratio and ring velocity ratio as shown in figure 4.7.

Note that in all the cases in figure 4.10(d–f), the scalar contours show multiple streams for the pulsed jet. Even in the regime where the vortex ring has a trailing column (e.g. fig 4.10g, $L/D = 4$), the jet splits in two streams unlike the fully modulated jet. This is because the minimum jet velocity is non–zero for partially modulated jets. So, the jet basically consists of high momentum fluid that generates rings and low momentum fluid that stays close to the wall. The second stream is mainly jet fluid with non–zero jet velocity during the period when the pulse is 'off'.

4.3.6 Effect of 'experimental square' waveform

The simulations are performed using square wave excitation at the nozzle inflow. The corresponding waveform obtained at the nozzle exit is very close to a square waveform, as discussed in section 4.2. However, exit waveforms in experiments are not perfect square waves. The effect of this deviation from a perfect square

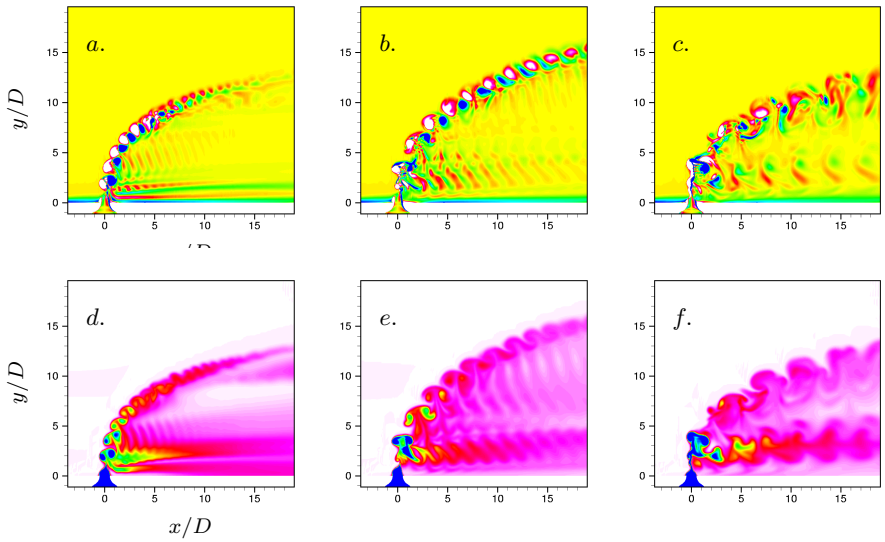

Figure 4.10: The effect of partial modulation (75%). Contours of z vorticity (fig. a–c) and scalar concentration (fig. e–g) in symmetry plane. Ring velocity ratio, $r_{\text{ring}} = 4.5$ and duty cycle is 25% ($\overline{U}_j = 1.75, \Delta U = 3.0, U_\infty = 0.67$). Strouhal number or Stroke ratio is varied: (a) & (d) $St = 0.43, L/D = 1.0$; (b) & (e) $St = 0.21, L/D = 2.0$; (c) & (f) $St = 0.11, L/D = 4$. Note that optimal penetration is obtained at $St = 0.21$ or equivalent stroke ratio of 2 and $r_{\text{ring}} = 4.5$.

waveform is therefore investigated. A simulation is performed with a modified–square waveform corresponding to the experiments of Shapiro *et. al* (2006). Figure 4.11(a) shows the waveform from one of their experiments (fig 3b, page 1295 of their paper). The modified–square waveform (fig. 4.11a) is scaled to yield a stroke ratio of 2 and ring velocity ratio of 4.5. The duty cycle of the waveform is 27%. The equivalent square waveform is shown in figure 4.11(c). Figures 4.11(b) & (d) show span–wise vorticity contours in the symmetry plane for both waveforms. Note that there is hardly any difference in either trajectory or the vorticity field. This is because the flow depends largely on the amount of circulation imparted during the pulse (stroke ratio) and velocity ratio. The circulation is not significantly affected by the deviations from a perfect square waveform in the experiments. The flow fields will therefore be consistent as long as the stroke ratio and velocity ratios are properly computed.

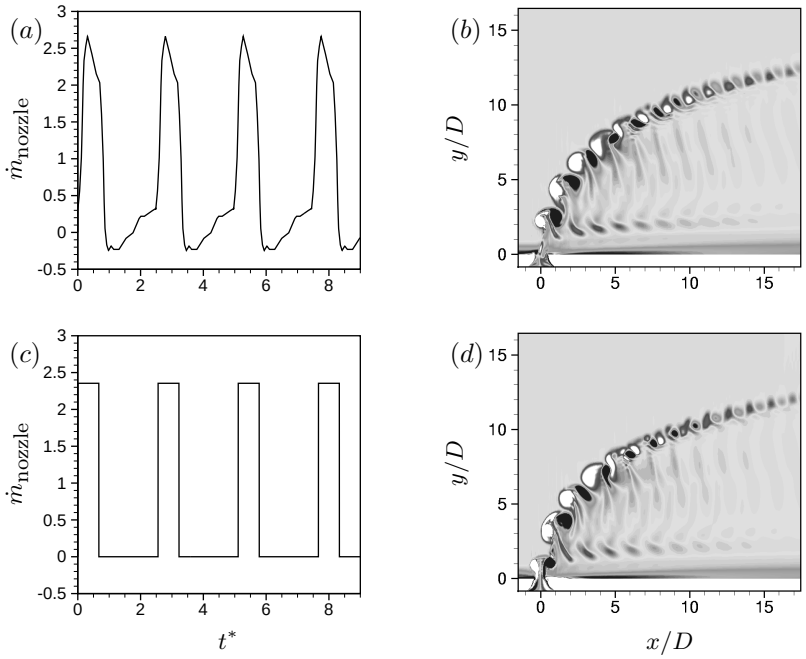

Figure 4.11: (a) & (b) Massflow rate at the nozzle exit and corresponding flow field for a waveform similar to the experiments of Shapiro *et al.* (2006). (c) & (d) Massflow rate at the nozzle exit and corresponding flow field for a square waveform. Both waveforms have the same stroke ratio, velocity ratio and duty cycle.

Case	$\bar{U_j}$ m/s	U_∞	r_j	$U'_{j,\mathrm{rms}}$	Re_j	f	α or τ	τ_{opt} ms
1	2.8	1.1	2.58	1.5	1420	44–147 Hz	10–50%	3.0
4	7.2	1.8	4.0	2.3	3660	87–130 Hz	10–50%	1.6

Table 4.2: Experimental Conditions of Shapiro *et al.* (2006).

4.4 Interpretation of, and comparison to experimental results

In this section, we consider results from several experiments and interpret the optimal conditions in terms of the regime map. We show that the optimal conditions in experiments can be predicted/explained using the stroke ratio and ring-velocity ratio of the equivalent vortex rings. Also, while the optimal St or duty cycles vary over a wide range, the regime map shows good collapse of optimal conditions between the various experiments and the simulations discussed earlier.

4.4.1 Experiment of Shapiro *et al.* (2006)

Shapiro *et al.* (2006) perform controlled experiments of pulsed jets in crossflow. They note that specific combinations of pulse widths and forcing frequencies produce deeply penetrating vortex rings and bifurcating jets, and that the jet penetration is maximum under these conditions. Their experiments consider four different jet and crossflow combinations at two different mean jet to crossflow velocity ratios, 2.58 and 4.0. Table 4.2 lists experimental conditions for two cases denoted by 1 and 4 in their paper with jet velocity ratios 2.58 and 4.0 respectively. For each case, the frequency is fixed and the pulse width is varied such that $U'_{j,\mathrm{rms}}$ is constant (table 4.2). Since frequency is fixed and duty cycle is varied such that $U'_{j,\mathrm{rms}}$ is constant, both stroke ratio L/D and ring velocity ratio r_{ring} vary. As the duty cycle increases, L/D increases and r_{ring} decreases. For each experiment of Shapiro *et al.* (2006), the

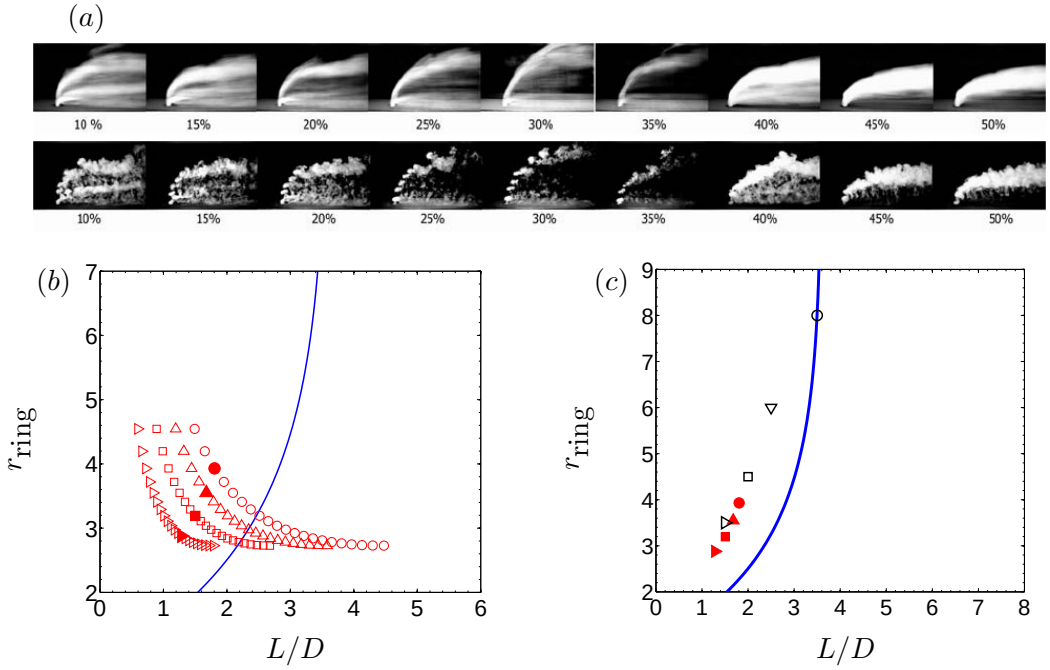

Figure 4.12: (a) Figure 4 from experiment of Shapiro *et al.* (2006), reprinted by permission; mean and instantaneous flow–field (case 1, $U'_{j,\mathrm{rms}} = 1.5$ m/s) with forcing frequency $f = 110$ Hz for duty cycle ranging from 10% to 50%. Maximum jet penetration occurs at 30% duty cycle corresponds to optimal pulse width ($\tau = 3$ ms). (b) The experimental conditions for varying pulse width or duty cycle are transformed in regime map for four frequencies: ○, 44 Hz; △, 55 Hz; ⊓, 73.5 Hz; ▷, 110 Hz. Filled symbols show the optimal conditions ($\tau = 3$ ms) at corresponding frequencies. The solid line denotes the transition curve. (c) Optimal conditions from experiments are compared to simulations. Filled and open symbols correspond to experiment and simulations respectively.

parameters can be transformed into ring parameters and interpreted accordingly.

Figure 4.12 considers case 1 (table 4.2) of Shapiro *et al.* (2006). Figure 4.12(a) reproduces from their paper the mean and instantaneous flow field at 110 Hz when the duty cycle varies from 10% to 50%. Optimal penetration is obtained at duty cycle of 30% with pulse width of 3 ms. The optimal pulse widths at the other frequencies (44, 55, 73.5 Hz) are also reported to have the same value of 3 ms. Figure 4.12(b) shows the corresponding vortex ring parameters for the four different frequencies (44, 55, 73.5 and 110 Hz for case 1) using different symbols. The stroke ratios and ring velocity ratios are computed using the peak–to–peak velocity difference. Note that at a given frequency, as the pulse width increases at fixed $U'_{j,\mathrm{rms}} = 1.5$ m/s, stroke ratio increases and ring velocity ratio decreases. The optimal pulse width of 3 ms for each of these frequencies are denoted by solid symbols. The optimal stroke ratios and ring velocity ratios are also listed in table 4.3. Note that the optimal conditions lie on the left of the transition curve and decrease with ring velocity ratio as shown in figure 4.12(b). In figure 4.12(c), these optimal conditions are compared to optimal stroke ratios obtained in simulations. Note that good agreement is obtained and the experimental optimal conditions follow the same trend as the simulations.

The flow structures in figure 4.12(a) are interesting to observe. Below the optimal duty cycle of 30%, discrete upstream tilted vortex rings are evident. Note that the rings interact in the near field and the penetration is less at lower pulse width or duty cycles (10% to 20%). In these cases, the equivalent stroke ratios are much smaller than their transition value (less than 1) as noted in figure 4.12(b). These rings therefore contain much less circulation, which results in lesser penetration. Around the optimal duty cycle (25% to 35%), upstream tilted vortex rings are produced that penetrate deep into the crossflow before interacting or merging with each other. At even higher duty cycle (40% to 50%), the rings interact in the very near field and the pulsed jet looks more like a steady jet. This behavior is similar to that observed in the simulations in section 4.3.

Frequency Hz	r_j	Optimal τ	Optimal ring parameters	
			L/D^*	r_{ring}
44	2.58	3 ms	1.80	3.93
55	2.58	3 ms	1.68	3.55
73.5	2.58	3 ms	1.50	3.19
110	2.58	3 ms	1.28	2.88

Table 4.3: Case 1 of Shapiro *et al.*; Optimal conditions ($U'_{j,\text{rms}}$ is matched at 1.5 m/s)

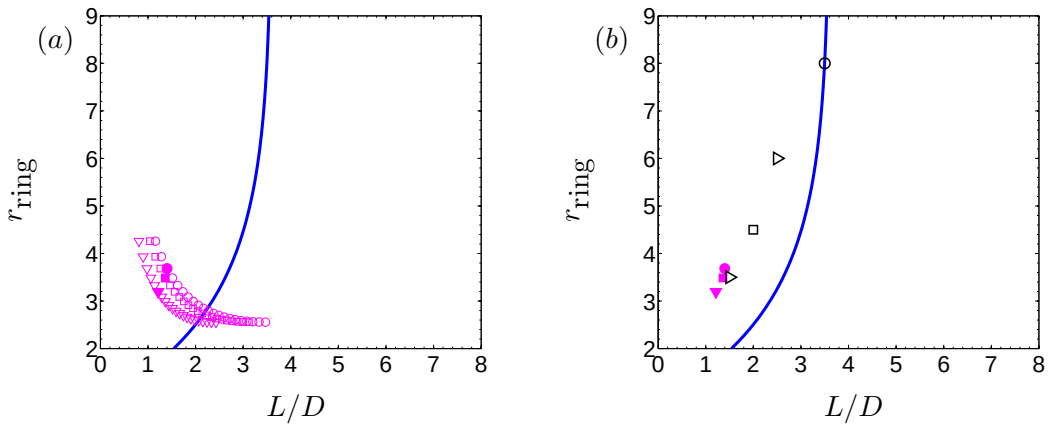

Figure 4.13: (a) Experimental conditions (case 4 of Shapiro *et al.*, $U'_{j,\text{rms}} = 2.3$ m/s) with varying pulse width for different frequencies: ∘, 87 Hz; ⊓, 96.7 Hz; ∇, 124.3 Hz, are plotted in stroke ratio and ring velocity ratio space. Filled symbols show the optimal conditions with pulse width 1.6 ms. Solid line denotes the transition curve. (b) Optimal condition for the experiment is compared with simulations. Filled and open symbols correspond to experiment and simulations respectively.

Frequency Hz	r_j	Optimal τ	Optimal ring parameters	
			L/D^*	r_{ring}
87	4.0	1.6 ms	1.40	3.68
96.7	4.0	1.6 ms	1.34	3.53
124.3	4.0	1.6 ms	1.21	3.19

Table 4.4: Case 4 of Shapiro *et al.*; Optimal conditions ($U'_{j,\text{rms}}$ is matched at 2.3 m/s).

Case 4 in Shapiro *et al.*'s experiments examines optimal pulse width at various frequencies. The experimental conditions for case 4 are listed in table 4.2. The pulse width is varied at fixed frequency such that $U'_{j,\mathrm{rms}} = 2.3$ m/s. In this case, the optimal pulse width is found to be 1.6 ms at all the frequencies. Figure 4.13(a) plots the experimental conditions in the regime map for three frequencies (87, 96.7 and 124.3 Hz) as the pulse width is varied. Note that as the pulse width increases, stroke ratio increases and ring velocity ratio decreases. The optimal conditions are listed in table 4.4 and marked using solid symbols in figure 4.13(a). Figure 4.13(b) compares the optimal experimental conditions to simulation results. Note that good agreement is obtained.

Shapiro *et al.* (2006) also perform experiments where they fix the peak–to–peak jet velocity excitation amplitude ΔU_j and frequency, while varying the duty cycle. Note that as the duty cycle increases for fixed ΔU_j, the stroke ratio increases while ring–velocity ratio stays fixed. Figure 4.14(a) shows the instantaneous flow field for different duty cycles (10% to 50%) at 85 Hz and $\Delta U_j = 4.8m/s$. The experimental conditions for this case are transformed into corresponding vortex ring parameters space in figure 4.14(b). Note that optimal penetration is achieved at duty cycle of 25%. This optimal duty cycle of 25% at 85 Hz corresponds to L/D of 1.8 at $r_{\mathrm{ring}} = 4.36$ (solid symbol in figure 4.14b). The optimal condition is plotted along with the simulation results in figure 4.14(c). Note that good agreement is obtained. The optimal duty cycles for three different frequencies (55, 73.5 and 85 Hz) and the corresponding ring parameters are listed in table 4.5.

4.4.2 Experiment of Eroglu & Breidenthal (2001)

Eroglu & Breidenthal (2001) study fully modulated pulsed transverse jets with square wave excitation at 50% duty cycle. Figures 4.15(a)–(d) show the flow field in their experiments at different pulsing frequencies (a) $St = 0.0$ (steady jet), (b) $St = 0.28$, (c) $St = 0.42$ and (d) $St = 0.71$. The mean jet to crossflow velocity

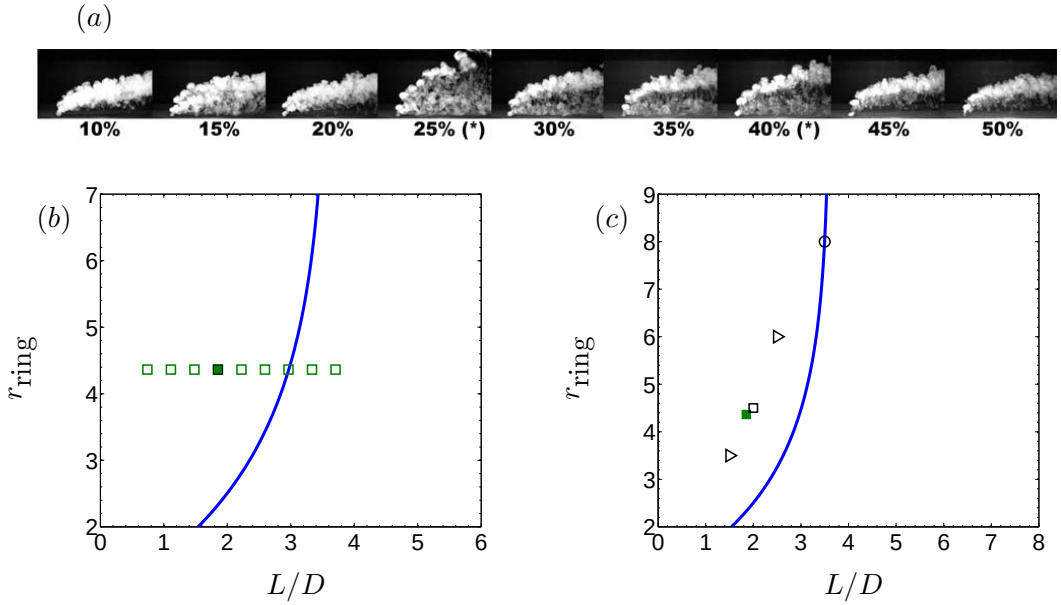

Figure 4.14: (a) Figure 6c from experiment of Shapiro *et al.* (2006), reprinted by permission; smoke visualization for experimental case 1, with peak–to–peak ΔU_j fixed at 4.8 m/s with forcing frequency $f = 85$ Hz for duty cycle ranging from 10% to 50%. Maximum jet penetration occurs at 25% duty cycle. (b) Experimental conditions are plotted in stroke ratio and ring velocity ratio space. Filled symbol shows the optimal condition with duty cycle 25%. The solid line denotes the transition curve. (c) Optimal condition for the experiment is compared to simulations. Filled and open symbols correspond to experiment and simulations respectively.

Frequency Hz	r_j	Optimal α	Optimal ring parameters	
			L/D^*	r_{ring}
55	2.58	15%	1.718	4.36
73.5	2.58	20%	1.714	4.36
85	2.58	25%	1.852	4.36

Table 4.5: Case 1 Shapiro *et al.*; Optimal condition (ΔU_j is matched at 4.8 m/s)

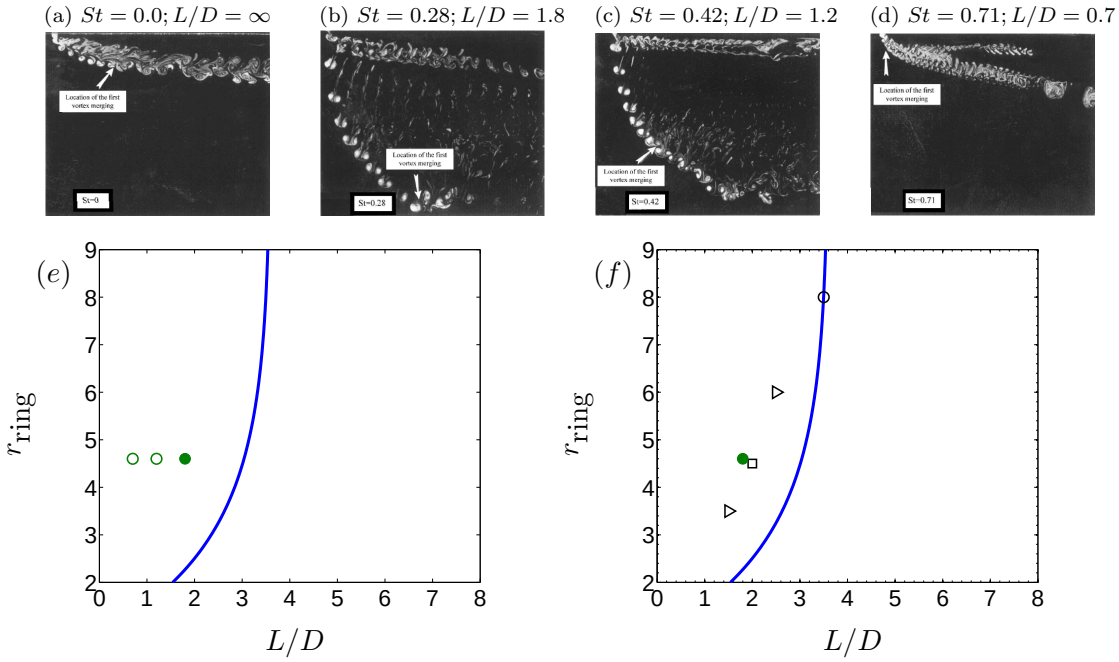

Figure 4.15: Results from the experiments of Eroglu & Breidenthal (2001, reprinted by permission) showing pulsed jets in crossflow at different Strouhal numbers. Figure (a) shows the steady jet, $St = 0.0$. Ring velocity ratio is 4.6 in all cases. The equivalent stroke ratios (L/D) are (b) 1.8, (c) 1.2 and (d) 0.7. Note figure (b) shows the maximum penetration for $L/D = 1.8$.

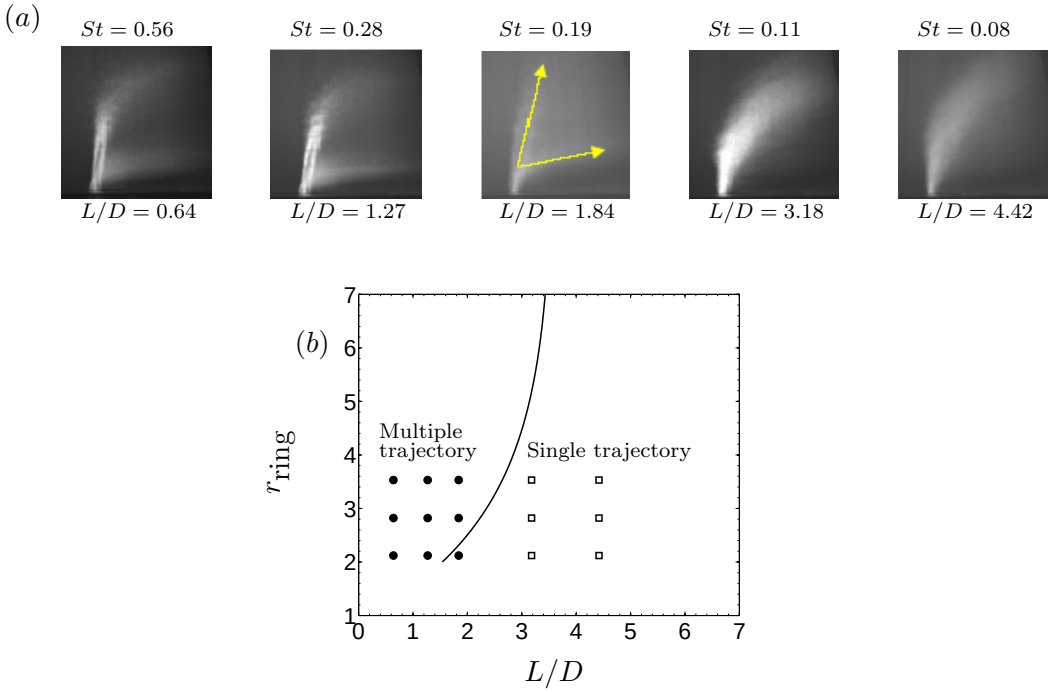

Figure 4.16: (a) Experiments of Tomar *et al.* (2004, reproduced by permission) on ZNMF–JIC reveal that for $St >= 0.19$ (corresponds to $L/D <= 1.84$) the mean jet structure has multiple trajectory and for $St < 0.11$ ($L/D > 3.18$) the jet has single trajectory. The equivalent ring velocity ratio for this case correspond to 3.53. (b) Symbols correspond to transformed experimental data in ring parameter space. Filled and open symbols correspond to multiple and single trajectory structure respectively.

ratio is fixed at 2.3 which corresponds to a ring velocity ratio of 4.6. The equivalent stroke ratios for these cases are shown in figures 4.15(a)–(d). It is clear that discrete vortex rings are produced at $St = 0.28$ which penetrate the crossflow in the near field and interact/merge further downstream. Also the jet splits in two streams. As the frequency is increased to $St = 0.42$, the location of the first interaction shifts upstream and the jet penetration is lower. Again, as the frequency is increased to $St = 0.71$, the rings interact in the very near field and the penetration is much lower than the other two cases. This behavior is consistent with that observed in the simulations. The experimental conditions are transformed onto the regime map in figure 4.15(e)–(f). Note that the stroke ratio for optimal penetration lies very close to the optimal stroke ratios obtained in the simulations.

St	L/D	Mean structure
0.08	4.42	single trajectory
0.11	3.18	single trajectory
0.19	1.84	multiple trajectory
0.28	1.27	multiple trajectory
0.56	0.64	multiple trajectory

Table 4.6: Experiments ZNMF-JIC (Tomar *et al.* 2004)

4.4.3 Zero–Net–Mass–Flux Jet in Crossflow by Tomar *et al.* (2004)

Tomar *et al.* (2004) study the effect of Strouhal number and velocity ratio on the mean structure of Zero–Net–Mass–Flux Jets in Crossflow (ZNMF–JIC) using planar laser induced fluorescence. Experiments are performed for velocity ratios ranging from 2–5 and Strouhal numbers varying from 0.08 to 0.56. They observe two distinct flow regimes depending on St as shown in figure 4.16(a). Figure 4.16(a) shows the mean structure of the jet as St is varied at velocity ratio of 5. A single mean jet trajectory is observed for $St < 0.11$ and multiple trajectories are observed for $St > 0.19$. Tomar *et al.* (2004) also suggest that the multiple trajectory ZNMF–JIC penetrates more deeply into the ambient crossflow. Table 4.6 lists the vortex ring parameters computed for their experiments. The equivalent stroke ratio ranges from 0.64–4.42 and the ring velocity ratio varies from 1.41–3.16. Ring parameters are computed from maximum piston velocity, orifice diameter and free–stream crossflow velocity. Note that for $L/D = 0.64$, 1.27 and 1.84, multiple trajectories are observed while for $L/D = 3.18$ and 4.42, single trajectories are observed. These conditions are plotted on the regime map in figure 4.16(b). The experimentally observed behavior is consistent with our simulations of fully modulated jets in crossflow. When the pulsing produces single vortex rings without any trailing column, multiple trajectories are observed as shown in figure 4.5(g) and 4.6(g). As observed in their experiments, the multiple trajectory jets penetrate deeper into the crossflow.

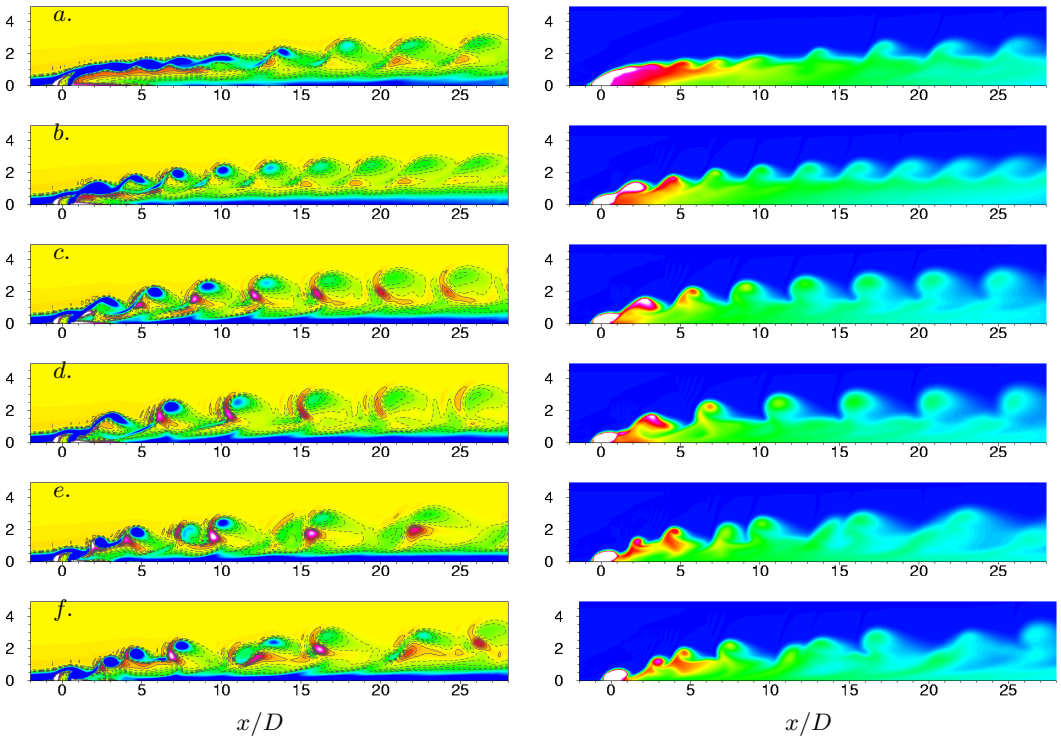

Figure 4.17: Ring velocity ratio = 0.75, duty cycle = 75%: contours of vorticity and scalar are plotted in the symmetry plane at different stroke ratios: (a) 1.0, (b) 2.0, (c) 2.5, (d) 3.0, (e) 4.0 and (f) 6.0. (The length scales on the vertical axes are all y/D.)

4.5 Simulation results for $r_{\mathbf{ring}} < 2$

The behavior of pulsed transverse jets at low velocity ratios is fundamentally different from that at high velocity ratios. This difference may be traced back to the behavior of vortex rings in crossflow at low velocity ratios. As discussed by Sau & Mahesh (2008) and summarized in section 3.5, at low velocity ratios (less than 2), pulsing into a crossflow produces hairpin vortices and not vortex rings. The hairpin vortices form on a certain timescale; if the pulse duration is longer than this timescale, a series of hairpins are shed in a periodic manner. Even a continuous, low velocity ratio jet sheds hairpins. This shedding frequency depends on velocity ratio and Reynolds number. Most of the entrainment of crossflow fluid is due to the hairpin legs.

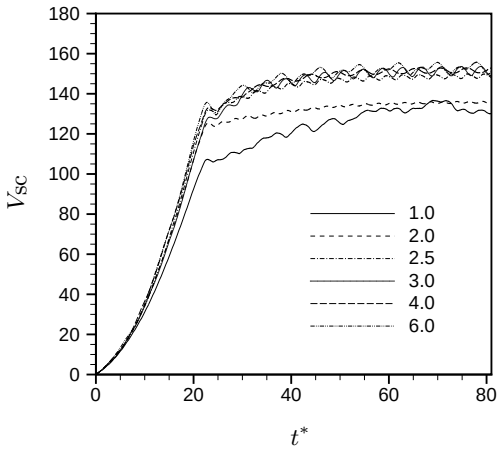

Figure 4.18: Variation of total volume of scalar carrying fluid in the domain with time. The ring velocity ratio is 0.75, duty cycle is 75% and different stroke ratios are considered.

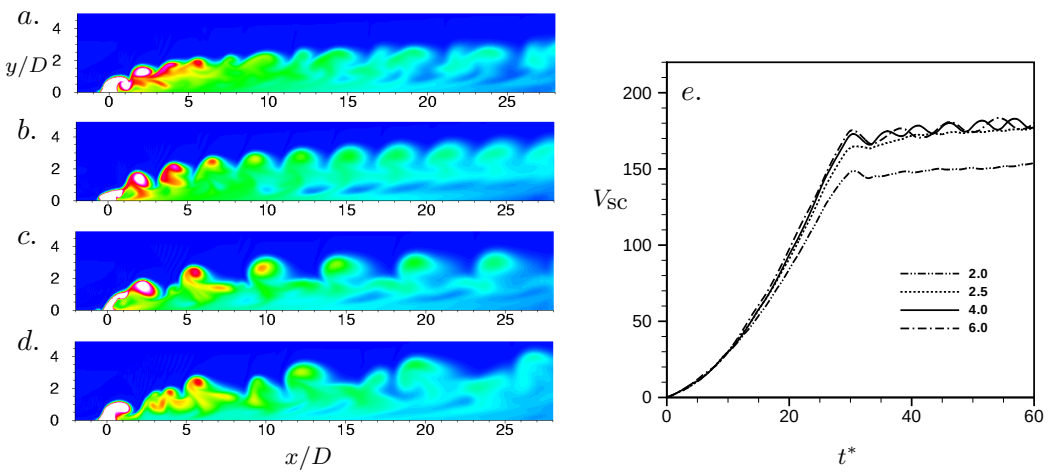

Figure 4.19: Ring velocity ratio = 1.0, duty cycle = 75%. Contours of scalar in the symmetry plane at different stroke ratios: (a) 2.0, (b) 2.5, (c) 4.0 and (d) 6.0. (e) Variation of total volume of scalar carrying fluid in the domain with time. Ring velocity ratio is 1.0, duty cycle is 75% and different stroke ratios are considered.

Here, simulations of continuously pulsed low velocity jets in crossflow are performed. Optimal pulse frequencies are examined at different velocity ratios. Note that for a fixed velocity ratio and duty cycle, varying the frequency changes the length of the pulse (stroke ratio). As discussed above, as long as the pulse length is longer than the timescale on which the hairpins are shed, hairpin structures will form and shed periodically regardless of the pulse Strouhal number St or stroke ratio L/D. It is therefore expected that penetration of the pulsed jet will not change when the pulsing frequency is varied. The simulation results confirm this behavior. Figure 4.17 shows results for a velocity ratio of 0.75 with constant duty cycle of 75% at different St or L/D. Instantaneous scalar contours are plotted in the symmetry plane, and show the cross sections of the hairpin heads. The mean mass flow rate and scalar injection rate through the nozzle exit are held constant while the frequency is varied. The total volume of scalar carrying fluid after initial transients exit the domain(V_{sc}) is computed as a metric for mixing. Figure 4.18 shows how the total volume of scalar carrying fluid (V_{sc}) in the domain varies with time for various stroke ratios at velocity ratio of 0.75 and duty cycle of 75%. The initial transients exit the domain around $t^* = 35$. For each L/D, V_{sc} remains constant after the flow has exited the domain. This constant value of V_{sc} is compared between different L/D. Note that V_{sc} increases with stroke ratio till $L/D = 2.5$, then remains approximately constant as stroke ratio increases. This behavior can be explained as follows.

4.5.1 Timescale of hairpin formation

As mentioned above, there is a natural timescale on which hairpins form at each velocity ratio and Reynolds number. For lower stroke ratios such as $L/D = 1$ or 2, the pulse width is smaller than the natural timescale of hairpin formation. As a result (figure 4.17a–b), the hairpins are much smaller and weaker. The legs of these hairpins do not entrain as much fluid compared to the stronger hairpins produced

at higher L/D (e.g. $L/D = 3$ shown in figure 4.17(d). As L/D increases beyond 3 (4.17e–f), each pulse creates more than one hairpin, which is then shed downstream. These hairpins are created on their natural timescale. In this case, the timescale of hairpin formation is approximately 2.5 (non–dimensionalized using U_p and D). This explains why V_{sc} increases till $L/D = 3$ and then remains constant. As long as the time scale of each pulse is larger than the required natural timescale for hairpin formation, more mixing will be observed. Again at these very low velocity ratios, duty cycle does not play much of a role if the velocity ratio is held constant. This is because the hairpins formed by each pulse are quickly swept away by the crossflow before they can interact with the subsequent hairpins. This is why the higher duty cycle is chosen to compare different stroke ratios. For very low duty cycles; e.g. 15%, the interaction will be even less. It is found that the duty cycle does not have as large an impact at low velocity ratios as it does at high velocity ratios.

Similar results are observed for other low velocity ratios. Figure 4.19 shows scalar contours in the symmetry plane for velocity ratio of 1.0 at different stroke ratios. The duty cycle is kept constant at 75%. Figure 4.19(e) shows the variation of total volume of scalar carrying fluid (V_{sc}) for different stroke ratios. Again, note that the smaller stroke ratio ($L/D = 2.0$) in fig. 4.19(a) results in weaker and smaller hairpins. Larger stroke ratios such as $L/D = 4.0, 6.0$ (fig.4.19c–d) yield stronger hairpins. The natural timescale at $r_{\text{ring}} = 1.0$ is approximately 3.0. The variation of V_{sc} in figure 4.19(e) is consistent with this physical behavior.

4.6 Summary

Controlled simulations of fully modulated, laminar, pulsed jets in crossflow with square–wave excitation are performed. Optimal pulsing conditions for maximum jet penetration and spread into the crossflow are examined. The evolution of pulsed jets in crossflow is interpreted in terms of the behavior of single vortex rings in the

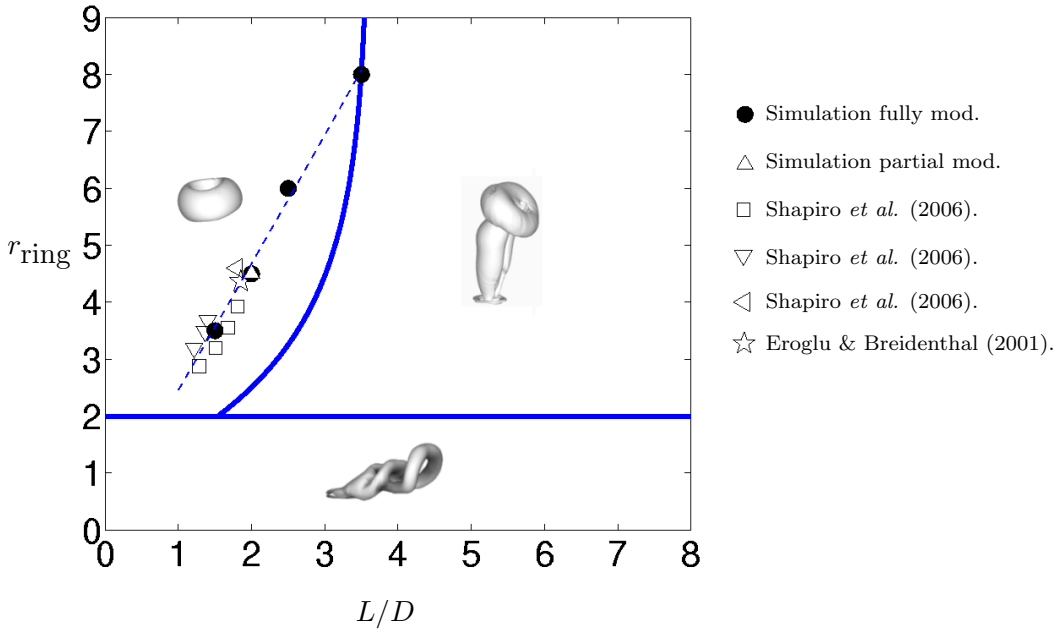

Figure 4.20: Optimal pulsing conditions from several experiments are plotted along with the optimal data from simulations. Note that the data collapse onto a curve.

presence of crossflow. The regime map for single vortex rings in crossflow shows that three different flow regimes exist, depending on the stroke ratio and ring velocity ratio. The pulse conditions (frequency, duty cycle) can be transformed into the ring parameters and the flow field can be interpreted using the regime map. Optimal pulsing conditions from all the simulations fall on a curve in the regime map. Also, data from a wide range of experiments (Shapiro *et al.* 2006, Eroglu & Breidenthal 2001) are interpreted in terms of their vortex rings and optimal experimental conditions are seen to collapse on the same optimal curve in the regime map (figure 4.20).

The behavior at high (greater than 2) and low (less than 2) velocity ratios is fundamentally different. For very high velocity ratios, the rings produced by successive pulses do not interact, and their behavior is similar to that of single rings in crossflow. The optimal stroke ratio under these conditions marks the transition between a vortex ring and vortex ring with trailing column at a given ring velocity

ratio (Sau & Mahesh 2008). The optimal stroke ratio for pulsed jets decreases as the ring velocity ratio decreases. However, as the ring velocity ratio decreases, successive rings begin to interact with each other and the overall penetration decreases. This interaction has the effect of shifting the optimal stroke ratio to the left of the transition curve. The jet apparently splits in two streams for stroke ratios which produces upstream–tilted vortex rings without trailing column. This behavior is observed at stroke ratios around the optimal conditions. The effect of duty cycle is examined. For very high values of duty cycle, the rings interact in the very near field irrespective of the stroke ratio and no optimum is found. As long as the duty cycle is low, an optimal penetration is obtained and this optimal stroke ratio does not change when duty cycle changes.

At very low ring velocity ratios, hairpin structures form, and are shed periodically. These hairpin structures form on a timescale that depends on velocity ratio and Reynolds number. Pulsed jet simulations at these low ring velocity ratios suggest that for optimal mixing, the timescale associated with each pulse should at least equal or be greater than the natural timescale of hairpin formation. Hence at very low velocity ratios, large stroke ratios yield most effective mixing. At very low velocity ratios, duty cycle does not affect the flow very much if the velocity ratio is held constant. Regardless of the duty cycle, the hairpins formed by each pulse are swept away by the crossflow before they can interact with each other.

The main contribution of this study is to show how optimal pulsing conditions (at least for square wave pulsing) for jets in crossflow can be predicted in terms of the vortex rings produced by the pulsing. The regime map allows experimental control parameters such as stroke length, frequency, duty cycle, kinetic energy of fluctuations etc. to be predicted by relating them to the ring stroke ratio and velocity ratio. The collapse of data from a number of experiments and simulations is encouraging in light of the wide scatter that optimal Strouhal numbers are known to display (Narayanan *et al.* 2003). Also, the effect of the crossflow is consistently

accounted for in this study, and not ignored (e.g. Johari 2006). The proposed idea is valid for both full and partial modulation, since ring parameters are based on the deviation of the velocity about the mean. Also, the regime map appears to be relatively robust, as demonstrated by the agreement between an ideal square waveform and a non–ideal experimental waveform. The regime map is therefore proposed as a promising approach to predict optimal conditions for pulsed jets in crossflow.

Bibliography

[1] Acarlar, M. S. & Smith, C. R. 1987 A study of hairpin vortices in a laminar boundary layer. Part 1. Hairpin vortices generated by a hemisphere protuberance. *J. Fluid Mech.* **175**, 1–41.

[2] Acarlar, M. S. & Smith, C. R. 1987 A study of hairpin vortices in a laminar boundary layer. Part 2. Hairpin vortices generated by fluid injection. *J. Fluid Mech.* **175**, 43–83.

[3] Bardina, J., Ferziger, J. H. & Reynolds, W.C. 1980 Improved subgrid scale models for large eddy simulation, *AIAA paper* 80-1357.

[4] Blossey, P., Narayanan, S. & Bewley, T.R. 2001 Dynamics and control of a jet in crossflow: direct numerical simulation and experiments. *Proc. IUTAM Symp. Turbulent Mixing Combustion*, ed. A. Pollard & S. Candel, Kluwer Academic, Dordrecht, pp. 45–56.

[5] Burton, G. C. & Dahm, W. J. A. 2005 Multifractal subgrid-scale modeling for large-eddy simulation. I. Model development and a priori testing, *Phys. Fluids* 17, 075111

[6] Chang, Y. K. & Vakili, A. D. 1995 Dynamics of vortex rings in crossflow. *Physics of Fluids* **7**, 1583–1597.

[7] Comte-Bellot, G. & Corrsin, S. 1971 Simple Eulerian time correlation of full and narrow–band velocity signals in grid-generated, 'isotropic' turbulence, *J. Fluid Mech.* 48, p. 273.

[8] Dabiri, J.O. & Gharib, M. 2004 Fluid entrainment by isolated vortex rings. *J. Fluid Mech.* **511**, 311–331.

[9] Didden, N. 1979 On the formation of vortex rings: Rolling–up and production of circulation. *Z. Angew. Mech. Phys.* **30**, 101–116.

[10] Domaradzki, J. A. & Loh, K.C. 1999 The subgrid-scale estimation model in the physical space representation, *Phys. Fluids* 11, 2330.

[11] Domaradzki, J. A., Loh, K. C. & Yee, P. P. 2002 Large eddy simulations using the subgrid-scale estimation model and truncated Navier–Stokes dynamics, *Theor. Comput. Fluid Dyn.* 15, 421.

[12] Eroglu, A. & Briedenthal, R. E. 2001 Structure, penetration and mixing of pulsed jets in crossflow. *AIAA J.* **39**, 417–423.

[13] Fric, T. F. & Roshko, A. 1994 Vortical structure in the wake of a transverse jet. *J. Fluid Mech.* **279**, 1–47.

[14] Germano, M., Piomelli, U., Moin, P. & Cabot, W. H. 1991 A dynamic subgridscale eddy viscosity model, *Phys. Fluids* 3, 1760.

[15] Gharib, M., Rambod, E. & Shariff, K. 1998 A universal time scale for vortex ring formation. *J. Fluid Mech.* **360**, 121–140.

[16] Ghosal, S., Lund, T. S., Moin, P. & Akselvoll, K. 1995 A dynamic localization model for large-eddy simulation of turbulent flows, *J. Fluid Mech.* 286, p. 229-255.

[17] Glezer, A. 1988 The formation of vortex rings. *Phys. Fluids* **31**, 3532–3542.

[18] Gopalan, S., Abraham, B. M. & Katz, J. 2004 The structure of a jet in cross flow at low velocity ratios. *Physics of Fluids* **16(6)**, 2067–2087.

[19] Hermanson, J. C., Wahba, A. & Johari, H. 1998 Duty cycle effects on penetration of fully modulated, turbulent jets in crossflow. *AIAA J.* **36**, 1935–1937.

[20] Johari, H. 2006 Scaling of fully pulsed jets in crossflow. *AIAA J.* **44**, 2719–2725.

[21] Johari, H., Pacheco-Tougas, M. & Hermanson, J. C. 1999 Penetration and mixing of fully modulated jets in crossflow. *AIAA J.* **37**, 842–850.

[22] Karagozian, A. R., Cortelezi, L. & Soldati, A. 2003 Manipulation and control of jets in crossflow. In *CISM Courses and Lectures No. 439*, , vol. 218. Springer Wien.

[23] Kemenov, K. A. & Menon, S. 2006 Explicit small-scale velocity simulation for high-Re turbulent flows, *J. Comput. Phys.* 220, 290.

[24] Kim, W. W. & Menon, S. 1995 A new dynamic one-equation subgrid-scale model for large eddy simulations, *AIAA Paper* 95-0356.

[25] Lesieur, M. & Metais, O. 1996 New Trends in Large-Eddy Simulations of Turbulence, *Annual Review of Fluid Mechanics*, Vol. 28: 45-82.

[26] Liepmann, D. & Gharib, M. 1992 The role of streamwise vorticity in the near-field entrainment of round jets. *J. Fluid Mech.* **245** 643-668.

[27] Lilly, D. 1992 A proposed modification of the Germano subgrid–scale closure method, *Phys. Fluids A* 4, 633.

[28] Liu, S., Meneveau, C., Katz J. 1994 On the properties of similarity subgrid-scale models as deduced from measurements in a turbulent jet. *J. Fluid Mech.* 275, 83.

[29] Mahesh, K., Constantinescu, G. & Moin, P. 2004 A numerical method for large–eddy simulation in complex geometries. *J. Comput. Phys.* **197**, 215–240.

[30] Maragason, R. J. 2002 Fifty years of jet in crossflow research. In *AGARD Symp. on a Jet in Crossflow, Winchester, UK, AGARD CP*-534.

[31] Marshall, J. S. & Grant, J. R. 1994 Evolution and break–up of vortex rings in straining and shearing flows. *J. Fluid Mech.* **273**, 285–312.

[32] Maxworthy, T. 1972 The structure and stability of vortex rings. *J. Fluid Mech.* **51**, 15–32.

[33] Maxworthy, T. 1977 Some experimental studies of vortex rings. *J. Fluid Mech.* **81**, 465–495.

[34] Megerian, S., Davitian, J., Alves, L. S. De B. & Karagozian, A. R. 2007 Transverse-jet shear-layer instabilities. Part 1. Experimental studies. *J. Fluid Mech.* **593**, 93–129.

[35] Meneveau, C. & Katz, J. 2000 Scale-invariance and turbulence models for large-eddy simulation, *Annu. Rev. Fluid Mech.* 32.

[36] Meneveau, C., Lund, T. S. & Cabot, W. H. 1996 A Lagrangian dynamic subgrid-scale model of turbulence, *J. Fluid Mech.* 319, 353.

[37] Misra, A. & Pullin, D. 1997 A vortex-based subgrid stress model for large-eddy simulation, *Phys. Fluids* 9(8), 2443.

[38] Moin, P., Squires, K., Cabot, W. & Lee, S. 1996 A dynamic subgridscale model for compressible turbulence and scalar transport, *Phys. Fluids* 3, 2746

[39] Morinishi, Y. & Vasilyev, O. V. 2002 Vector level identity for dynamic subgrid scale modeling in large eddy simulation, *Phys. Fluids* 14, 3616.

[40] Muppidi, S. 2006 Direct Numerical Simulations and Modeling of jets in crossflow. *PhD Thesis,* University of Minnesota

[41] Muppidi, S. & Mahesh, K. 2008 Direct Numerical Simulation of passive scalar transport in transverse jets. *J. Fluid Mech.* **598**, 335–360.

[42] M'Closkey, R. T., King, J. M., Cortelezzi, L. & Karagozian, A. R. 2002 The actively controlled jet in crossflow. *J. Fluid Mech.* **452**, 325–335.

[43] Müller, E. A. & Didden, N. 1980 Zur erzeugung der zirkulation bei der bildung eines ringwirbels an einer dusenmundung. *Stroj. Casop.* **31**, 363–372.

[44] Narayanan, S., Barooah, P. & Cohen, J. M. 2003 Dynamics and control of an isolated jet in crossflow. *AIAA J.* **14**, 2316–2330.

[45] Park, N. & Mahesh, K. 2007 Analysis of numerical errors in large eddy simulation using statistical closure theory, *J. Comput. Phys.* 222, 1.

[46] Park, N. & Mahesh, K. 2008 A velocity-estimation subgrid model constrained by subgrid scale dissipation, *J. Comput. Phys.* 227, 8.

[47] Park, N. & Mahesh, K. 2009 Reduction of the Germano-identity error in the dynamic Smagorinsky model, *Phys. Fluids* 21, 065106.

[48] Rosenfeld, M., Rambod, E. & Gharib, M. 1998 Circulation and formation number of laminar vortex rings. *J. Fluid Mech.* **376**, 297–318.

[49] Sau, R. & Mahesh, K. 2007 Passive scalar mixing in vortex rings. *J. Fluid Mech.* **582**, 449–491.

[50] Sau, R. & Mahesh, K. 2008 Dynamics and mixing of vortex rings in crossflow. *J. Fluid Mech.* **604**, 389–409.

[51] Sau, R. & Mahesh, K. 2010 Optimization of pulsed jets in crossflow. *J. Fluid Mech.* **653**, 365–390.

[52] Schumann 1975 Subgrid scale model for finite difference simulations of turbulent flows in plane channels and annuli, *J. Comput. Phys.* 18.

[53] Scotti, A. & Meneveau, C. 1999 A fractal model for large eddy simulation of turbulent flow. *Physica D.* 127:198.

[54] Shapiro, S. R., King, J. M., Karagozian, A. R. & M'Closkey, R. T. 2003 Optimization of controlled jets in crossflow. *AIAA Paper* pp. 2003–634.

[55] Shapiro, S. R., King, J. M., Karagozian, A. R. & M'Closkey, R. T. 2006 Optimization of controlled jets in crossflow. *AIAA J.* **44**, 1292–1298.

[56] Shariff, K. & Leonard, A. 1992 Vortex rings. *Annu. Rev. Fluid Mech.* **24**, 235–279.

[57] Smagorinsky, J. 1963 General circulation experiments with the primitive equations: I. The basic experiment, *Mon. Weather Rev.* 91, 99.

[58] Stolz, S., Adams, N. A. & Kleiser, L. 2001 An approximate deconvolution model for large-eddy simulation with application to incompressible wall-bounded flows, *Phys. Fluids* 13, 997.

[59] Ting, L. & Tung, C. 1965 Motion and Decay of a Vortex in a Nonuniform Stream. *Physics of Fluids* **8(6)**, 1039–1051.

[60] Tomar, S., Arnaud, J. & Soria, J. 2004 Structure, penetration of a zero–net–mass–flux round jet in crossflow. *Tech. Rep.*. Proceedings of 15th Australasian Fluid Mechanics Conference.

[61] Vermeulen, P. J., Rainville, P. & Ramesh, V. 1992 Measurements of the Entrainment Coefficient of Acoustically Pulsed Axisymmetric Free Air Jets. *Journal of Engineering for Gas Turbines and Power*. **114(2)**, 409-415.

[62] Vermeulen, P. J., Ramesh, V. & Yu, W. K. 1986 Measurements of Entrainment by Acoustically Pulsed Axisymmetric Air Jets. *Journal of Engineering for Gas Turbines and Power*. **108(3)**, 479-484.

[63] Wu, J. M., Vakili, A. D. & Yu, F. M. 1988 Investigation of the interacting flow of non-symmetric jets in crossflow. *AIAA J.* **26**, 940–947.

[64] Yoshizawa, A. 1986 Statistical theory for compressible turbulent shear flows, with the application to subgrid modeling, *Phys. Fluids* 29, 2152

Appendix A

Subgrid scale estimation models for Large Eddy Simulation

A.1 Motivation & previous work

We develop subgrid scale models for Large Eddy Simulation (LES) to predict scalar mixing in very high Reynolds number turbulent flows.

LES is a numerical technique to compute high Reynolds number turbulent flows. In LES, the large scale motions (resolved scales) are directly computed while the small scales are discarded. The effect of small scales is modeled through the subgrid stress $\tau_{ij} = \overline{u_i u_j} - \overline{u}_i \overline{u}_j$. Traditional SGS models can be classified as eddy–viscosity models, similarity models and mixed models. There are extensive reviews of the traditional SGS modeling in the literature, e.g. Meneveau & Katz (2000), Lesieur & Metais (1996). The eddy–viscosity models, $\tau_{ij} - \tau_{kk}\delta_{ij} = 2\nu_T \overline{S}_{ij}$ are most commonly used because of their simplicity and robustness. Here ν_T is the eddy viscosity, $\overline{S}_{ij}$ is resolved strain rate and δ_{ij} is the Kronecker delta function. In the original Smagorinsky model, the eddy viscosity is expressed as $\nu_T = C_s \overline{\Delta}^2 \left(2\overline{S}_{ij}\overline{S}_{ij}\right)^{\frac{1}{2}}$, where C_s is an empirical model constant (Smagorinsky 1963). The most popular model among eddy–viscosity models is the dynamic Smagorinsky model (DSM) (Germano

et al. 1991) where the model coefficient is obtained dynamically. The dynamic approach is based on the Germano identity:

$$T_{ij} - \{\tau_{ij}\} = L_{ij} \tag{A.1}$$

where $(\{\})$ is the test filter, T_{ij} is the subtest scale stress at the test filter level, $T_{ij} = \{\overline{u_i u_j}\} - \{\overline{u}_i\}\{\overline{u}_j\}$ and $L_{ij} = \{\overline{u}_i\overline{u}_j\} - \{\overline{u}_i\}\{\overline{u}_j\}$ is the resolved stress. The model constant is obtained by minimizing the Germano identity error, ϵ_{ij}:

$$\epsilon_{ij} = T_{ij}^M - \left\{\tau_{ij}^M\right\} - L_{ij} \tag{A.2}$$

where T_{ij}^M is obtained using scale similarity:
$T_{ij}^M - T_{kk}^M\delta_{ij} = 2C_s\left\{\overline{\Delta}\right\}^2\left(2\left\{\overline{S}\right\}_{ij}\left\{\overline{S}\right\}_{ij}\right)^{\frac{1}{2}}\left\{\overline{S}\right\}_{ij}$. $\left\{\overline{\Delta}\right\}$ is the test filter width. However, minimizing (A.2) requires obtaining the scalar unknown C_s from the tensor equation (A.2). Originally, Germano *et al.* (1991) computed C_s by satisfying $\epsilon_{ij}\overline{S}_{ij} = 0$. Subsequently, Lilly (1992) proposed the most widely used modification where C_s is computed by minimizing $\epsilon_{ij}\epsilon_{ij}$ in the least square sense:

$$(C_s\overline{\Delta})^2 = \frac{\langle L_{ij}M_{ij}\rangle_{h+}}{\langle M_{ij}M_{ij}\rangle_h} \tag{A.3}$$

where $M_{ij} = 2(\left\{\overline{\Delta}\right\}/\overline{\Delta})^2\left\{\overline{|S|}\right\}\left\{\overline{S}\right\}_{ij} - 2\left\{|\overline{S}|\overline{S}_{ij}\right\}$, $<>_h$ is an average over homogeneous directions, and $\langle\phi\rangle_+ = 0.5(\phi+|\phi|)$ denotes clipping for positive eddy viscosity. There are other variants of the minimizing procedure of the Germano identity error. Meneveau *et al.* (1996) proposed an Lagrangian version of the DSM to minimize the time averaged Germano identity error. Morinishi and Vasilyev (2002) applied the dynamic procedure on SGS force rather than on SGS stress and proposed a model based on vector level identity. Recently, Park and Mahesh (2009) considered the ensemble averaged Germano identity error and proposed a correction that further reduces the error. Eddy–viscosity models are purely dissipative and therefore stabi-

lizing. However, these models have drawbacks such as very poor correlation with the real subgrid stress tensor and an inability to predict the backscatter of energy. In scale similarity models, the effect of small scales is modeled in terms of the interaction between large and small resolved scales; e.g. $\tau_{ij} = C_L \left(\widetilde{\overline{u}_i \overline{u}_j} - \widetilde{\overline{u}}_j \widetilde{\overline{u}}_j \right)$, where C_L is model coefficient (Bardina *et al.* 1980 and Liu *et al.* 1994). These models show better correlation with actual SGS stress tensor in a priori tests but lack dissipation of energy in actual LES. To ensure dissipation, mixed models are proposed where an eddy–viscosity term is added to the scale similarity model.

Subgrid velocity estimation is an alternative approach to eddy–viscosity and scale similarity models. Here, the subgrid stress is computed directly from the estimated subgrid velocity (Domaradzki & Loh 1990, Scotti & Meneveau 1999, Domaradzki *et al.* 2002, Burton & Dahm 2005, Kemenov & Menon 2006, Park & Mahesh 2008). The subgrid velocity estimation models are free from linear stress–strain relationship and do not use the equivalence of energy transfer and dissipation. Estimation models also have backward dissipation which is present in actual turbulent flows. One fundamental issue is to represent the subgrid velocity on the LES grid. Kemenov & Menon (2006) use a fully resolved, but reduced one dimensional model to obtain the subgrid velocity. Domaradzki *et al.* (2002) use a three dimensional finer but under–resolved grid to obtain $u_i^{'}$. Misra and Pullin (1997) assume the subgrid structure consists of stretched vortices and obtain the SGS stress from the distribution of stretched vortices and from the subgrid kinetic energy, together with an assumed Kolmogorov energy spectrum for the subgrid scales. Other estimation models proposed are based on subgrid vorticity estimation and one–dimensional fractal interpolation (Scotti & Meneveau 1999, Burton & Dahm 2005).

Park & Mahesh (2008) proposed a simple velocity estimation model which is constrained by subgrid dissipation. Their estimation model incorporates the dissipative nature of the eddy–viscosity models into more physically appealing non–eddy viscosity SGS models by constraining the ensemble average of the resulting SGS dis-

sipation. The main idea is to use the SGS dissipation of the eddy–viscosity model to constrain the coefficients of the non–eddy viscosity model. This type of subgrid modeling does not require finer grids and does not have any adjustable coefficients. The model works very well for decaying isotropic turbulence and channel flows. However, the previous model had some theoretical drawbacks in that the predicted subgrid kinetic energy levels were small and in how Galilean invariance was imposed.

A.2 Velocity estimation model

The filtered Navier–stokes equations are

$$\frac{\partial \bar{u}_i}{\partial t} + \frac{\partial \bar{u}_i \bar{u}_j}{\partial x_j} = -\frac{\partial \bar{p}}{\partial x_i} + \nu \frac{\partial^2 \bar{u}_i}{\partial x_j x_j} - \frac{\partial \tau_{ij}}{\partial x_j} \quad , \quad \frac{\partial \bar{u}_i}{\partial x_i} = 0 \tag{A.4}$$

where τ_{ij} is the subgrid stress. The subgrid stress is expressed in terms of the resolved velocity, $\overline{u}_i$ and subgrid velocity, $u_i^{'}$ as

$$\tau_{ij} = \overline{u_i u_j} - \overline{u}_i \overline{u}_j \tag{A.5}$$

$$= \overline{\overline{u}_i \overline{u}_j} + \overline{\overline{u}_i u_j^{'}} + \overline{u_i^{'} \overline{u}_j} + \overline{u_i^{'} u_j^{'}} - \overline{u}_i \overline{u}_j. \tag{A.6}$$

The central idea is to estimate or model the subgrid velocity, and obtain the subgrid stress from the estimated subgrid velocity.

A.2.1 Park & Mahesh (2008) model

Recently, Park & Mahesh (2008) proposed a velocity estimation approach which is constrained by subgrid dissipation. The SGS stress, τ_{ij} for sharp cut–off filter is $\overline{\overline{u}_i u_j^{'}} + \overline{u_i^{'} \overline{u}_j} + \overline{u_i^{'} u_j^{'}}$. τ_{ij} is grid–scale quantity and therefore can be expressed as a function of the resolved velocity $\overline{u}_i$. They note that τ_{ij} is represented on the LES grid though SGS information ($u_i^{'}$) is required. This motivated them to model the

SGS stress as

$$\tau_{ij}^{M} = \overline{u}_i u_j^{\mathrm{rsg}} + u_i^{\mathrm{rsg}} \overline{u}_j + u_i^{\mathrm{rsg}} u_j^{\mathrm{rsg}} \tag{A.7}$$

where u_i^{rsg} is the 'resolved projection' of SGS velocity. u_i^{rsg} is modeled as

$$u_i^{\mathrm{rsg}} = R\theta \overline{u}_j L_{ij} \tag{A.8}$$

where R is a dimensionless constant, θ is a time scale and L_{ij} is a linear term. The model is termed as *resolved–subgrid estimation model* (RSEM). They consider two candidates for L_{ij}, $L_{ij}^{(1)} = \overline{D}_{ij}$ and $L_{ij}^{(2)} = \overline{S}_{ij}$. Here $\overline{D}_{ij}$ and $\overline{S}_{ij}$ are the deformation and strain–rate tensors respectively. The model corresponding to the two forms are referred as RSEM-S and RSEM-D. It is found from numerical experiments that RSEM-S outperforms RSEM-D.

The coefficient R is determined by forcing the modeled SGS dissipation to approximate a target value of the dissipation in the mean sense. The 'target dissipation', D^T is obtained from the dynamic Smagorinsky model (Germano *et al.* 1991):

$$D^T = \tau_{ij}^T \overline{S}_{ij} \text{ and } \tau_{ij}^T - \frac{1}{3}\tau_{kk}^T \delta_{ij} = -2C_s \overline{\Delta}^2 |\overline{S}| \overline{S}_{ij} \tag{A.9}$$

where C_s is obtained using the dynamic procedure. The estimation model is constrained by the ensemble average of D^T; i.e

$$\left\langle \tau_{ij}^M \overline{S}_{ij} \right\rangle = \left\langle D^T \right\rangle \tag{A.10}$$

where $\langle\rangle$ denotes the ensemble average. By substituting equations (A.7) and (A.8) in the above equation, and assuming R is constant with respect to the ensemble average, one obtains

$$\langle \alpha \rangle R^2 + \langle \beta \rangle R = \left\langle D^T \right\rangle \tag{A.11}$$

where $\alpha = \theta^2 \overline{u}_m L_{im} \overline{u}_n L_{jn} \overline{S}_{ij}$ and $\beta = \theta \left(\overline{u}_i \overline{u}_k L_{jk} + \overline{u}_j \overline{u}_k L_{ik} \right) \overline{S}_{ij}$. The coefficient R

is chosen such that it minimizes difference between the mean dissipation obtained from RSEM and the mean target dissipation. So, R is obtained by minimizing the least-square error

$$E(R) = \int_{\Omega} \left(\alpha R^2 + \beta R - D^T\right)^2 d\mathbf{x}. \tag{A.12}$$

Once R is obtained, τ_{ij}^M is constructed from u_i^{rsg} using equation (A.8). The model is applied to decaying isotropic turbulence and channel flow. The model yields as good results as the dynamic Smagorinsky model (DSM) for isotropic turbulence. It predicts better statistics and instantaneous flow structures in channel flow than DSM. However, the model formulation in equation (A.8) violates the Galilean invariance by itself. The bulk velocity of the entire flow is used to enforce the Galilean invariance of the modeled stress. The expression involving the resolved velocity $\overline{u}_i$ in equation (A.8) is replaced by $\overline{u}_i - U_i$ where U_i is the bulk velocity. Also, the subgrid kinetic energy provided by this model is very small. The model proposed in this paper resolves these issues.

A.2.2 Proposed model

The true subgrid scale stress is

$$\tau_{ij} = \overline{\overline{u}_i\overline{u}_j} + \overline{\overline{u}_i u_j^{'}} + \overline{u_i^{'}\overline{u}_j} + \overline{u_i^{'}u_j^{'}} - \overline{u}_i\overline{u}_j. \tag{A.13}$$

The unresolved velocity is modeled as a vector function of the resolved quantities:

$$u_i^{'} = F_i(\overline{u}_j, \overline{S}_{ij}) \tag{A.14}$$

where, $\overline{S}_{ij}$ is strain–rate tensor. We can obtain an expression for $u_i^{'}$ by expanding the polynomial F_i. Using tensor algebra, a vector valued function $F_i(\overline{u}_j, \overline{S}_{ij})$ of a

second order symmetric tensor $\overline{S}_{ij}$ and a vector $\overline{u}_i$, can be expanded as follows:

$$F_i(\overline{u}_j, \overline{S}_{ij}) = C_0\overline{u}_i + C_1\overline{S}_{ik}\overline{u}_k + C_2\overline{S}_{ik}\overline{S}_{kl}\overline{u}_l \tag{A.15}$$

where the coefficients C_0, C_1 and C_2 are functions of invariants.
$C_i = C_i(I_S, II_S, III_S, I_u, I_{S,u}, II_{S,u})$. Here, $I_S = \text{trace}(\overline{S}_{ij})$, $II_S = \text{trace}(\overline{S}^2_{ij})$ and $III_S = \text{trace}(\overline{S}^3_{ij})$ are three independent invariants of $\overline{S}_{ij}$; $I_u = \overline{u}_i\overline{u}_i$ is the invariant of $\overline{u}_i$; and $I_{S,u} = \overline{u}_i\overline{S}_{ij}\overline{u}_j$ and $II_{S,u} = \overline{u}_i\overline{S}_{ik}\overline{S}_{kj}\overline{u}_j$ are invariants for $\overline{S}_{ij}$ and $\overline{u}_i$. Note that the above expression, Eq. (A.15) for $F_i(\overline{u}_j, \overline{S}_{ij})$ is exact and the function, F_i is quadratic in $\overline{S}_{ij}$ with three unknown coefficients. All the higher order terms are reduced to quadratic forms using the symmetric property of $\overline{S}_{ij}$ and Cayley–Hamilton theorem. Using equations (A.14) & (A.15), the model for $u_i^{'}$ reads as,

$$u_i^{'} = C_0\overline{u}_i + C_1\theta\overline{S}_{ik}\overline{u}_k + C_2\theta^2\overline{S}_{ik}\overline{S}_{kl}\overline{u}_l \tag{A.16}$$

where θ is a time scale which is set to Δ/U_{ref} where U_{ref} is the reference velocity. θ makes the coefficients dimensionless. Equation (A.16) shows that the new SGS velocity estimation model with three unknown coefficients. Note that if C_0 and C_2 are set to zero then the model reduces to the RSEM–S model (Park & Mahesh 2008) with only one coefficient as in Eq. (A.8). Similar to RSEM-D, the alternative approach is to model $u_i^{'}$ using the resolved velocity gradient tensor, $\overline{D}_{ij}$ instead of $\overline{S}_{ij}$:

$$u_i^{'} = F_i(\overline{u}_j, \overline{D}_{ij}). \tag{A.17}$$

The polynomial expansion reads as

$$\begin{aligned} u_i^{'} = F_i(\overline{u}_j, \overline{D}_{ij}) =& C_0\overline{u}_i + C_1\theta\overline{D}_{ik}\overline{u}_k + C_2\theta\overline{D}^T_{ik}\overline{u}_k + C_3\theta^2\overline{D}_{ik}\overline{D}_{kl}\overline{u}_l + \\ & C_4\theta^2\overline{D}_{ik}\overline{D}^T_{kl}\overline{u}_l + C_5\theta^2\overline{D}^T_{ik}\overline{D}_{kl}\overline{u}_l + ... \end{aligned} \tag{A.18}$$

It is readily evident that equation (A.18) (*D–formulation*) yields lot more unknown coefficients than the equation (A.16) (*S–formulation*). The D–formulation is not reducible to a finite low order polynomial. Although, we can truncate the higher order terms and use the first three terms (until linear terms) of the polynomial to construct $u_i^{'}$:

$$u_i^{'} = F_i(\overline{u}_j, \overline{D}_{ij}) \approx C_0\overline{u}_i + C_1\theta\overline{D}_{ik}\overline{u}_k + C_2\theta\overline{D}_{ik}^T\overline{u}_k. \tag{A.19}$$

Note that RSEM–D model (Park & Mahesh 2008) has only the second term on the right hand side. It is found from our numerical experiments that the D–formulation yields inferior results than the S–formulation. Thus, the D–formulation is discarded and the S–formulation is considered in this paper.

A.2.3 Coefficient determination

The three coefficients in equation (A.16) are obtained by imposing three external constraints: (i) Galilean invariance, (ii) ensemble averaged subgrid dissipation and (iii) subgrid kinetic energy.

The model should preserve the Galilean invariance of the LES equations. Galilean invariance requires the LES equations to be form invariant under observer transformation, $\mathbf{X}^* = \mathbf{X} + \mathbf{V}t + \mathbf{b}$, where $\mathbf{V}$ and $\mathbf{b}$ are constant vectors. Applying this transformation and invoking the Galilean invariance of the unresolved velocity $\mathbf{u}^{'*} = \mathbf{u}^{'}$ yields,

$$\tau_{ij}^* = \tau_{ij} + V_i\overline{u_j^{'}} + V_j\overline{u_i^{'}}. \tag{A.20}$$

Note that the invariance error is zero, when $\overline{u_i^{'}} = 0$, which is the case for sharp cut–off filter. Galilean invariance of the unresolved velocity ($\mathbf{u}^{'*} = \mathbf{u}^{'}$) implies that

$$C_0\overline{V}_i + C_1\theta\overline{S}_{ik}\overline{V}_k + C_2\theta^2\overline{S}_{ik}\overline{S}_{kl}\overline{V}_l = 0 \text{ for any constant vector } \mathbf{V}. \tag{A.21}$$

This implies that,

$$\det(C_0\mathbf{I} + C_1\theta\overline{\mathbf{S}} + C_2\theta^2\overline{\mathbf{S}}^2) = 0 \text{ or } C_0 + C_1\left(\theta^3\det\overline{S}\right) + C_2\left(\theta^3\det\overline{S}\right)^2 = 0. \quad \text{(A.22)}$$

The Galilean invariance yields a linear relation between the coefficients in Eq. (A.22).

The second constraint imposed on the estimation model is the ensemble averaged subgrid dissipation. The estimation model is constrained to approximate a prescribed subgrid dissipation. This constraint is imposed in the average sense since if applied locally, it will be purely dissipative in nature. Constraining the ensemble average dissipation allows the model to locally provide both forward and backward dissipation. So, the dissipation constraint reads as

$$\left\langle \tau_{ij}\overline{S}_{ij}\right\rangle = \left\langle D^T\right\rangle \quad \text{(A.23)}$$

where τ_{ij} is the modeled stress from the estimated velocity, D^T is the target dissipation and $\langle\rangle$ denotes the ensemble average. D^T is supplied using dynamic Smagorinsky model (Germano *et al.* 1991) or a new dissipation model (discussed later). Substituting equations (A.13) and (A.16) in (A.23) and using tensor manipulations, the dissipation constraint implies,

$$\begin{aligned}\left\langle D^T\right\rangle = &\left\langle \left(C_0^2 + 2C_0\right)\overline{u}^T\overline{S}\overline{u} + \left(C_1 + C_0C_1\right)2\theta\overline{u}^T\overline{S}^2\overline{u} + \left(C_2 + C_0C_2\right)2\theta^2\overline{u}^T\overline{S}^3\overline{u}\right\rangle \\ &+ \left\langle C_1^2\theta^2\overline{u}^T\overline{S}^3\overline{u} + C_2^2\theta^4\overline{u}^T\overline{S}^5\overline{u} + C_1C_2 2\theta^3\overline{u}^T\overline{S}^4\overline{u}\right\rangle.\end{aligned} \quad \text{(A.24)}$$

Note that tensor contractions are written using matrix notation where $\overline{u}^T\overline{S}\overline{u} = \overline{u}_i\overline{S}_{ij}\overline{u}_j$ and $\overline{u}^T\overline{S}^2\overline{u} = \overline{u}_i\overline{S}_{ik}\overline{S}_{kj}\overline{u}_j$. The right hand side of Eq. (A.24) denotes the ensemble average dissipation obtained from the estimation model.

The subgrid scale kinetic energy, k_{sgs} obtained from the estimated velocity is

constrained locally by a prescribed target value, $k_{\rm sgs}^T$:

$$k_{\rm sgs} = \frac{1}{2}\tau_{ii} = \frac{1}{2}\left(C_0^2 + 2C_0\right)\overline{u}^T\overline{u} + \left(C_1 + C_0C_1\right)\theta\overline{u}^T\overline{S}\overline{u} + \left(C_2 + C_0C_2\right)\theta^2\overline{u}^T\overline{S}^2\overline{u} + \frac{1}{2}C_1^2\theta^2\overline{u}^T\overline{S}^2\overline{u} + \frac{1}{2}C_2^2\theta^4\overline{u}^T\overline{S}^4\overline{u} + C_1C_2\theta^3\overline{u}^T\overline{S}^3\overline{u} = k_{\rm sgs}^T. \tag{A.25}$$

The target subgrid kinetic energy is supplied through either dynamic Yoshizawa's model (Yoshizawa 1986, Moin *et al.* 1991) or a transport equation (Kim & Menon 1995) for subgrid kinetic energy.

Thus we obtain a system of three equations (A.22), (A.24) and (A.25) for C_0, C_1 and C_2. Note that equation (A.22) is linear whereas the other two equations are quadratic in C_0, C_1 and C_2. The system of equations is solved as follows. The linear relation in (A.22) is inserted into (A.23) and (A.25) to yield two quadratic equations involving C_1 and C_2:

$$\langle\alpha_1\rangle C_1^2 + \langle\alpha_2\rangle C_1^2 + \langle\alpha_3\rangle C_1C_2 + \langle\alpha_4\rangle C_1 + \langle\alpha_5\rangle C_2 = \left\langle D^T\right\rangle \tag{A.26}$$

$$\beta_1C_1^2 + \beta_2C_2^2 + \beta_3C_1C_2 + \beta_4C_1 + \beta_5C_2 = k_{\rm sgs}^T \tag{A.27}$$

where α_i, β_i ($i = 1$ to 5) can be obtained from the three equations (A.22), (A.24) and (A.25), and are detailed in the appendix. Note that C_1 and C_2 are taken out of the ensemble average operator. C_1 and C_2 are obtained by solving the two quadratic equations locally such that the least square error is minimized. Then, C_0 is obtained from equation (A.22). Note that the Galilean invariance constraint is satisfied exactly. The external targets D^T and $k_{\rm sgs}^T$ can be obtained from models, DNS data or experiments. In this paper, three pairs of different model combinations are considered as shown in table A.1. Once C_0, C_1 and C_2 are obtained, then the estimated velocity u_i' is obtained (Eq. (A.16)) from which the subgrid stress τ_{ij}^M is calculated (Eq. (A.13)).

	D^T	k^T_{sgs}
1	Dynamic Smagorinsky model (Germano *et al.* 1991)	Dynamic Yoshizawa model (Moin *et al.* 1991)
2	Kim & Menon (1995) model	A transport equation for k_{sgs}, Kim & Menon (1995)
3	A new two equation dynamic model for dissipation (Sau & Mahesh (2010)	Dynamic Yoshizawa model (Moin *et al.* 1991)

Table A.1: Different combinations of models for target quantities.

A.2.4 Results

The proposed model is validated using the decaying isotropic turbulence experiments of Comte-Bellot and Corrsin (1971) (referred as CBC hereafter). The Taylor micro-scale Reynolds number $Re_\lambda = u_{\text{rms}}\lambda/\nu$ varies from 71.6 to 60.6 in the experiments. Isotropic turbulence is simulated in a cubical box at 32^3 resolutions. The LES equations (Eq. (A.4)) are solved in Fourier space using a dealiased Fourier–Galerkin pseudo spectral method:

$$\frac{\partial \widehat{u_i}}{\partial t} + ik_l\widehat{u_i u_l} = -ik_i\widehat{p} - \nu k^2\widehat{u_i} + ik_j\widehat{\tau_{ij}}, \text{ and } ik_i\widehat{u_i} = 0 \tag{A.28}$$

where $\widehat{u_i}$ denotes the Fourier transform of $\overline{u}_i$. Projecting the LES equations on the space of solenoidal velocity field, we obtain

$$\frac{\partial \widehat{u_i}}{\partial t} = -\left(\delta_{im} - \frac{k_i k_m}{k^2}\right)(ik_l\widehat{u_l u_m} + ik_l\widehat{\tau_{lm}}) - \nu k^2\widehat{u_i}. \tag{A.29}$$

Third order Runge–Kutta time integration is used for the non–linear terms and Crank Nicholson is used for the viscous term. The simulations are initialized using a random, divergence–free velocity field that matches the initial experimental spectrum at $tU_0/M = 42$, where $M = 5.08$ cm and $U_0 = 10m/s$ are the experimental grid size and mean convection velocity, respectively. The performance of the estimation model is also compared to the dynamic Smagorinsky model.

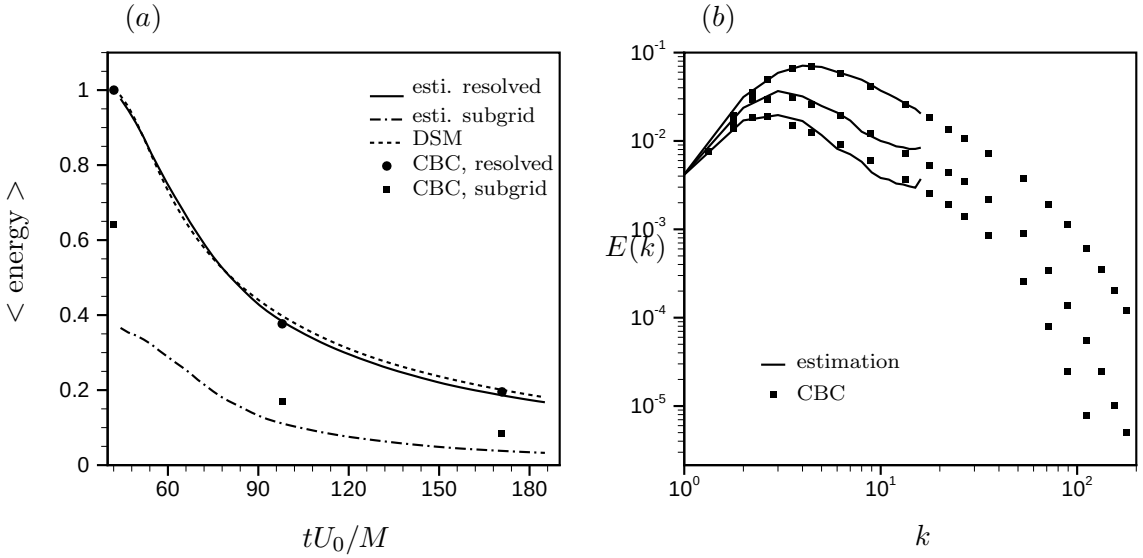

Figure A.1: Decaying isotropic turbulence from LES: (a) resolved and subgrid kinetic energy decay; (b) resolved kinetic energy spectra. Estimation model results are compared with Experiments of Comte–Bellot & Corrsin (1971). Dissipation and subgrid kinetic energy constraints used in the estimation model are (i) Dynamic Smagorinsky and (ii) Yoshizawa model.

A.2.4.1 D^T from DSM and $k^T_{\mathbf{sgs}}$ from Yoshizawa

The results from the proposed estimation model are shown in figure A.1 where D^T and k^T_{sgs} are obtained through dynamic Smagorinsky model and Yoshizawa's model. D^T is obtained as:

$$D^T = \tau^T_{ij}\overline{S}_{ij} \text{ and } \tau^T_{ij} - \frac{1}{3}\tau^T_{kk}\delta_{ij} = -2(C_s\overline{\Delta})^2|\overline{S}|\overline{S}_{ij} \tag{A.30}$$

where $|\overline{S}| = (2\overline{S}_{ij}\overline{S}_{ij})^{\frac{1}{2}}$, $(C_s\overline{\Delta})^2 = \langle L_{ij}M_{ij}\rangle_{h+} / \langle M_{ij}M_{ij}\rangle_h$, $L_{ij} = \widetilde{\overline{u}_i\overline{u}_j} - \widetilde{\overline{u}}_j\widetilde{\overline{u}}_j$, $M_{ij} = (\widetilde{\overline{\Delta}}/\overline{\Delta})^2|\widetilde{\overline{S}}|\widetilde{\overline{S}}_{ij} - \widetilde{|\overline{S}|\overline{S}_{ij}}$. Here, the tilde denotes the test filtering at $2\overline{\Delta}$. $<>_h$ is an average over homogeneous directions, and $\langle\phi\rangle_+ = 0.5(\phi + |\phi|)$ denotes clipping for positive eddy viscosity. Similarly, k^T_{sgs} is obtained from

$$k^T_{\mathrm{sgs}} = 2(C_I\overline{\Delta})^2|\overline{S}|^2 \tag{A.31}$$

where the model coefficient is obtained dynamically, $(C_I\overline{\Delta})^2 = \langle LM\rangle/\langle MM\rangle$, $L = \widetilde{\overline{u}_k\overline{u}_k} - \widetilde{\overline{u}}_k\widetilde{\overline{u}}_k$ and $M = (\widetilde{\overline{\Delta}}/\overline{\Delta})^2|\widetilde{\overline{S}}^2| - \widetilde{|\overline{S}|^2}$.

Figure A.1 shows the time evolution of the resolved kinetic energy and subgrid kinetic energy. The subgrid kinetic energy is computed from the estimated subgrid velocity, $u_i^{'}$. Three dimensional energy spectra is also shown at non–dimensional time $tU_0/M = 42$, 98 and 171. The resolved and subgrid kinetic energy are normalized with the initial resolved kinetic energy. All values except time in the figures are non–dimensionalized by reference velocity $u_{\text{ref}} = \sqrt{\frac{3}{2}}u_{\text{rms}}$ and length scale $L_{\text{ref}} = 11M$. Figure A.1 shows that the proposed estimation model yields good results for resolved kinetic energy and spectra. The estimation model is slightly more dissipative than the dynamic Smagorinsky model. Note that the estimation model underpredicts the subgrid kinetic energy. This behavior is attributed to the Yoshizawa's model which is used constrain the subgrid kinetic energy. Yoshizawa's model is known to underpredict the subgrid kinetic energy (Park & Mahesh 2007).

A.2.4.2 D^T and k^T_{sgs} from Kim & Menon (1995)

Figure A.2 shows the estimation model results when the target values are obtained by solving a transport equation (Schumann 1975, Ghosal *et al.* 1995, Menon *et al.* 1995) for k^T_{sgs}:

$$\frac{\partial k_{\text{sgs}}}{\partial t} + \overline{u}_i\frac{\partial k_{\text{sgs}}}{\partial x_i} = -\tau_{ij}\frac{\partial \overline{u}_i}{\partial x_j} - \epsilon_{\text{sgs}} + \frac{\partial}{\partial x_i}\left(\nu_T\frac{\partial k_{\text{sgs}}}{\partial x_i}\right) \tag{A.32}$$

where the ϵ_{sgs} denotes the subgrid scale dissipation rate and ν_T denotes the eddy viscosity. In this equation subgrid stress τ_{ij} and subgrid dissipation rate ϵ_{sgs} are modeled as

$$\tau_{ij} = -2\nu_T\overline{S}_{ij} + \frac{2}{3}\delta_{ij}k_{\text{sgs}},\ \nu_T = C_\tau\overline{\Delta}k_{\text{sgs}}^{1/2} \text{ and } \epsilon_{sgs} = C_\epsilon\frac{k_{\text{sgs}}^{3/2}}{\overline{\Delta}} \tag{A.33}$$

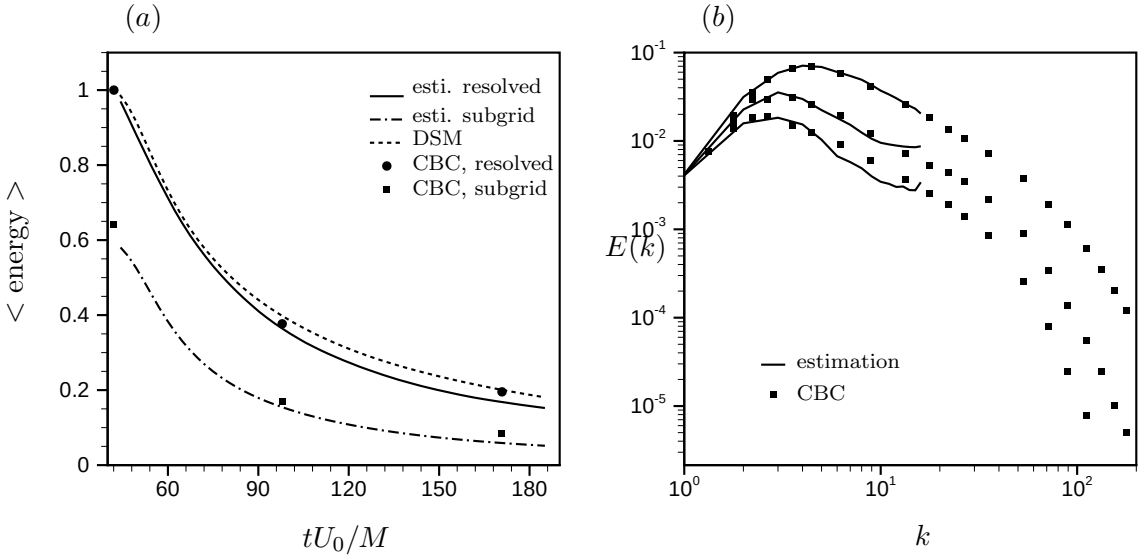

Figure A.2: Decaying isotropic turbulence from LES: (a) resolved and subgrid kinetic energy decay; (b) resolved kinetic energy spectra. Estimation model results are compared with experiments of Comte–Bellot & Corrsin (1971). Dissipation and subgrid kinetic energy constraint used in the estimation model are (i) eddy viscosity model (Kim & Menon 1996) and (ii) a transport equation for k (Kim & Menon 1996).

where C_τ and C_ϵ are determined dynamically (Kim & Menon 1995). Note that all the three terms on the right hand side of (A.32) i.e. production, dissipation and diffusion of $k_{\rm sgs}$, are modeled. Once $k_{\rm sgs}$ is obtained by solving the transport equation, the target dissipation ($D^T = \tau_{ij}\overline{S}_{ij}$) is obtained using Eq. (A.33), where τ_{ij} is a function of $k_{\rm sgs}$.

Figure A.2(a) shows the time evolution of the resolved kinetic energy (solid line) and subgrid kinetic energy (dash–dot line) when the targets are obtained using Eq. (A.32) . The energy spectra is shown in figure A.2(b). Note that the estimation model is slightly more dissipative in this case. However, the estimation model yields better subgrid kinetic energy when a transport equation for $k_{\rm sgs}$ is used.

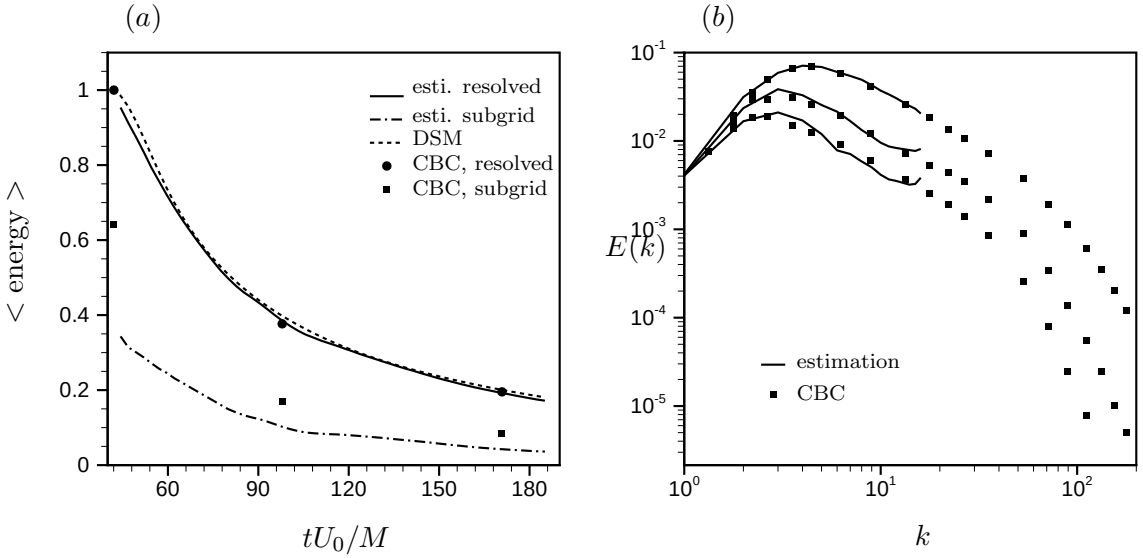

Figure A.3: Decaying isotropic turbulence from LES: (a) resolved and subgrid kinetic energy decay; (b) resolved kinetic energy spectra. Estimation model results are compared with experiments of Comte–Bellot & Corrsin (1971). Dissipation and subgrid kinetic energy constraint used in the estimation model are (i) new two–level dissipation model and (ii) Yoshizawa model.

A.2.4.3 D^T from new dissipation model

The estimation model requires external target subgrid dissipation which we have obtained using eddy–viscosity stress models. Although dissipation is a scalar quantity, it is obtained by modeling the subgrid stress tensor. If a dynamic model for dissipation were developed then eddy–viscosity stress models would not be needed to obtain dissipation. We develop a new dissipation model which applies the dynamic procedure on the dissipation itself. The dissipation is modeled in terms of the invariants of strain–rate tensor. The dynamic procedure uses a second level test filter. The model coefficient is obtained by solving a system of two equations. No least square minimization is required in this model. The model is formulated and validated in the next section in detail. Here, it is briefly summarized below.

The subgrid dissipation, d is modeled as:

$$d = -Cf\left(\overline{\Delta}, \overline{u}_i\right) = -C\overline{\Delta}^2\left(II^n \times III^p\right) \tag{A.34}$$

where C is the non–dimensional model constant, f is a scalar function of second (II) and third (II) invariants of strain–rate tensor $(\overline{S}_{ij})$, and $2n + 3p = 3$. The model constant C is obtained by dynamic procedure as follows. The dynamic equation at the test filter level is

$$D - \{d\} + R = \left\{\overline{u}_i\overline{u}_j\overline{S}_{ij}\right\} - \{\overline{u}_i\}\{\overline{u}_j\}\left\{\overline{S}_{ij}\right\} \tag{A.35}$$

where $\{\}$ denotes the test filter, D is the dissipation at the test filter level and $R = \left\{\overline{u_iu_j}\overline{S}_{ij}\right\} - \{\overline{u_iu_j}\}\left\{\overline{S}_{ij}\right\}$. Note that R is also a subgrid quantity in test filter level and is of the same dimension as d. R is again modeled as:

$$R = C_{r_1} f(\left\{\overline{\Delta}\right\}, \{\overline{u}_i\}) + \left\{\overline{\overline{u}_i\overline{u}_j}\overline{S}_{ij}\right\} - \left\{\overline{\overline{u}_i\overline{u}_j}\right\}\left\{\overline{S}_{ij}\right\} \tag{A.36}$$

where C_{r_1} is a non–dimensional model constant. Note that there are two constants C and C_{r_1} for one dynamic equation in (A.35). A second level test filter, $\langle\rangle$ is used to obtain another dynamic equation in the second test filter level:

$$\mathcal{D} - \langle D\rangle + \mathcal{R} = \left\langle\{\overline{u}_i\}\{\overline{u}_j\}\left\{\overline{S}_{ij}\right\}\right\rangle - \langle\{\overline{u}_i\}\rangle\langle\{\overline{u}_j\}\rangle\left\langle\left\{\overline{S}_{ij}\right\}\right\rangle \tag{A.37}$$

where $\mathcal{R}$ and $\mathcal{D}$ are consistently defined as:

$$\begin{aligned}\mathcal{D} &= \langle\{\overline{u_iu_j}\}\rangle\left\langle\left\{\overline{S}_{ij}\right\}\right\rangle - \langle\{\overline{u_i}\}\rangle\langle\{\overline{u_j}\}\rangle\left\langle\left\{\overline{S}_{ij}\right\}\right\rangle \text{ and}\\ \mathcal{R} &= \left\langle\{\overline{u_iu_j}\}\left\{\overline{S}_{ij}\right\}\right\rangle - \langle\{\overline{u_iu_j}\}\rangle\left\langle\left\{\overline{S}_{ij}\right\}\right\rangle.\end{aligned} \tag{A.38}$$

Using scale–similarity and substituting the models, the two constants, C and C_{r_1}

are obtained from the two scalar identities in (A.35) and (A.37):

$$\begin{bmatrix} \{f_0\} - f_1 & f_1 \\ \\ \langle f_1 \rangle - f_2 & f_2 \end{bmatrix} \begin{pmatrix} C \\ \\ C_{r_1} \end{pmatrix} = \begin{bmatrix} \left\{\overline{u}_i\overline{u}_j\overline{S}_{ij}\right\} - \{\overline{u}_i\}\{\overline{u}_j\}\left\{\overline{S}_{ij}\right\} \\ \\ \left\langle\{\overline{u}_i\}\{\overline{u}_j\}\left\{\overline{S}_{ij}\right\}\right\rangle - \langle\{\overline{u}_i\}\rangle\langle\{\overline{u}_j\}\rangle\left\langle\left\{\overline{S}_{ij}\right\}\right\rangle \end{bmatrix} - \begin{bmatrix} \left\{\overline{\overline{u}_i\overline{u}_j}\overline{S}_{ij}\right\} - \left\{\overline{\overline{u}_i\overline{u}_j}\right\}\left\{\overline{S}_{ij}\right\} \\ \\ \left\langle\left\{\overline{\overline{u}_i\overline{u}_j}\right\}\left\{\overline{S}_{ij}\right\}\right\rangle - \left\langle\left\{\overline{\overline{u}_i\overline{u}_j}\right\}\right\rangle\left\langle\left\{\overline{S}_{ij}\right\}\right\rangle \end{bmatrix} \tag{A.39}$$

where $f_0 = f\left(\overline{\Delta}, \overline{u}_i\right)$, $f_1 = f(\left\{\overline{\Delta}\right\}, \{\overline{u}_i\})$ and $f_2 = f(\left\langle\left\{\overline{\Delta}\right\}\right\rangle, \langle\{\overline{u}_i\}\rangle)$.

This new model is used to obtain the target dissipation in the estimation model simulation. Figure A.3 show the results with the new dissipation model as one of the targets. Here, the Yoshizawa model is used to obtain the target subgrid kinetic energy. Note that the estimation model predicts good results for resolved kinetic energy (fig. A.3a) and the energy spectra (fig. A.3b). The estimation model results are in good agreement with the experimental values for the resolved kinetic energy. Consider the time evolution of resolved kinetic energy obtained using the three different target dissipation - dynamic Smagorinsky model, Kim & Menon (1995) model and new dissipation model in figures in A.1(a), A.2(a) and A.3(a) respectively. The main differences can be noted during the initial transients and the final stage ($tU_0/M = 171$). During the initial transients, the resolved kinetic energy is lower than the DSM simulations in figure A.3(a). Park & Mahesh (2009) note that the filtered EDQNM simulation data shows similar behavior. Also note that the estimation model in figure A.3(a) is closest to the experimental value at the final stage. Thus, the performance of the estimation model is improved when the target dissipation is obtained from the new dissipation model.

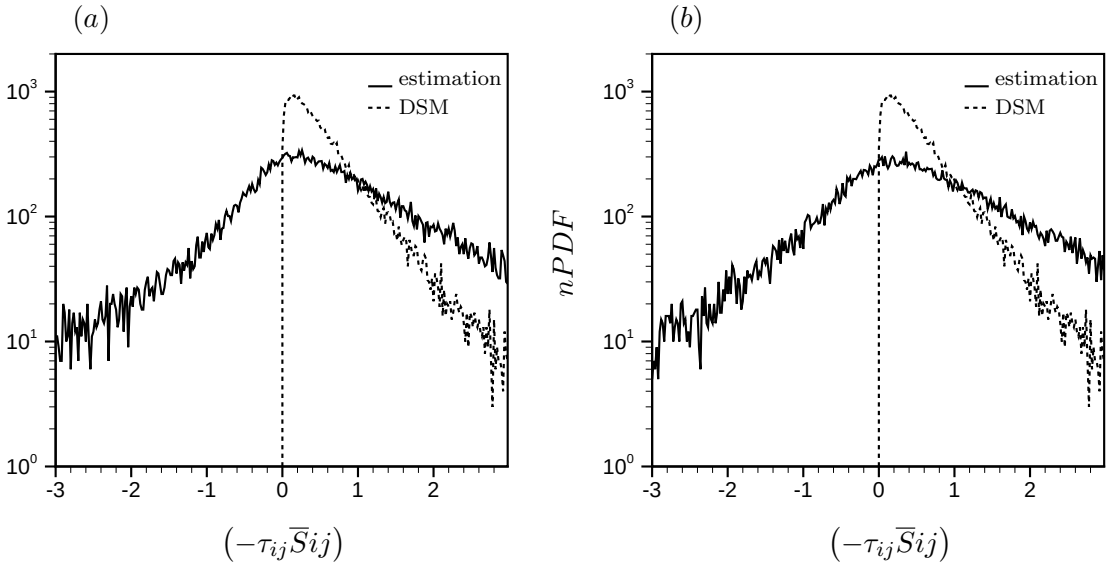

Figure A.4: PDF of subgrid dissipation at $tU_0/M = 64$ using estimation model (using, a and b, two types of target dissipation and kinetic energy constraints) and dynamic Smagorinsky model. Note that the estimation model predicts realistic backscatter.

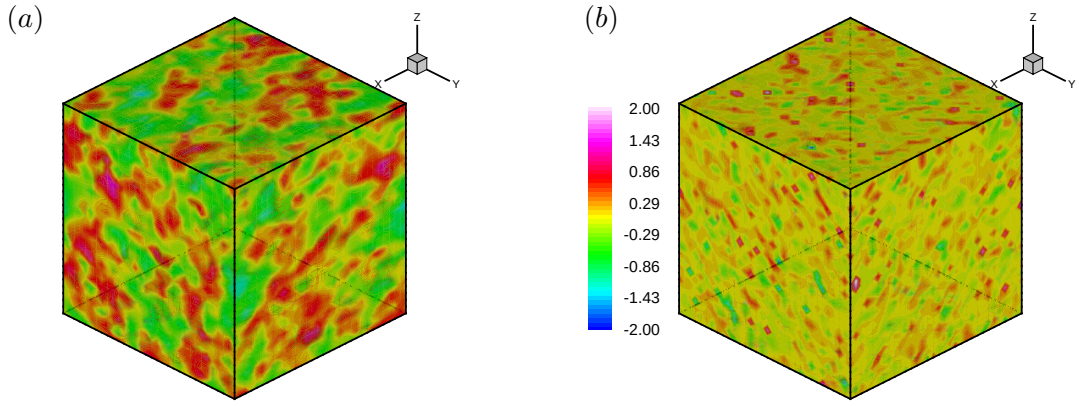

Figure A.5: Instantaneous (a) resolved and (b) subgrid velocity field from the estimation model.

A.2.4.4 Backscatter

Figure A.4 shows the PDF of instantaneous subgrid dissipation from DSM and estimation model. In figure A.4(a), estimation model uses dynamic Smagorinsky and Yoshizawa as the target dissipation and kinetic energy respectively. In figure A.4(b), the targets are obtained using Kim & Menon (1995) model. It is evident from the PDFs that the estimation model predicts large backscatter. Note that the estimation model is stable while producing large backscatter and that this behavior does not depend upon the target values prescribed. The ability to predict the backscatter is an encouraging feature of the proposed estimation model. Figure A.5 shows the instantaneous resolved and estimated subgrid velocity field. The availability of the subgrid velocity in LES simulations, is another advantage of the estimation model over the traditional SGS models. The subgrid velocity will help to better represent or model the subgrid physics in flows that have important physical effects occurring at subgrid scales such as scalar mixing.

A.3 A dynamic model for subgrid dissipation

The subgrid velocity estimation model requires dissipation as an external constraint to the model. The proposed dynamic model can be used to provide the subgrid dissipation. We model the subgrid dissipation instead of subgrid stress. We also show that if the dissipation model is chosen to be consistent with the dissipation provided by the DSM, then the proposed dynamic model for dissipation also yields the model coefficient in the DSM. Since dissipation is a scalar quantity, a dynamic model for dissipation is not over–determined, unlike the Germano identity error in the DSM.

A.3.1 Model formulation

The subgrid scale dissipation,

$$d = \tau_{ij}\overline{S}_{ij} = \left(\overline{u_i u_j} - \overline{u}_i\overline{u}_j\right)\overline{S}_{ij}. \tag{A.40}$$

Note that d is a scalar quantity. We write a one–constant model for d as follows:

$$d = -Cf\left(\overline{\Delta}, \overline{u}_i\right) \tag{A.41}$$

where f is a scalar function of the resolved quantities at the grid filter level and C is the non–dimensional model constant. The function, f is modeled using the second (II) and third (III) invariants of the resolved strain–rate tensor, $\overline{S}_{ij}$:

$$d = -Cf\left(\overline{\Delta}, II, III\right) \tag{A.42}$$

where $II = \left(\overline{S}_{ij}\overline{S}_{ij}\right)$ and $III = det\left(\overline{S}_{ij}\right)$. We model d using a power law:

$$f = \left(\overline{\Delta}^m \times II^n \times III^p\right) \tag{A.43}$$

where, m, n and p can be obtained from dimensional considerations as $m = 2$ and $2n + 3p = 3$. So, the model for dissipation reads,

$$d = -C\overline{\Delta}^2\left(II^n \times III^p\right). \tag{A.44}$$

The model constant C is to be determined dynamically. Note that the dissipation provided by the Smagorinsky model is

$$d_s = \left(-2C_s\overline{\Delta}^2|\overline{S}|\overline{S}_{ij}\right)\overline{S}_{ij} = -\left(2\sqrt{2}C_s\right)\overline{\Delta}^2\left(\overline{S}_{ij}\overline{S}_{ij}\right)^{\frac{3}{2}}. \tag{A.45}$$

If we use $n = 3/2$ in equation (A.44), then we obtain the same expression for dissipation as in equation (A.45):

$$d = -C\overline{\Delta}^2 \left(\overline{S}_{ij}\overline{S}_{ij}\right)^{\frac{3}{2}}. \tag{A.46}$$

This implies, using equations (A.45) and (A.46) that $C = (2\sqrt{2}C_s)$. The Smagorinsky coefficient, C_s for the subgrid stress can therefore be obtained from the dissipation model coefficient, C.

A.3.2 Determination of model constant

The subgrid dissipation at the first test filter level,

$$D = \left(\{\overline{u_i u_j}\} - \{\overline{u}_i\}\{\overline{u}_j\}\right)\{\overline{S}_{ij}\} \tag{A.47}$$

where $\{\}$ denotes the first test filter. Applying the dynamic procedure to dissipation using equations (A.40) and (A.47),

$$\begin{aligned} D - \{d\} &= \left(\{\overline{u_i u_j}\} - \{\overline{u}_i\}\{\overline{u}_j\}\right)\{\overline{S}_{ij}\} - \left\{\left(\overline{u_i u_j} - \overline{u}_i\overline{u}_j\right)\overline{S}_{ij}\right\} \\ &= \left(\{\overline{u_i u_j}\}\{\overline{S}_{ij}\} - \{\overline{u}_i\}\{\overline{u}_j\}\{\overline{S}_{ij}\}\right) - \left(\{\overline{u_i u_j}\overline{S}_{ij}\} - \{\overline{u}_i\overline{u}_j\overline{S}_{ij}\}\right) \\ &= -\left(\{\overline{u_i u_j}\overline{S}_{ij}\} - \{\overline{u_i u_j}\}\{\overline{S}_{ij}\}\right) \\ &\quad + \left(\{\overline{u}_i\overline{u}_j\overline{S}_{ij}\} - \{\overline{u}_i\}\{\overline{u}_j\}\{\overline{S}_{ij}\}\right). \end{aligned} \tag{A.48}$$

Note that the terms inside the first set of parentheses are subgrid terms and the terms inside the second set of parentheses can be computed from the resolved field. Let

$$R = \{\overline{u_i u_j}\overline{S}_{ij}\} - \{\overline{u_i u_j}\}\{\overline{S}_{ij}\}. \tag{A.49}$$

Inserting Eq. (A.49) into (A.48), the dynamic equation at test filter reads,

$$D - \{d\} + R = \left\{\overline{u}_i\overline{u}_j\overline{S}_{ij}\right\} - \{\overline{u}_i\}\{\overline{u}_j\}\left\{\overline{S}_{ij}\right\}. \tag{A.50}$$

Note that since R is not known, we can not obtain the model constant if we assume scale similarity and substitute the models for d and D. Consider a second level test filter, $\langle\rangle$. A similar dynamic equation can be derived at the second test filter level:

$$\mathcal{D} - \langle D\rangle + \mathcal{R} = \left\langle\{\overline{u}_i\}\{\overline{u}_j\}\left\{\overline{S}_{ij}\right\}\right\rangle - \langle\{\overline{u}_i\}\rangle\langle\{\overline{u}_j\}\rangle\left\langle\left\{\overline{S}_{ij}\right\}\right\rangle \tag{A.51}$$

where $\mathcal{R}$ and $\mathcal{D}$ are consistently defined as:

$$\begin{aligned}\mathcal{D} = \langle\{\overline{u_iu_j}\}\rangle\left\langle\left\{\overline{S}_{ij}\right\}\right\rangle - \langle\{\overline{u_i}\}\rangle\langle\{\overline{u_j}\}\rangle\left\langle\left\{\overline{S}_{ij}\right\}\right\rangle \text{ and}\\ \mathcal{R} = \left\langle\{\overline{u_iu_j}\}\left\{\overline{S}_{ij}\right\}\right\rangle - \langle\{\overline{u_iu_j}\}\rangle\left\langle\left\{\overline{S}_{ij}\right\}\right\rangle.\end{aligned} \tag{A.52}$$

Note that (A.50) and (A.51) are two scalar identities. Now, if we use a one constant model for R and use scale similarity, the model constants for d and R can be obtained by solving the system of two linear equations (A.50) and (A.51).

A.3.3 Galilean invariance and R

Note that R is a test filter level quantity (Eq. (A.49)). We write the model for R as

$$R = C_r g\left(\left\{\overline{\Delta}\right\}, \{\overline{u}_i\}\right) \tag{A.53}$$

where C_r is the non–dimensional model constant and g is a scalar function (as yet unspecified) which is modeled using the test filter level quantities. Using scale similarity and substituting the models for d and R into equations (A.50) and (A.51),

$$\begin{aligned}C\left(\left\{f\left(\overline{\Delta},\overline{u}_i\right)\right\} - f(\left\{\overline{\Delta}\right\}, \{\overline{u}_i\})\right) + C_r g(\left\{\overline{\Delta}\right\}, \{\overline{u}_i\}) =\\ \left\{\overline{u}_i\overline{u}_j\overline{S}_{ij}\right\} - \{\overline{u}_i\}\{\overline{u}_j\}\left\{\overline{S}_{ij}\right\}\end{aligned} \tag{A.54}$$

$$C\left(\left\langle f(\left\{\overline{\Delta}\right\},\{\overline{u}_i\})\right\rangle - f(\left\langle\left\{\overline{\Delta}\right\}\right\rangle,\langle\{\overline{u}_i\}\rangle)\right) + C_r g(\left\langle\left\{\overline{\Delta}\right\}\right\rangle,\langle\{\overline{u}_i\}\rangle) = \left\langle\{\overline{u}_i\}\{\overline{u}_j\}\left\{\overline{S}_{ij}\right\}\right\rangle - \langle\{\overline{u}_i\}\rangle\langle\{\overline{u}_j\}\rangle\left\langle\left\{\overline{S}_{ij}\right\}\right\rangle. \tag{A.55}$$

The above equations in matrix form are

$$\begin{bmatrix} \{f_0\} - f_1 & g_1 \\ \\ \langle f_1\rangle - f_2 & g_2 \end{bmatrix} \begin{pmatrix} C \\ \\ C_r \end{pmatrix} = \begin{bmatrix} \left\{\overline{u}_i\overline{u}_j\overline{S}_{ij}\right\} - \{\overline{u}_i\}\{\overline{u}_j\}\left\{\overline{S}_{ij}\right\} \\ \\ \left\langle\{\overline{u}_i\}\{\overline{u}_j\}\left\{\overline{S}_{ij}\right\}\right\rangle - \langle\{\overline{u}_i\}\rangle\langle\{\overline{u}_j\}\rangle\left\langle\left\{\overline{S}_{ij}\right\}\right\rangle \end{bmatrix} \tag{A.56}$$

where $f_0 = f\left(\overline{\Delta},\overline{u}_i\right)$, $f_1 = f(\left\{\overline{\Delta}\right\},\{\overline{u}_i\})$, $f_2 = f(\left\langle\left\{\overline{\Delta}\right\}\right\rangle,\langle\{\overline{u}_i\}\rangle)$, $g_1 = g(\left\{\overline{\Delta}\right\},\{\overline{u}_i\})$ and $g_2 = g(\left\langle\left\{\overline{\Delta}\right\}\right\rangle,\langle\{\overline{u}_i\}\rangle)$. Thus, the model constants can be obtained from the system of equations in (A.56).

Although the model for dissipation is Galilean invariant, the coupled modeled equations are not. The dynamic equation (A.50) at the test filter level is Galilean invariant:

$$D - \{d\} + R = L \tag{A.57}$$

where L is $\left(\left\{\overline{u}_i\overline{u}_j\overline{S}_{ij}\right\} - \{\overline{u}_i\}\{\overline{u}_j\}\left\{\overline{S}_{ij}\right\}\right)$. Since D and $\{d\}$ are Galilean invariant, we require that $R - L$ be Galilean invariant. This is readily seen using the Galilean group of transformations:

$$u_i^* = u_i + V_i \tag{A.58}$$

where $\mathbf{V}$ is a constant vector. The transformations on R yield

$$\begin{aligned} R^* &= \left\{\overline{u_i^* u_j^*}\ \overline{S^*}_{ij}\right\} - \left\{\overline{u_i^* u_j^*}\right\}\left\{\overline{S^*}_{ij}\right\} \\ &= \left\{\overline{(u_i+V_i)(u_j+V_j)}\ \overline{S}_{ij}\right\} - \left\{\overline{(u_i+V_i)(u_j+V_j)}\right\}\left\{\overline{S}_{ij}\right\} \\ &= \left\{\overline{u_i u_j}\overline{S}_{ij}\right\} - \left\{\overline{u_i u_j}\right\}\left\{\overline{S}_{ij}\right\} + 2V_i\left(\left\{\overline{u}_j\overline{S}_{ij}\right\} - \{\overline{u}_j\}\left\{\overline{S}_{ij}\right\}\right); \text{i. e.} \\ R^* &= R + 2V_i\left(\left\{\overline{u}_j\overline{S}_{ij}\right\} - \{\overline{u}_j\}\left\{\overline{S}_{ij}\right\}\right). \end{aligned} \tag{A.59}$$

Similarly,

$$\begin{aligned} L^* &= \left(\left\{\overline{u_i^* u_j^* S^*}_{ij}\right\} - \left\{\overline{u_i^*}\right\}\left\{\overline{u_j^*}\right\}\left\{\overline{S^*}_{ij}\right\}\right) \\ &= \left(\left\{\overline{u}_i\overline{u}_j\overline{S}_{ij}\right\} - \left\{\overline{u}_i\right\}\left\{\overline{u}_j\right\}\left\{\overline{S}_{ij}\right\}\right) + 2V_i\left(\left\{\overline{u}_j\overline{S}_{ij}\right\} - \left\{\overline{u}_j\right\}\left\{\overline{S}_{ij}\right\}\right); \text{i. e.} \\ L^* &= L + 2V_i\left(\left\{\overline{u}_j\overline{S}_{ij}\right\} - \left\{\overline{u}_j\right\}\left\{\overline{S}_{ij}\right\}\right). \end{aligned} \tag{A.60}$$

Now, d is itself Galilean invariant which implies

$$D^* - \{d^*\} + R^* = L^*. \tag{A.61}$$

The above analysis implies that the model for d should be Galilean invariant, but the model for R should be such that

$$R^*_{\text{model}} = R_{\text{model}} + 2V_i\left(\left\{\overline{u}_j\overline{S}_{ij}\right\} - \left\{\overline{u}_j\right\}\left\{\overline{S}_{ij}\right\}\right). \tag{A.62}$$

If R is modeled as $R_{\text{model}} = C_r g(\left\{\overline{\Delta}\right\}, \{\overline{u}_i\})$, where g is a Galilean invariant scalar function, the modeled equations (A.56) for solving C and C_r are not Galilean invariant. This problem can be cured using a mixed model for R:

$$R_{\text{model}} = C_{r_1} g(\left\{\overline{\Delta}\right\}, \{\overline{u}_i\}) + C_{r_2}\left(\left\{\overline{\overline{u}_i\overline{u}_j}\,\overline{S}_{ij}\right\} - \left\{\overline{\overline{u}_i\overline{u}_j}\right\}\left\{\overline{S}_{ij}\right\}\right) \tag{A.63}$$

where C_{r_1} and C_{r_2} are model constants, and the second term on the right hand side is a scale similarity term corresponding to R. Now, using Galilean transformations,

$$\begin{aligned} R^*_{\text{model}} &= C_{r_1} g(\left\{\overline{\Delta}\right\}, \{\overline{u}_i\})^* + C_{r_2}\left(\left\{\overline{\overline{u^*}_i\overline{u^*}_j}\,\overline{S^*}_{ij}\right\} - \left\{\overline{\overline{u^*}_i\overline{u^*}_j}\right\}\left\{\overline{S^*}_{ij}\right\}\right) \\ &= C_{r_1} g(\left\{\overline{\Delta}\right\}, \{\overline{u}_i\}) + C_{r_2}\left(\left\{\overline{\overline{u}_i\overline{u}_j}\,\overline{S}_{ij}\right\} - \left\{\overline{\overline{u}_i\overline{u}_j}\right\}\left\{\overline{S}_{ij}\right\}\right) + \\ &\quad C_{r_2} 2V_i\left(\left\{\overline{\overline{u}}_j\overline{S}_{ij}\right\} - \left\{\overline{\overline{u}}_j\right\}\left\{\overline{S}_{ij}\right\}\right) \\ &= R_{\text{model}} + C_{r_2} 2V_i\left(\left\{\overline{\overline{u}}_j\overline{S}_{ij}\right\} - \left\{\overline{\overline{u}}_j\right\}\left\{\overline{S}_{ij}\right\}\right). \end{aligned} \tag{A.64}$$

Note that if the grid filter is spectral cut-off, then $\overline{\overline{u}}_j = \overline{u}_j$. The constant, C_{r_2} has to be set to one in order to restore the Galilean invariance.

$$C_{r_2} = 1. \tag{A.65}$$

Therefore the model for R,

$$R_{\text{model}} = C_{r_1} g(\{\overline{\Delta}\}, \{\overline{u}_i\}) + \left(\{\overline{\overline{u}_i \overline{u}_j}\overline{S}_{ij}\} - \{\overline{\overline{u}_i \overline{u}_j}\}\{\overline{S}_{ij}\}\right). \tag{A.66}$$

Thus, the system of equations (A.56) for solving the model constants now reads as follows.

$$\begin{bmatrix} \{f_0\} - f_1 & g_1 \\ \\ \langle f_1 \rangle - f_2 & g_2 \end{bmatrix} \begin{pmatrix} C \\ \\ C_{r_1} \end{pmatrix} = \begin{bmatrix} \{\overline{u}_i \overline{u}_j \overline{S}_{ij}\} - \{\overline{u}_i\}\{\overline{u}_j\}\{\overline{S}_{ij}\} \\ \\ \langle\{\overline{u}_i\}\{\overline{u}_j\}\{\overline{S}_{ij}\}\rangle - \langle\{\overline{u}_i\}\rangle\langle\{\overline{u}_j\}\rangle\langle\{\overline{S}_{ij}\}\rangle \end{bmatrix} - \begin{bmatrix} \{\overline{\overline{u}_i \overline{u}_j}\overline{S}_{ij}\} - \{\overline{\overline{u}_i \overline{u}_j}\}\{\overline{S}_{ij}\} \\ \\ \langle\{\overline{\overline{u}_i \overline{u}_j}\}\{\overline{S}_{ij}\}\rangle - \langle\{\overline{\overline{u}_i \overline{u}_j}\}\rangle\langle\{\overline{S}_{ij}\}\rangle \end{bmatrix}. \tag{A.67}$$

A.3.4 Model for g

The model requires the scalar invariant functions f and g. Note that the model for f is already described in equation (A.44). Now, g is also a scalar invariant function and is of same dimension as f, but defined at test filter level. Therefore, g is modeled similar to f but at the test filter level:

$$g(\{\overline{\Delta}\}, \{\overline{u}_i\}) = \overline{\Delta}^2 \left(II_g^n \times III_g^p\right) \tag{A.68}$$

where, $2n + 3p = 3$, and II_g and III_g are the second and third invariants of the velocity gradient tensor in the test filter level:

$$II_g = \left\{\overline{S}_{ij}\right\}\left\{\overline{S}_{ij}\right\} \text{ and } III_g = \det\left(\left\{\overline{S}_{ij}\right\}\right). \tag{A.69}$$

Once g is prescribed, equation (A.67) is solved to obtain the model coefficients.

A.3.5 Determination of Smagorinsky constant in DSM

In the Smagorinsky model, the subgrid scale stress tensor is modeled as,

$$\tau_{ij} = (\overline{u_i u_j} - \overline{u}_i\overline{u}_j) = -2C_s\Delta^2|\overline{S}|\overline{S}_{ij}. \tag{A.70}$$

As shown in equation (A.45), the dissipation provided by Smagorinsky model is

$$d = -\left(2\sqrt{2}C_s\right)\overline{\Delta}^2\left(\overline{S}_{ij}\overline{S}_{ij}\right)^{\frac{3}{2}} = -C_s f\left(\overline{\Delta}, \overline{u}_i\right) \tag{A.71}$$

where $f\left(\overline{\Delta}, \overline{u}_i\right)$ is the invariant scalar function based on strain rate tensor: $f\left(\overline{\Delta}, \overline{u}_i\right) = \overline{\Delta}^2|\overline{S}|^{3/2}$. Similarly, the corresponding function, $g(\left\{\overline{\Delta}\right\}, \{\overline{u}_i\}) = \left\{\overline{\Delta}\right\}^2 |\left\{\overline{S}\right\}|^{3/2}$. So, the model constants can be obtained from the two level dynamic equations:

$$\begin{bmatrix} \left\{\overline{\Delta}^2|\overline{S}|^{3/2}\right\} - \left\{\overline{\Delta}\right\}^2|\left\{\overline{S}\right\}|^{3/2} & \left\{\overline{\Delta}\right\}^2|\left\{\overline{S}\right\}|^{3/2} \\ \left\langle\left\{\overline{\Delta}\right\}^2|\left\{\overline{S}\right\}|^{3/2}\right\rangle - \left\langle\left\{\overline{\Delta}\right\}\right\rangle^2|\left\langle\left\{\overline{S}\right\}\right\rangle|^{3/2} & \left\langle\left\{\overline{\Delta}\right\}\right\rangle^2|\left\langle\left\{\overline{S}\right\}\right\rangle|^{3/2} \end{bmatrix} \begin{pmatrix} C_s \\ C_{r_1} \end{pmatrix} =$$
$$\begin{bmatrix} \left\{\overline{u}_i\overline{u}_j\overline{S}_{ij}\right\} - \left\{\overline{u}_i\right\}\left\{\overline{u}_j\right\}\left\{\overline{S}_{ij}\right\} \\ \left\langle\left\{\overline{u}_i\right\}\left\{\overline{u}_j\right\}\left\{\overline{S}_{ij}\right\}\right\rangle - \left\langle\left\{\overline{u}_i\right\}\right\rangle\left\langle\left\{\overline{u}_j\right\}\right\rangle\left\langle\left\{\overline{S}_{ij}\right\}\right\rangle \end{bmatrix} - \begin{bmatrix} \left\{\overline{\overline{u}_i\overline{u}_j}\overline{S}_{ij}\right\} - \left\{\overline{\overline{u}_i\overline{u}_j}\right\}\left\{\overline{S}_{ij}\right\} \\ \left\langle\left\{\overline{\overline{u}_i\overline{u}_j}\right\}\left\{\overline{S}_{ij}\right\}\right\rangle - \left\langle\left\{\overline{\overline{u}_i\overline{u}_j}\right\}\right\rangle\left\langle\left\{\overline{S}_{ij}\right\}\right\rangle \end{bmatrix} \tag{A.72}$$

The above system of equations is averaged over homogeneous directions to obtain C_s and C_{r_1}. Note that the equations in (A.72) are not overdetermined unlike the

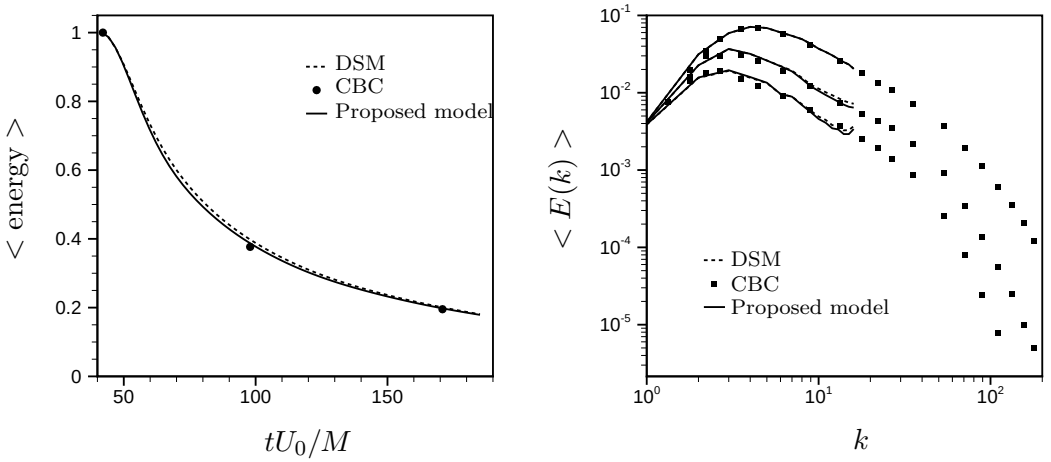

Figure A.6: Decaying isotropic turbulence from LES with Smagorinsky model. The model coefficient is obtained by (i) new two–level dynamic procedure (solid line) and (ii) standard Germano's procedure (dashed line). (a) resolved kinetic energy decay, (b) resolved kinetic energy spectra. Results are compared with experiments (symbols) of Comte–Bellot & Corrsin (1971).

DSM and represent an alternative way to obtain the stress model coefficient in the Smagorinsky model.

A.3.6 Results

The proposed approach is validated using the decaying isotropic turbulence experiments of Comte-Bellot and Corrsin (1971). The Taylor micro-scale Reynolds number $Re_\lambda = u_{\rm rms}\lambda/\nu$ varies from 71.6 to 60.6 in the experiments. Isotropic turbulence is simulated in a cubical box and LES is performed at 32^3 resolutions, The LES equations are solved in Fourier space using a dealiased Fourier–Galerkin pseudo spectral method:

$$\frac{\partial \widehat{u_i}}{\partial t} + ik_l\widehat{u_i u_l} = -ik_i\widehat{p} - \nu k^2\widehat{u_i} + ik_j\widehat{\tau_{ij}}, \text{ and } ik_i\widehat{u_i} = 0 \tag{A.73}$$

where $\widehat{u_i}$ denotes the Fourier transform of $\overline{u}_i$. Projecting the LES equations on the space of solenoidal velocity field, we obtain

$$\frac{\partial \widehat{u_i}}{\partial t} = -\left(\delta_{im} - \frac{k_i k_m}{k^2}\right)(ik_l\widehat{u_l u_m} + ik_l\widehat{\tau_{lm}}) - \nu k^2\widehat{u_i}. \tag{A.74}$$

Third order Runge–Kutta time integration is used for the non–linear terms and Crank Nicholson is used for the viscous term. The simulations are initialized using a random, divergence–free velocity field that matches the initial experimental spectrum at $tU_0/M = 42$, where $M = 5.08$ cm and $U_0 = 10$ m/s are the experimental grid size and mean convection velocity, respectively. In the simulations, the subgrid stress τ_{ij} is modeled using the Smagorinsky model (A.70), where the model coefficient is obtained using the new approach from equation (A.72). The new dynamic procedure is also compared with the standard DSM.

Figure A.6 shows the time evolution of the resolved kinetic energy. Three dimensional energy spectra is also shown at non–dimensional time $tU_0/M = 42$, 98 and 171. The resolved kinetic energy is normalized with the initial resolved kinetic energy. All values except time in the figures are non–dimensionalized by reference velocity $u_{\text{ref}} = \sqrt{\frac{3}{2}} u_{\text{rms}}$ and length scale $L_{\text{ref}} = 11M$. Figure A.6 shows that the proposed dynamic model yields good results for resolved kinetic energy and spectra. Note that there is not much difference in the results for the proposed dynamic model and the DSM. The Smagorinsky coefficients from the two models are plotted in A.7(a). Figure A.7(b) shows the other model coefficient C_{r_1} in the new model. The new models yields slightly higher value of the Smagorinsky coefficient. The transient behavior is similar. Note that the coefficient from the new model is not zero initially. The new model reduces the initial rapid transient behavior of the model coefficient.

A.4 Scalar estimation model

The estimation approach is extended to passive scalar mixing. The key ideas are similar to the velocity estimation model. The subgrid flux is obtained from the modeled subgrid scalar by constraining the subgrid dissipation.

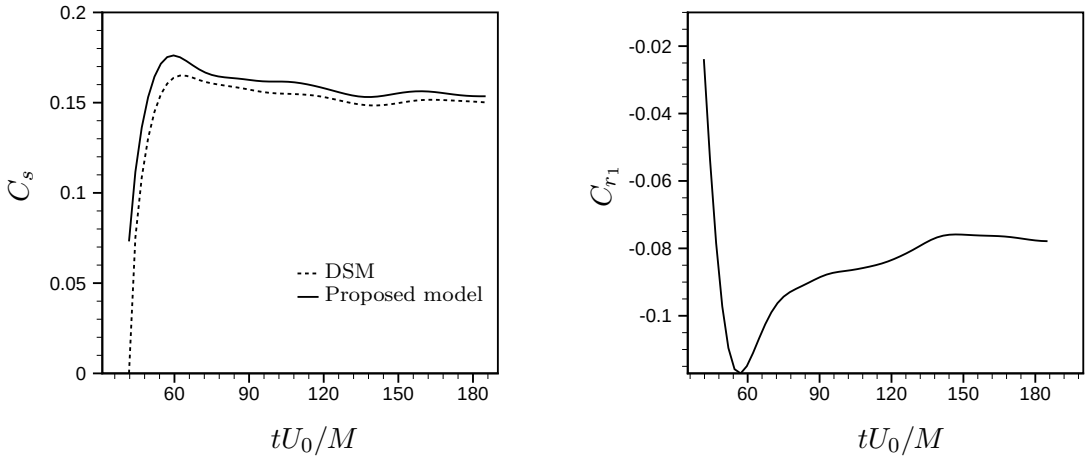

Figure A.7: Model coefficients (a) C_s and (b) C_{r_1}.

A.4.1 Formulation

LES of passive scalar mixing is governed by the filtered scalar–transport equations:

$$\frac{\partial \overline{C}}{\partial t} + \bar{u}_j \frac{\partial \overline{C}}{\partial x_j} = D \frac{\partial^2 \overline{C}}{\partial x_j x_j} - \frac{\partial q_j}{\partial x_j} \ , \quad q_j = \overline{u_j C} - \overline{u}_j \overline{C} \tag{A.75}$$

where q_j is the subgrid scalar flux which requires modeling for closure. In terms of the resolved and subgrid quantities, the subgrid scalar flux,

$$q_j = \overline{\overline{u}_j \overline{C}} + \overline{\overline{u}_j C'} + \overline{u_j' \overline{C}} + \overline{u_j' C'} - \overline{u}_j \overline{C}. \tag{A.76}$$

Note that the scalar flux contains both the subgrid velocity and scalar. The subgrid velocity is available from the velocity estimation model. The subgrid scalar is modeled as

$$C' = RN(\bar{\mathbf{u}}, \mathbf{u}', \overline{C}) \tag{A.77}$$

where R is an adjustable constant and N is a nonlinear scalar function of the known quantities. The performance of the scalar estimation model depends on how subgrid scalar is modeled. N is modeled as the product of resolved scalar gradient and the

subgrid velocity:

$$C^{'} = R\theta u_j^{'} \frac{\partial \overline{C}}{\partial x_j} \tag{A.78}$$

where θ is a time scale. Note that the Galilean invariance of the subgrid flux is preserved.

A.4.2 Coefficient determination

The constant R is determined by imposing the subgrid scale dissipation as a constraint to the estimation model. The dissipation obtained from the estimation model is approximated to match a prescribed 'target dissipation', D_c^T. D_c^T can be supplied through any model, DNS or experiment. Here, it is obtained from dynamic eddy–diffusivity model for scalar flux (Moin *et. al* 1991):

$$D_c^T = q_j^T \frac{\partial \overline{C}}{\partial x_j} \text{ and } q_j^T = \frac{\nu_t}{Sc_t} \frac{\partial \overline{C}}{\partial x_j} = \frac{C_s \overline{\Delta}^2 |\overline{S}|}{Sc_t} \frac{\partial \overline{C}}{\partial x_j} \tag{A.79}$$

where ν_t is the eddy–viscosity, C_s is the dynamic Smagorinsky coefficient for subgrid scale stress tensor and Sc_t is the turbulent Schmidt number. The eddy–diffusivity (ν_t/Sc_t) can be computed from the following relation which is obtained dynamically:

$$\frac{C_s \overline{\Delta}^2}{Sc_t} = -\frac{\langle L_j M_j \rangle}{\langle M_j M_j \rangle} \tag{A.80}$$

where $L_j = \widetilde{\overline{u}_j \overline{C}} - \widetilde{\overline{u}}_j \widetilde{\overline{C}}$ and $M_j = \left(\widetilde{\overline{\Delta}}/\overline{\Delta}\right)^2 |\widetilde{\overline{S}}|(\partial \widetilde{\overline{C}}/\partial x_j) - |\overline{S}|(\widetilde{\partial \overline{C}/\partial x_j})$. The coefficient R is determined by equating the ensemble averaged dissipation from the estimation model and the dynamic eddy diffusivity model. The dissipation constraint is:

$$\left\langle q_j^M \frac{\partial \overline{C}}{\partial x_j} \right\rangle = \langle D_c^T \rangle \tag{A.81}$$

where q_j^M is the flux from estimation model and $\langle\rangle$ denotes the ensemble average. Now substituting (A.76), we obtain

$$\left\langle \left(\overline{\overline{u}_j \overline{C}} - \overline{u}_j \overline{C} + \overline{u_j' \overline{C}} \right) \frac{\partial \overline{C}}{\partial x_j} \right\rangle + \left\langle \left(\overline{(u_j + u_j')C'} \right) \frac{\partial \overline{C}}{\partial x_j} \right\rangle = \left\langle D_c^T \right\rangle . \tag{A.82}$$

Substituting Eq. (A.77) and assuming R is constant with respect to the ensemble, the above equation yields

$$\left\langle \left(\overline{\overline{u}_j \overline{C}} - \overline{u}_j \overline{C} + \overline{u_j' \overline{C}} \right) \frac{\partial \overline{C}}{\partial x_j} \right\rangle + R \left\langle \left(\overline{(u_j + u_j')N} \right) \frac{\partial \overline{C}}{\partial x_j} \right\rangle = \left\langle D_c^T \right\rangle . \tag{A.83}$$

Thus, R is obtained from the simple linear relation:

$$R = \frac{\left\langle D_c^T \right\rangle - \left\langle \left(\overline{\overline{u}_j \overline{C}} - \overline{u}_j \overline{C} + \overline{u_j' \overline{C}} \right) \frac{\partial \overline{C}}{\partial x_j} \right\rangle}{\left\langle \left(\overline{(u_j + u_j')N} \right) \frac{\partial \overline{C}}{\partial x_j} \right\rangle}. \tag{A.84}$$

Note that once the target dissipation is computed, R can be obtained at virtually no additional cost. Once R is obtained, then the estimated subgrid scalar is calculated (Eq. (A.78)) from which the subgrid flux is computed (Eq. (A.76)).

A.4.3 Results

The proposed model is applied to decaying isotropic turbulence with an imposed uniform mean scalar gradient. The velocity field is solved using the velocity estimation approach discussed earlier. The velocity estimation corresponds to the decaying isotropic turbulence experiments of Comte-Bellot and Corrsin (1971). The experimental conditions and simulation details for velocity field are already discussed in Section A.2.4. The scalar field with a uniform mean gradient in y–direction can be expressed as:

$$\widetilde{C} = Sy + C \tag{A.85}$$

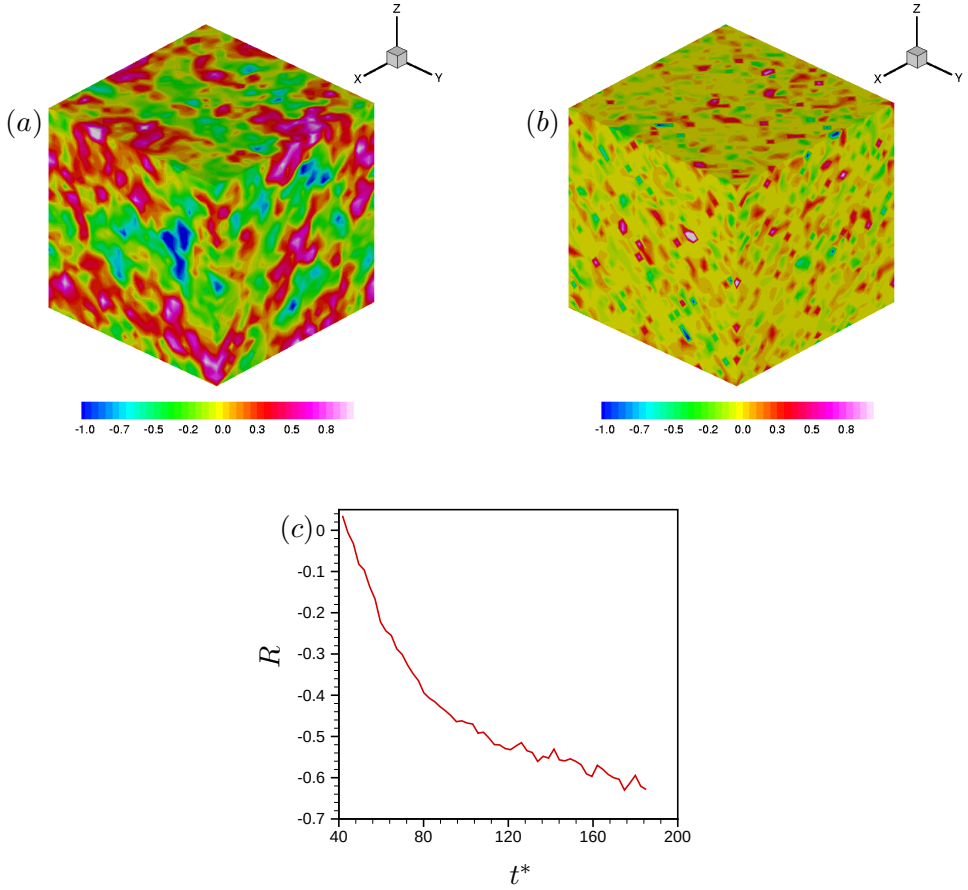

Figure A.8: (a) Estimation model results: (a) resolved scalar and (b) subgrid scale scalar fluctuation at $t^* = 128.6$; (c) time evolution of the model coefficient R.

where S is the imposed uniform gradient in y–direction and C is scalar fluctuations about the mean gradient. The transport equation for governing $\widetilde{C}$ is:

$$\frac{\partial \widetilde{C}}{\partial t} + u_j \frac{\partial \widetilde{C}}{\partial x_j} = D \frac{\partial^2 \widetilde{C}}{\partial x_j x_j} \tag{A.86}$$

where D is the scalar diffusivity. Substituting equation (A.85),

$$\frac{\partial C}{\partial t} + S u_2 + u_j \frac{\partial C}{\partial x_j} = D \frac{\partial^2 C}{\partial x_j x_j} \tag{A.87}$$

where u_2 is the y–component of velocity. Now, applying filter on Eq. (A.87), LES equations for the scalar fluctuations, C can be obtained as:

$$\frac{\partial \overline{C}}{\partial t} + \overline{u}_j \frac{\partial \overline{C}}{\partial x_j} = D \frac{\partial^2 \overline{C}}{\partial x_j x_j} - S\overline{u}_2 - \frac{\partial q_j}{\partial x_j} \quad , \quad q_j = \overline{u_j C} - \overline{u}_j \overline{C} \tag{A.88}$$

The scalar LES equations are also solved in Fourier space using a dealiased pseudo–spectral method:

$$\frac{\partial \widehat{C}}{\partial t} = -ik_j \widehat{u_j C} - Dk^2 \widehat{C} - S\widehat{u_2} - ik_j \widehat{q_j} \tag{A.89}$$

where $\widehat{\ }$ denotes the Fourier transform operator. The scalar field is initialized with a mean gradient ($S = 1.0$) but without any scalar fluctuations $\overline{C} = 0$. Schmidt number, Sc is 1.0. Simulations are performed on 32^3 grid. The performance of the scalar estimation model is compared with the eddy–diffusivity model.

Figure A.8 shows the results from the scalar estimation model. The scalar estimation model is found to be dissipative and stable. Time evolution of the model coefficient R is shown in figure A.8(c). Figure A.8(a) and (b) show contours of the instantaneous resolved and subgrid scalar fluctuations about the mean gradient respectively at $t^* = 128.2$. It is evident from the contours that the resolved and estimated subgrid scalar are large and small scale in nature, respectively. This feature of the estimation model is encouraging.

We compare the estimation model with the dynamic eddy–diffusivity model in figure A.9. The resolved scalar fluctuations at $t^* = 185.6$ are shown from estimation model and eddy–diffusivity model in figure A.9(a) and (b), respectively. Though, the contour structures are different locally but overall, the scalar field looks similar. The ensemble averaged scalar energy and scalar variance are also compared in figure A.9(c)–(d). Figure A.9(c) shows that the production of scalar energy is well predicted by the estimation model. Note that the estimation model does not require additional modeling of the scalar variance. The variance for estimation model is computed from the estimated subgrid scalar. The variance in eddy–diffusivity

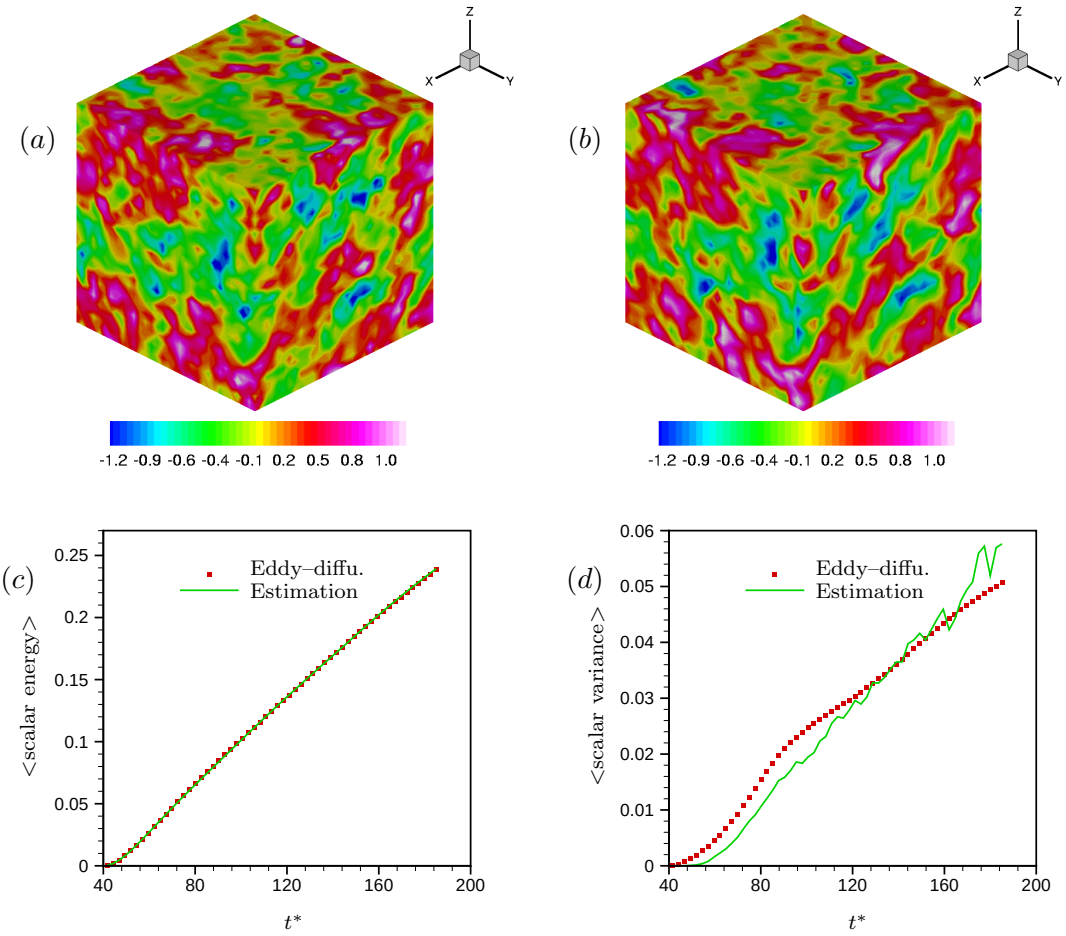

Figure A.9: Comparison to eddy-diffusivity model: contours of resolved scalar field at $t^* = 185.6$ - (a) estimation model, (b) dynamic eddy–diffusivity model. Time evolution of (c) resolved scalar energy and (d) subgrid scalar variance.

model is computed by dynamic Yoshizawa model (Moin *et al.* 1991):

$$\overline{C^2} - \overline{C}^2 = c_v \overline{\Delta}^2 \left| \frac{\partial \overline{C}}{\partial x_j} \right|^2 \tag{A.90}$$

where $c_v = \langle L_v M_v \rangle / \langle M_v M_v \rangle$, $L_v = \widetilde{\overline{C}^2} - \widetilde{\overline{C}}^2$ and $M_v = \left(\widetilde{\overline{\Delta}}/\overline{\Delta}\right)^2 \left(\left| \partial \widetilde{\overline{C}}/\partial x_j \right|^2 - \left| \partial \overline{C}/\partial x_j \right|^2 \right)$. Figure A.9$(d)$ shows that the estimation model yields good prediction of scalar variance when compared to Yoshizawa model.

A.5 Summary

We propose an estimation model for subgrid velocity. The subgrid stress is directly computed from the modeled subgrid velocity. The proposed estimation approach is neither eddy–viscosity nor scale similarity type model. The model coefficients of the subgrid velocity are obtained by imposing constraints on the resulting ensemble averaged subgrid dissipation and local subgrid kinetic energy. The external constraints can be provided from models, DNS or experiments. Here, subgrid dissipation is provided by eddy–viscosity stress models or a new dynamic model for dissipation and subgrid kinetic energy is provided by Yoshizawa model or a modeled transport equation. The proposed estimation model is applied to decaying isotropic turbulence and is shown to yield good results. The proposed model is an improvement over the estimation model by Park & Mahesh (2008). Unlike their model, the Galilean invariance is imposed in a consistent manner and proper r.m.s levels of subgrid kinetic energy are obtained. The proposed model predicts large backscatter of energy while being stable. The model does not require finer grids and defiltering operation on the velocity field compared to other estimation approaches (e. g. Domaradzki *et al.* 2002, Stolz *et al.* 2001)

We propose a new dynamic approach to model subgrid dissipation. The dissipation is modeled using invariants of the strain–rate tensor. The proposed dynamic method uses two–level test filters and the dissipation model co-efficient is obtained using two scalar identities. It is shown that the Smagorinsky coefficient can be obtained using this method, as an alternative to Germano's dynamic approach (DSM). The proposed model is not over–determined unlike the DSM. The proposed model is applied to decaying isotropic turbulence and is shown to yield as good results as standard DSM.

The estimation approach is also extended to passive scalar mixing. The subgrid flux is computed directly from the estimated subgrid velocity and modeled subgrid

scalar. The subgrid scalar is modeled in terms of velocity and resolved scalar gradient. The model coefficient is obtained by constraining the ensemble average subgrid dissipation. The scalar estimation model is applied to decaying isotropic turbulence with an uniform mean scalar gradient and is compared to eddy–diffusivity model. The estimation model yields good results in comparison to the eddy–diffusivity model.